Design of LCoS devices using high contrast gratings

By

Sangeeth Soman Thandasseril

Thesis submitted in fulfilment of the requirements for
the degree of Doctor of Philosophy under the supervision of
A/Prof Alexander Solntsev
(Principal Supervisor)
Prof Christopher Geoffrey Poulton
A/Prof Mikhail Lapine
(Co-Supervisors)

University of Technology Sydney
Faculty of Science

December 9, 2022

CERTIFICATE OF AUTHORSHIP

I, Sangeeth Soman Thandasseril declare that this thesis, is submitted in fulfilment of the requirements for the award of Doctor of Philosophy, in the department of Mathematical and Physical Sciences at the University of Technology Sydney. This thesis is wholly my own work unless otherwise referenced or acknowledged. In addition, I certify that all information sources and literature used are indicated in the thesis. This document has not been submitted for qualifications at any other academic institution. This research is supported by the Australian Government Research Training Program.

Signature:

Production Note:
Signature removed prior to publication.

Date: December 9, 2022

This work is dedicated to my Dad(late), Mother and to my grandmother (late Kausalya)

To my partner, my friends and loved ones.

ACKNOWLEDGEMENTS

I want to thank my PhD supervisors Prof. Alexander Solntsev, Prof. Chris Poulton and Prof. Mikhail Lapine. For giving me valuable suggestions and feedback and supporting me throughout this degree.

I want to thank my industry partner Finisar for supporting me with the materials and parameters helpful in modelling the device.

Though there were insurmountable challenges during the COVID-19 period, my family supported me with unwavering love. Reaching this point of life has had its trials, of which my loved ones might say a few, but I could not have done it without your all support.

The work presented in this thesis would not have been possible without the contributions of many brilliant people, to whom I am very grateful. These people are Simon White from UTS, Steve Frisken (CEO of Cylite), Jeremy Bolger from Finisar and Nitesh Gulati from Finisar.

Thank you, my partner, for providing me with mental support for the last periods of my PhD.

To all my friends at UTS, I would like to thank you for the friendships I made. I will never forget it from the bottom of my heart.

To Geethamma (mother), I miss you every day. I wouldn't be who I am today without your support. I also wanted to thank all the staff and technical officers at UTS who has given unconditional support to my work.

ABSTRACT

Liquid crystal on silicon (LCoS) technology, existing for more than four decades ago, is facilitating a range of applications in photonics. For example, phase-only LCoS devices (LCoSDs) are now routinely used as switching elements in wavelength-selective switches. A range of different approaches have been considered to improve the performance of conventional LCoSDs. For instance, the diffractive optical losses associated with the pixelated backplane need to be alleviated to enhance the optical performance of LCoSDs. To make the device optically flat, I am using the high-contrast grating (HCG) structures implemented by Finisar Australia Pty Limited in C-Band and optimising the performance in other wavelength regions of operation.

In this thesis, I have numerically investigated HCGs to enhance the performance of LCoSDs. The study was performed using Finite-difference time-domain (FDTD) and rigorous coupled-wave analysis (RCWA) methods. For each significant spectral range (1064 nm, visible range, C-band), HCG parameters have been optimised separately. According to this research, silicon would be a suitable material for near-infrared gratings, while silicon nitride would be a promising material for visible gratings. Furthermore, I have investigated a crosslinked silicon HCG structure to improve the reflectivity of conventional LCoS in the C-Band wavelength range and around 1064 nm, introducing polarisation-independent reflectivity. Finally, I studied Finisar's polarisation-independent LCoSD and optimised the performance using various optimisation techniques. In the future, the results of this research will likely contribute to the design of high-performance wavelength selective switches and WaveShapers.

CONTENTS

ILLUSTRATIONS

TABLES

ABBREVIATIONS

LCoSDs: Liquid crystal on silicon devices

CMOS: Complementary metal-oxide-semiconductor

LC: Liquid crystal

SLM: Spatial Light Modulator

WSS: Wavelength Selective Switches

AWG: Arrayed Waveguide Gratings

ROADM: Reconfigurable Optical Add-Drop Networks

HCG: High Contrast Grating

FDTD: Finite Difference Time Domain

RCWA: Rigorous Coupled Wave Analysis

VCSEL: Vertical-Cavity Surface-Emitting Lasers

FEM: Finite Element Method

GD-Calc: Grating Diffraction Calculator

RI: Refractive Index

TE: Transverse Electric

TM: Transverse Magnetic

2D: Two-Dimensional

PML: Perfectly Matched Layer

DBR: Distributed Bragg Reflector

RHCP: Right-Handed Circularly Polarised

1 CHAPTER 1:INTRODUCTION

1.1 INTRODUCTION TO LCOSDS

LCoSDs[1] were developed and recognised for their image and video display applications. This technology is a mixture of light-modulating properties of liquid crystals and the CMOS technology[2-4] by adequately choosing the LC materials and their[5]electro-optic effects. LCoSDs are divided into transmissive and reflective and can alter the polarisation of the incoming light by using the electro-optic properties of liquid crystals. The LCoS spatial light modulator device is used to modulate the phase, amplitude, or polarisation of the light wave in space and time. The device includes a slew of applications, such as adaptive optics for sensing, an optical element for displays, lithography, quantum computing, and telecommunication. A number of critical characteristics are associated with it, including response time, phase precision, phase stability, and linearity of phase modulation, are the reasons behind the selection of LCoS-based spatial light modulator (SLM) panels for such applications.

Currently, there are two different light modulations: phase modulation and amplitude modulation using LCoSDs. In amplitude modulation[6-7], variations in the linear polarisation of incident light travelling through a linear polariser modulate the amplitude of light. A standard LC television uses the same principle of amplitude modulated LCoSDs. In phase modulation, the phase delay is achieved by electrically varying the refractive index along the incident light path, which is possible mainly due to the non-zero birefringence of the LC elements in use. However, this process needs to be cautiously characterised[8-13]. In phase-only LCoSDs, zero absorption by polarisers or other light-absorbing components will occur, providing maximum light efficiency.

When a phase-only LCoSDs is implemented as an SLM, with a polarised LASER source[14-15], by spatially modulating the wavefront, the SLM can be applied in augmented displays with holographic imaging.

Frisken et al.[16-17] developed a phase-only LCoS as a switching element in wavelength selective switches (WSS) in the telecom wavelength regime. Being a transparent and agile network, LCoS-based SLMs have a significant role in novel transmission media, such as multi-core-mode switching and wavelength re-configuration. Previously, WSS functionality was performed via Arrayed Waveguide Gratings (AWG)[18] implemented for wavelength selectivity along with thermo-optic Mach Zehnder switches for switching featured into an integrated photonic circuit are feasible for a reasonable channel count and fewer port count devices. The narrowing of the optical spectra of the AWG leads to intractable group delay and polarisation instabilities across the band. LCoSDs are more advantageous because they can support more channels and diverse functionalities. The optical spectral width of each channel can be tailored, and spectral shaping within the channel has been implemented to generate an optimal transmission path[19].

By using the electro-optic effect within the thin cell of nematic liquid crystal, the LCoSDs convert the voltage on the silicon CMOS pixelated backplane to a calculated phase. This is similar to the image creation in LCoS projectors, and switching can be achieved in milliseconds. MEMS (microelectromechanical systems) based WSS is also a widely implemented switching elements in ROADMs (reconfigurable optical add-drop networks). Compared to the mechanical complexities involved in MEMS[20] by tilting the mirrors for switching to fibre optic ports, the drop and continue function[21] is performed in reflective LCoS by coupling power to multiple ports necessary for ROADM.

Figure 1.1 shows LCoS-based WSS design[21] from Finisar employed to control the phase of light at each pixel and steer the beam into different output ports. This design generates phase steps to create low insertion loss and high-efficiency switching. The light from the input fibre array passes through the polarisation diversity optics, which makes a high-efficiency orthogonal s-polarisation state for the diffraction grating. The selected fibre input light is reflected from the imaging mirror and then angularly dispersed by the grating and focused on the LCoS. Then the light gets reflected at a vertical angle by applying different voltage patterns to the liquid crystal cells. The optical path of each wavelength is retraced after the reflection from the LCoS, and each wavelength is steered to a particular output port of the fibre array, depending on the reflection angle. As all the individual wavelengths are spaced, switching each wavelength is interference-free with the wavelengths on different channels.

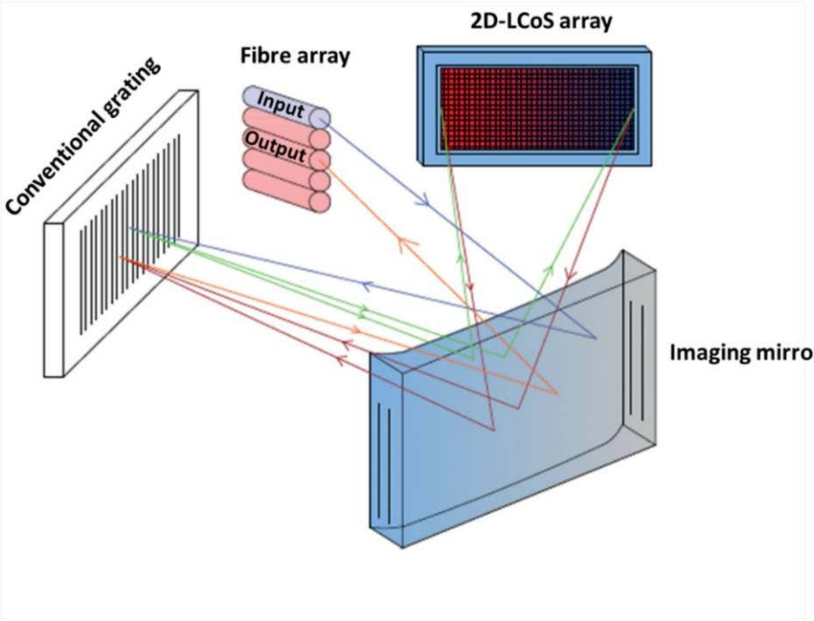

Figure 1.1. LCoS-based Wavelength selective switch (WSS) design from Finisar[16]. Input fibre(purple) carries many wavelengths, which are then separated by the conventional-s-polarised grating and directed to a specific output fibre (pink) based on the phase added by the SLM. In summary, SLM works as a dynamic lens due to the change in phase applied.

1.1.1 LC electro-optic effects for phase only LCoSDs

The most critical property of LCs for phase manipulation is the optical birefringence $\Delta n_{RI} = n_{eRI} + n_{oRI}$, where n_{eRI} is the extraordinary refractive index of light with the polarisation of the electric field parallel to the director and n_{oRI} is the ordinary refractive index for that parallel to the director of the LC molecule, as shown in Figure 1.2(a). Generally, all LC molecules have a positive birefringence[22-24] ranging from 0.05 to 0.45.

The incident light can be modulated in various ways by the electro-optic properties of the LC element with the voltage applied across the LC element and the electrodes. A slew of LC electro-optic structures have been characterised and tested in LCoSDs, including surface stabilised ferroelectric LC (SSFLC)[25-28], twisted nematic[29], vertically aligned nematic (VAN)[30], optically compensated birefringence[31] (OCB) and an untwisted nematic LC with electrically controlled birefringence[32-34](ECB). Untwisted nematic ECB mode is more captivating than other structures in the phase-only applications of LCoSDs.

An untwisted nematic LC (Freedericksz cells) with a positive dielectric anisotropy is implemented such that when an electric field is applied to the LC molecules, the orientation of the director switches from planar to homeotropic. For instance, the polyimide alignment layer holds the LC molecules in a particular non-vertical direction, as shown in Figure 1.2 (b). In the OFF state, where no voltage is applied, the first layer of LC molecules sits at an angle of 3° to the horizontal. This slight tilt angle is necessary to block the reverse tilt switching[35]; nonetheless, the pre-tilt angle should be much smaller to enhance the depth of phase modulation. The remaining layers conform to this alignment unless an external electric field is applied. When an electric field is applied across the LC cell, the molecules are partially aligned with the applied electric field. The more significant the field, the closer the alignment. While a cell designed for visible light operation will require a 2V range, a typical cell designed for C-band will require nearly twice the voltage and twice the cell thickness. When the applied electric field crosses the 10^6 V/m, the molecules are almost fully aligned with the applied electric field, and there is no further change in the birefringence.

The downside of the ECB mode is the excessive backflow of the LC molecules during the switching[36]. This backflow can decelerate the switching, especially in the thicker cells designed for C-band infra-red[37-38] communications. When the voltage applied is switched off, the neighbouring molecules next to the surface force the mid-layer molecules in the opposite direction, creating asymmetric torque and delayed response time. Thus, for practical phase modulation, it is highly desirable to use an ECB electro-optic effect with an untwisted configuration and a slight pre-tilt angle.

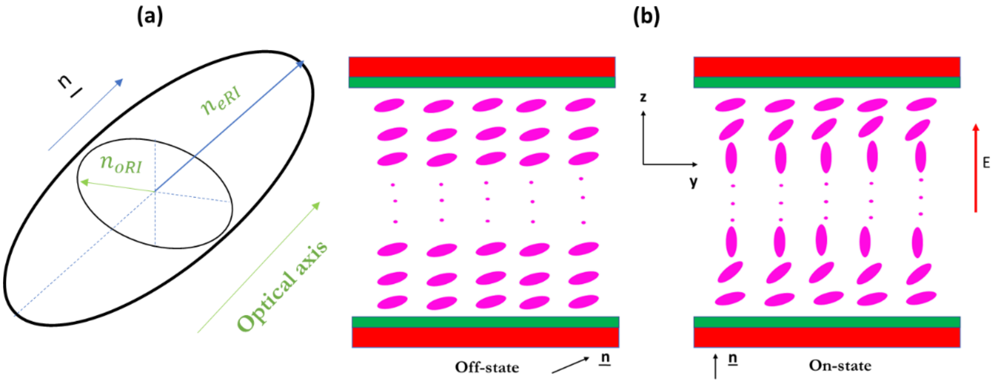

Figure 1.2(a,b): (a)A schematic of LC molecular birefringence. n_{eRI} is the extraordinary refractive index of the molecule, n_{oRI} is the ordinary refractive index, and $\underline{n}$ is the unit vector indicating the direction of the molecular ordering of liquid crystal molecules. Image from[5] (b) Schematic of zero-twisted configuration in electrically controlled birefringence(ECB) with the slight tilt angle. Image adapted with permission from[5].

1.1.2 Conventional reflective LCoSDs

Conventional reflective LCoS, as shown in Figure 1.3, includes liquid crystal material sandwiched between a transparent glass layer having a transparent indium tin oxide electrode and a CMOS silicon backplane. Two-dimensional bi-periodic pixelated reflective aluminium mirrors, individually driven by the voltage applied to provide a phase change to a minimum of one polarisation component of the incoming optical signal, are mounted on a silicon CMOS backplane. Once the voltage is applied to the pixels, the LC molecules orientate in a particular direction creating a phase delay to the incoming incident light. Different phase delay patterns correspond to different reflective angles. So, by controlling applied voltage patterns on multiple LC cells, the reflective angle can be controlled. The reflected light is steered to a particular output port by the phase modulation in the phase-only LCoS SLMs. Currently, the smallest pixel size commercially available for reflective LCoS SLM[39] is more than 3 microns.

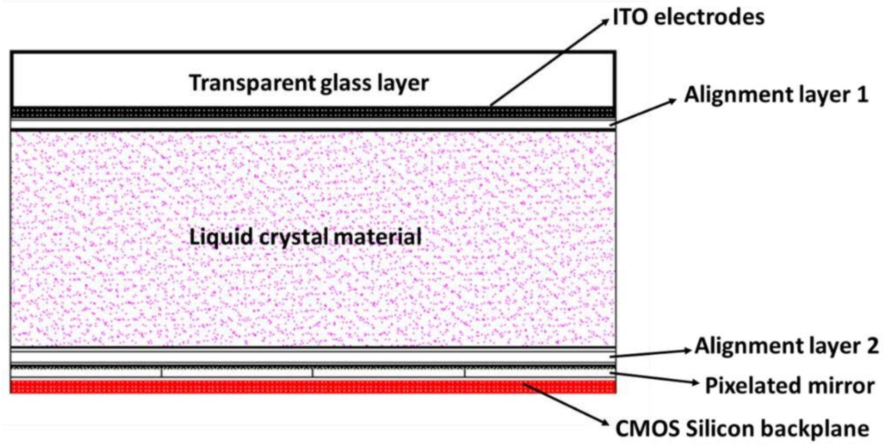

Figure 1.3. Illustrated schematically conventional reflective LCoS without grating[40].

Since the wavelength of the incident light is greater than the periodicity of the pixels, the pixels work in a diffraction regime. Typically, conventional reflective LCoSDs have a fill factor of less than 100%. The fill factor is the percentage of reflective area within each metallic aluminium pixel. Hence, the diffraction orders also appear, and the overall power distributed in several orders creates diffraction optical losses.

1.2 MOTIVATION OF THE THESIS

The motivation for this research is based on optimising the diffractive optical losses associated with the pixelated silicon backplane, thereby enhancing the performance of reflective LCoSDs. Using a subwavelength grating structure in near-infrared to visible wavelengths, I have designed a high-reflectivity LCoSD that mitigates the diffractive optical losses. Previous uses of multilayer dielectric coatings, such as Bragg mirrors, have been used to reduce optical losses resulting in inherent voltage drops. These were performed to suppress the pixel geometry and, in turn, create fringing field effects. Due to the addition of a thicker Bragg mirror design, LCoSDs are limited in their performance by the fringing field effect. Adding HCGs on top of the pixelated structure can significantly improve the performance of LCoSDs. Furthermore, reflection off the subwavelength grating design alleviates the optical losses associated with the diffraction and absorption created by the pixelated metallic structure.

A high difference in the refractive index of the grating layer can provide a slew of properties like broad high reflection efficiency[41-43]and high-Q resonances[44-47]. Of these, the broad reflectivity of HCGs is suitable for enhancing the performance of LCoSDs. As compared to the diffraction gratings, only 0-th order diffraction propagates after being reflected or transmitted by HCG since the grating is subwavelength in nature. With the material and parameters provided by Finisar, I have designed an LCoS backplane that incorporates subwavelength silicon HCG structures[48]. This boosts the efficiency of the 0-th order reflection of s-polarised input light in comparison to conventional LCoS backplanes. On top of pixels in visible operation wavelengths, I have used silicon nitride subwavelength gratings and studied the enhancement of reflection efficiency associated with s-polarised input light compared to the conventional LCoS. In chapter 6, I designed the 2D-cross-linked silicon subwavelength HCGs exhibiting the polarisation independent reflectivity. This thesis concludes with the optimisation of metallic-dielectric uniperiodic subwavelength gratings for near polarisation-independent reflectivity and π-phase shift between orthogonal reflection efficiency components using the initial grating parameters from the patent[49].

Maxwell's equations must be solved in vectorial form since I am modelling LCoS structure incorporating high index contrast sub-wavelength gratings and optimising for smaller pixel sizes. The simulation platforms are the finite difference time domain method (FDTD)[50] using Lumerical and rigorous coupled-wave analysis[51] using GD-Calc, which numerically solves Maxwell's equation for vectorial fields.

1.3 THESIS STRUCTURE

This research aims to simulate, at a basic level, the most useful models for my industry partner. It focuses on high reflectivity LCoS backplanes for performance improvements in other wavelengths of operations ranging from visible to near infra-red. As proposed in this thesis, these models are essential for high-performance wavelength selective switches and WaveShapers[52].

This thesis is structured as follows:

Chapter 1: Introduction: Here, the effective plans and motivations for the research are introduced and reviewed.

Chapter 2: Numerical simulations to calculate the reflection efficiency of LCoSDs. The fundamentals of HCG structure are briefly discussed. The reflection efficiency of LCoS structure without pixels and with grating is simulated in different simulation platforms, such as the finite difference time domain method and rigorous coupled-wave analysis.

Chapter 3: Design of LCoS without pixels and with silicon HCG. The reflection efficiency of LCoS without pixels and with grating is designed and optimised at 1550 nm, and 1064 nm near infra-red wavelength ranges, and the fabrication tolerances are analysed.

Chapter 4: Design of high reflectivity LCoS with pixels and grating in near-infrared wavelengths. A subwavelength silicon HCG on top of pixels is added. This is shown to enhance the reflection efficiency being simulated from near-infrared wavelengths. The formation of standing waves that contribute to optical losses in the pixel gap region and the layers above pixels are also studied.

Chapter 5: Design of silicon nitride HCG LCoS in the visible wavelength range. Here I discuss the design of the LCoS structure with silicon nitride subwavelength

HCG. The 0-th order reflection efficiency is shown to be enhanced after introducing silicon nitride subwavelength HCG on top of pixels in the visible wavelength range.

Chapter 6: Polarisation-independent gratings for high-reflectivity LCoS in near-infrared. Cross-linked silicon bi-periodic grating on top of pixelated backplanes is introduced here. This is shown to enhance both s and p components of 0-th order reflection efficiency and reaches unity reflection at 1064 nm.

Chapter 7: This research has investigated the uni-periodic metal-dielectric grating, which rotates the 0-th order s and p polarisation components to 180 ° by introducing anisotropic refractive index profile in orthogonal lateral dimensions with near polarisation independent reflectivity.

Chapter 8: Presents the summary and outlook of the current research and discusses some anticipated directions that can add to the work provided in this thesis.

2 CHAPTER 2:INTRODUCTION TO DIFFRACTION GRATINGS AND NUMERICAL METHODS

Chapter 2 describes the fundamentals of diffraction gratings and numerical simulation methods involved in simulating the LCoS designs in this project. The important simulation platforms include RCWA and the Finite difference time domain (FDTD) method.

2.1 INTRODUCTION TO DIFFRACTION GRATINGS

The word diffraction, from the Latin word "diffringere", which means "to break into pieces", was first named by Francesco Maria Grimaldi in 1665. Since then, diffraction gratings have been a hot research topic for optical physicists and engineers. They are integral to optical devices such as lasers, wavelength-selective switches, and spectrometers. Their general use in optical devices has been prominent due to their properties gained by the diffraction of optical signals caused by the structural properties. For instance, gratings are used to provide broad high reflectivity mirrors with low optical losses to improve the performance of LCoS in C-Band[40]. A few examples of these gratings include HCGs and Bragg gratings.

Gratings with subwavelength periodicity called HCG have drawn significant attention due to their ability to provide high reflectivity over a broad wavelength range with robust and compact structures. Conventional Bragg gratings are replaced with HCGs in vertical-cavity surface-emitting lasers (VCSELs)[53-54] and LCoS backplanes, developing engineering a slew of exciting properties crucial for different applications. These applications include more uncomplicated epitaxial structure[55], broad wavelength tunability[53] and wavefront control[56]. Conventional metallic mirrors give rise to ohmic and absorptive losses compared to HCGs. HCG mirrors are free from thermal-induced stress as well as initial deformation from stress. Conventional MEMS mirrors are coated with metal for switching wavelength selectivity applications since metal provides high reflectivity. During the heating from a light source, MEMS mirrors become distorted due to thermal stress. The thermal stress build-up due to temperature change and different coefficients of thermal expansion of the materials used. Once MEMS are heated above the threshold level, they distort the wavefront. Knoernschild and Kim demonstrated experimentally the warping of MEMS mirrors, which are heated with high optical power[57]. Thus, HCGs can remain consistently flat compared to conventional MEMS mirrors at high temperatures caused by high-power LASERs. For beam steering applications, HCG mirrors are much faster than any MEMS mirror due to low mass and inertia and have a wider reflectivity than DBR mirrors.

Diffraction grating generally is a periodic structure consisting of dielectric materials with distinct refractive indices. We can classify the grating into two-or three-dimensional structures depending upon the spatial direction of the periodicity since the dielectric materials are arranged in a particular fashion, and the grating modulates the phase and the amplitude of the incident optical signal. The pitch or periodicity of the grating and the refractive index difference define the properties of the diffracted wavefront. The reflectivity at an operational wavelength can be altered by varying the grating parameters. A uni-periodic grating with periodicity d_x along the x-direction is shown in Figure 2.1. A plane wave with an angle of incidence θ_{inc} , with respect to the grating normal $\hat{\imath}$ is made to incident on a uni-periodic one-dimensional grating.

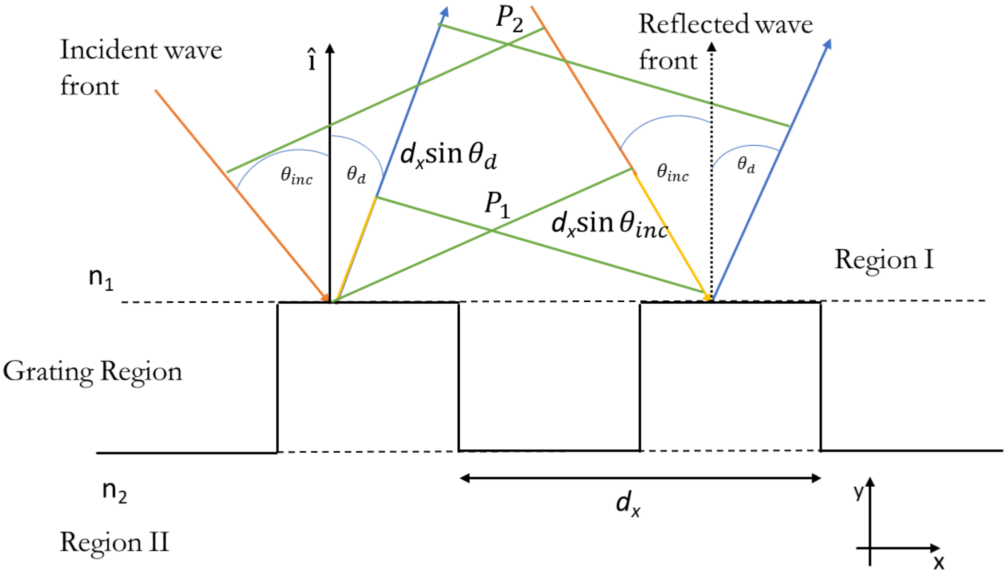

Figure 2.1. Example of a uni-periodic one-dimensional grating. The grating region has a periodic refractive index with the periodicity of d_x and varies from n_1 to n_2. The reflected wavefront interferes constructively or destructively depending upon the propagated distance.

According to the Huygens-Fresnel principle, the reflected light from every rectangular grating groove will be a source in the reflected wavefront. These source points will have different phases due to the difference in path length ($d_x \, sin\, \theta_{d,m} - d_x \, sin\, \theta_{inc}$), and an interference pattern will be evident in the scattered light. Depending on the source points' (P_1 and P_2, as shown in Figure 2.1) phase difference, the interference will be constructive or destructive. For the constructive interference to occur, the path difference between the points of the same plane wavefront has to be an integer multiple of the wavelength of the incident light, λ. The condition can be mathematically expressed as,

$$\sin\theta_{d,m} = \sin\theta_{inc} + m\frac{\lambda}{d_x} \qquad \text{m=0}, \pm 1, \pm 2, \dots.. \qquad (2.1a)$$

Where $\theta_{d,m}$ is the angle between the m-th diffracted mode direction and the grating-normal vector $\hat{\imath}$ and θ_{inc} is the angle of incidence, as shown in Figure 2.1. Considering the wavenumber $k = \frac{2\pi}{\lambda}$; a general expression is obtained by defining the grating wavenumber $K = \frac{2\pi}{d_x}$;

$$k_{x,m} = k_{x,i} + mK \qquad \text{m=0}, \pm 1, \pm 2, ,, \qquad (2.2a)$$

Where the x-component of the wavevector $k_x = k \sin \theta_{d,m}$.

From Equation (2.1a), assuming normal incidence, the necessary and sufficient condition for the diffracted mode to exist is given by,

$$\left|\sin \theta_{d,m}\right| < 1 \quad \Leftrightarrow \quad \left|m \frac{\lambda}{d_x}\right| = \left|m \frac{K}{k}\right| < 1 \qquad (2.3a)$$

Equation 2.3a defines the maximum diffraction order retained in the scattered light and depends on the ratio between the incidence wavelength and the grating periodicity.

Multilayer dielectric grating[58-59] is the most commonly employed in photonic devices, including the LCoS backplane. Bragg grating is a one-dimensional grating with multi-layer dielectric coating with a periodic alternation, as shown in Figure 2.2(a). According to Bragg's law, the spectral properties of the multilayer dielectric coating are described by,

$$m \frac{\lambda_B}{\bar{n}} = 2 d_x \sin \theta_{inc} \qquad (2.4a)$$

Where m is an integer and $\bar{n}$ is the mean refractive index in one grating period $\mathrm{d_x}$ and λ_B is the Bragg wavelength.

$$\bar{n} = \frac{n_1 L_1 + n_2 L_2}{d_x} \qquad (2.5a)$$

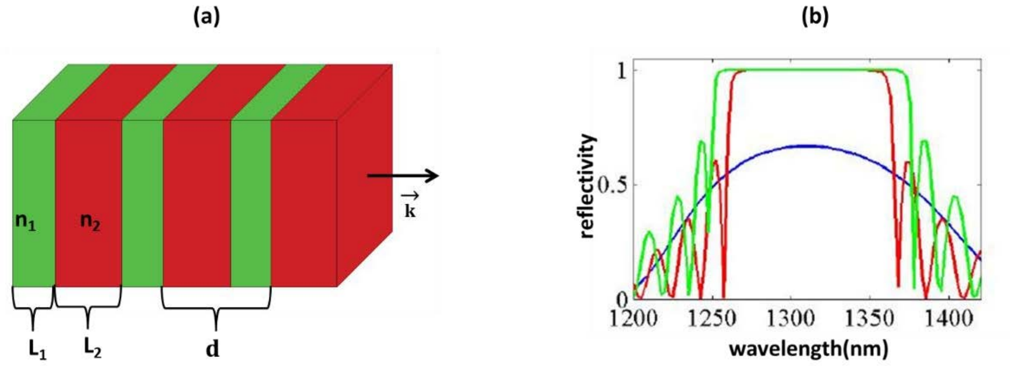

Figure 2.2 (a, b). Example of one-dimensional multilayer dielectric Bragg grating. (a) Illustrates the grating region with a periodic variation of refractive indices between $\boldsymbol{n_1}$ and $\boldsymbol{n_2}$ with a periodicity of d. (b) Showing the reflectivity spectra[60] of different Bragg gratings with a central Bragg wavelength of 1310 nm. The red and blue curves represent two gratings with a refractive index difference, $\boldsymbol{\Delta n = 0.36}$ and 50 and 30 periodicity, respectively. The green curve shows the reflectivity spectra corresponding to the grating with $\boldsymbol{\Delta n = 0.45}$ and the number of periods equal to 50.

Where n_1, L_1 and n_2, L_2 are the refractive indices and the lengths of the two dielectric materials of the Bragg grating. Let us consider a spectrum of Bragg reflectors reported in Figure 2.2(b). The centre wavelength is the Bragg wavelength λ_B . There is a dependency on the number of grating periods and the refractive index difference Δn. By making Δn constant and the bandwidth of reflectivity and the reflectivity at λ_B increase by increasing the number of periods, clearly shown in blue and red reflectivity spectra in Figure 2.2(b). While increasing the number of periods, the more significant contribution of partial internal reflections occurs within the grating structure leading to multiple interferences to form the diffracted wave. If the number of grating periods is constant and Δn incremented, the high reflectivity spectra broaden, as shown by the red and green spectra. If Δn is small, the reflectivity given by the internal layers will be small, leading to a lower diffraction intensity. Similarly, if Δn is large, then the diffraction efficiency is more significant, and fewer grating periods will be enough leading to a smaller structure.

Therefore, in applications such as LCoS backplane, Yang et al.[59] showed that the multilayer dielectric Bragg grating has a total thickness of 3.16 microns for operating in the C-band. Thus from one side, the contrast in indices of refraction cannot be much higher because that will lead to lattice mismatch constraints[61]. Conversely, lesser refractive index differences decrease the diffraction efficiency, and many Bragg grating periods are required to achieve high reflectivity over broadband. In[59], seven stack repetition design provides more than 98% of the s-component of reflectivity in C-Band. There is a possibility of improving the reflectivity by more than 99.99% by increasing the number of stack repetitions. Still, it will create a thickness of more than 3.16 microns, creating a thicker dielectric mirror design. However, thicker multilayer Bragg designs will create fringing field effects in the LCoS device.

2.2 HIGH INDEX CONTRAST GRATINGS FOR BROAD REFLECTIVITY

Subwavelength HCGs have proven to be a suitable alternative to dielectric Bragg gratings to enhance photonic devices' robustness and compactness. These novel gratings can impart high refractive index difference Δn, with much smaller dimensions. The typical thickness of HCGs ranges from 500 nm to 1000 nm and is nearly a thousand times smaller than Bragg reflectors. They are suitable candidates for broad high reflectivity bandwidth and polarisation selectivity applications.

The subwavelength HCG structure proposed in[43] has a significant refractive index difference due to silicon and silica. Figure 2.3(a) illustrates the design as an ultra-broadband high-reflectivity mirror. Metal mirrors also have large reflection bandwidths, but the absorption losses contribute to lower reflected power. The critical design parameters that contribute to the mirror effect are the index of refraction of the materials, the thickness of the low index layer, the grating thickness, the width of the high index layer and the periodicity of the grating. The grating periodicity determines the centre wavelength of the broad reflection band. The design parameters[43] used in the model were: periodicity (d_x) = 700 nm, the refractive index of silicon=3.48, lower silica layer index=1.47, grating thickness(t_g)=0.46 and duty cycle=0.75(fraction of high index material to low index material). Figure 2.3(b) illustrates the effect of waveguide array modes inside the grating, assuming the angle of incidence as zero.

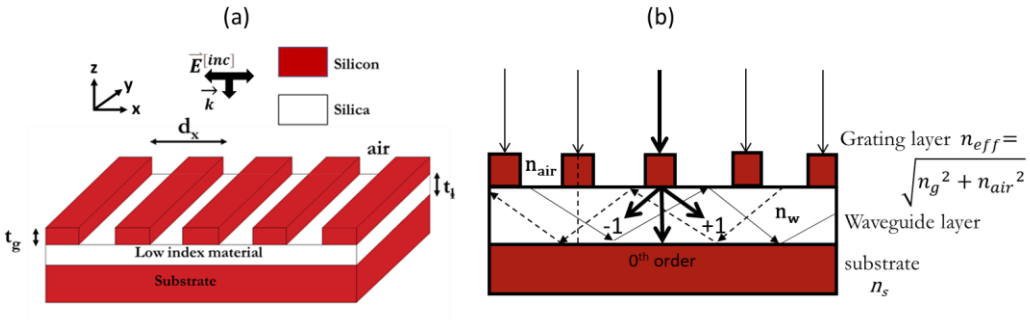

Figure 2.3(a, b). (a)Schematic of the subwavelength high contrast grating reflector. Reproduced from[43].(Copyright © 2004, IEEE). The low index layer thickness is essential for the ultra-broadband mirror effect. (b)Front view of the subwavelength HCG with waveguide array modes. For normal incidence, the grating effective refractive index, $n_{eff} = \sqrt{\mathbf{3.48^2+1^2}}$=3.6208 which is >$n_w$(refractive index of low index layer)>n_{air}, there exists two waveguide array modes[62]. Interaction of these modes with the 0th order mode at the input and output planes of the grating decides whether the HCG is highly reflective or transmissive.

The ultra-broadband mirror effect can be explained[63] as a combined effect of propagation of two-waveguide array modes within the grating layer and their reflection of the boundaries separating the grating thickness($\mathbf{t_g}$) and low index layer thickness ($\mathbf{t_l}$). Suppose a plane wave is normally incident on the grating along the z-axis. In that case, as shown in Figure 2.3(b), two waveguide-array modes having real propagation constant in the z-direction are excited inside the grating layer and propagate downward along the z-axis. The criteria for the GMR to occur is that the effective index of refraction of the grating layer must be greater than the refractive index of the waveguide layer (low index layer). The effective index of the grating layer, in this case, 3.62, is greater than the refractive index of the low index layer and the refractive index of air. These two waveguide array modes (There are two waveguide array modes shown in Figure 2.3(b): forward propagating mode, represented by black rays in the waveguide layer, and backward propagating mode, represented by dashed rays) propagate until they reach the interface separating the low index and grating layers and reflecting back to themselves. Upon propagation through the HCG thickness $\mathbf{t_g}$, each propagating waveguide array mode attains a different phase which is reflected back to each other and strongly coupled into one another. Furthermore, these leaky resonant modes are partially coupled to the zeroth-order diffracted mode in the transmission region of the low-index layer. Suppose the coupling occurs so that the phase difference is 180 degrees. In that case, destructive interference of the waveguide array modes occurs, and no power is transmitted to the substrate, leading to 100% reflectivity. Such two 100 % reflectivity points are carefully optimised, as shown in[43]. As shown in Figure 2.4, a high broadband reflectivity results when such points at wavelengths 1400 nm and 1800 nm are located close together due to significant index contrast and subwavelength dimensions. It is the thickness of the subwavelength gratings that determines the phase accumulated by the waveguide array modes and affects their interference at the input and exit planes of the HCG. To make broad reflectivity, the HCG thickness should be carefully optimised such that the destructive interference is obtained at the exit plane, which cancels the transmission.

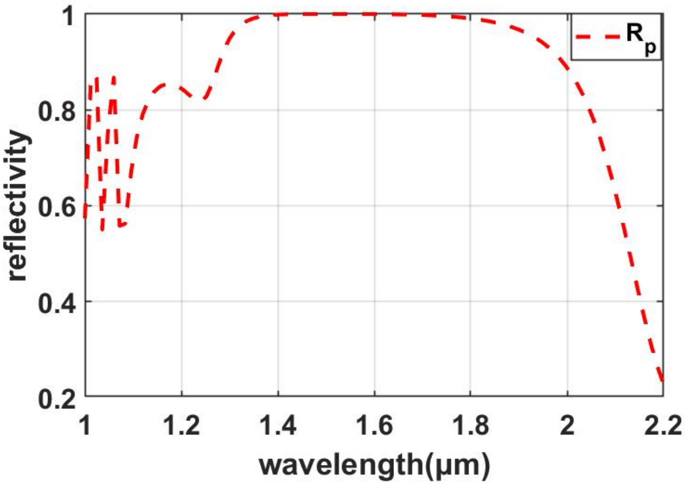

Figure 2.4. Ultra-broadband reflectivity for light polarised perpendicular to the grating lines at a centre wavelength of 1550 nm using RCWA[64]. Adapted with permission from[43] Copyright © 2004, IEEE.

This subwavelength grating under normal incidence has a very broad reflection spectrum and is widely used in applications where broad reflectivity is essential, including micro-electro-mechanical tunable devices.

2.3 NUMERICAL SIMULATIONS TO CALCULATE THE REFLECTIVITY OF LCOSDS

Simulations using numerical methods are divided into finite difference time domain method (FDTD), finite element method (FEM), rigorous coupled-wave analysis(RCWA) etc. In summary, they solve the problem by mapping electric and magnetic fields into space-time grids and looking for the solution in each grid in an iterative fashion. FDTD is very time demanding for complex optical structures such as LCoS; meanwhile, FEM and RCWA take much less time than the former.

2.3.1 Rigorous coupled-wave analysis method

RCWA is a frequency domain semi-analytic method that uses eigenmode expansion to determine far-field solutions of a multi-layered system. It is highly beneficial for calculating the reflection spectra of a grating with a periodicity. In general, RCWA is much faster than FDTD; it converts the calculation of complete electromagnetic fields in the time domain to coefficients of eigenmodes in the electromagnetic field in the frequency domain. It is highly suitable for simulating the reflection spectrum of complicated optical designs such as LCoS backplane and LCoS backplane integrated with various high contrast gratings. In this research, most of my computations are carried out with RCWA using GD-Calc.

GD calc[65] calculates the diffraction efficiency of biperiodic grating consisting of linear isotropic optical media. Figure 2.5 shows a biperiodic grating design. For example, square bars are held on top to form a biperiodic grating. This pattern extents periodically in both the x and y dimensions. Consider a position vector $\vec{r} = \hat{\imath}r_1 + \hat{\jmath}r_2 + \hat{k}r_3$ where $\hat{\imath}, \hat{\jmath}$ and $\hat{k}$ are orthonormal unit vectors. The grating structure shown in Figure 2.5 has a stack of grating strata surrounded by planes of constant r_1 , with a boundary at $r_1 = a_1[0], a_1[1] \dots \dots \dots$,

$$a_1[l_1 - 1] < r_1 < a_1[l_1] \text{ in stratum } l_1; l_1 = 1 \ldots . L_1 \tag{2.1}$$

Where L_1 is the number of strata in the grating structure. The grating is sandwiched between a substrate beneath the grating and a superstrate on top of the grating. Substrate and superstrate are considered semi-infinite strata according to equation 2.1.

i.e.,

$$-\infty = a_1[-1] < r_1 < a_1[0] \text{ in the substrate} \tag{2.2}$$

$$+\infty = a_1[L_1] < r_1 < a_1[L_1 + 1] \text{ in the superstrate} \tag{2.3}$$

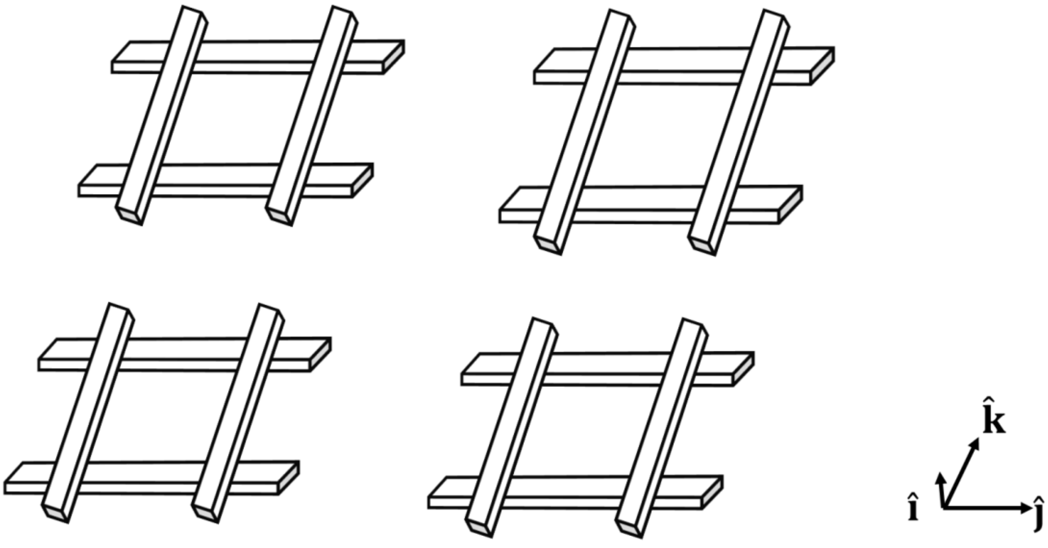

Figure 2.5. Biperiodic grating structure. Images from Ref[65].

It is essential to consider that r_1 increases towards the superstrate and the strata are numbered from substrate to superstate. The plane wave of illumination enters from the top (superstrate). The grating is assumed to have a known magnetic isotopic optical media. So, its optical properties are entirely evaluated by its scalar, complex permittivity ε. The relation between permittivity and the refractive index is $\varepsilon = (n + iq)^2$Where n is the real part of the material's RI (refractive index) and q is the extinction coefficient. The relative permittivity is 1 in free space, and the imaginary part of relative permittivity is always nonnegative according to the assumed sign convention.

$$Im[\varepsilon] \geq 0 \tag{2.4}$$

The grating is characterised by the fundamental vector periods $\vec{d_1}^{[g]}$ and $\vec{d_2}^{[g]}$ Which describes the translational symmetry of permittivity function as,

$$\vec{d_1}^{[g]} = \hat{j}d_{2,1}{}^{[g]} + \hat{k}d_{3,1}{}^{[g]} \tag{2.5}$$

$$\vec{d_2}^{[g]} = \hat{j}d_{2,2}{}^{[g]} + \hat{k}d_{3,2}{}^{[g]} \tag{2.6}$$

The vectors $\vec{d_1}^{[g]}$ and $\vec{d_2}^{[g]}$ are linearly independent.

i.e., $d_{2,1}{}^{[g]} * d_{3,2}{}^{[g]}$ is not equal to $d_{3,1}{}^{[g]} * d_{2,2}{}^{[g]}$.

The permittivity remains constant with respect to the translational displacements by either two fundamental vector periods.

$$\varepsilon\left[\vec{r} + \vec{d_1}^{[g]}\right] = \varepsilon[\vec{r}] \tag{2.7}$$

$$\varepsilon\left[\vec{r} + \vec{d_2}^{[g]}\right] = \varepsilon[\vec{r}] \tag{2.8}$$

Considering an example, Figure 2.6 represents a top view of the Figure 2.5 design, demonstrating fundamental periods $\vec{d_1}^{[g]}$ and $\vec{d_2}^{[g]}$.

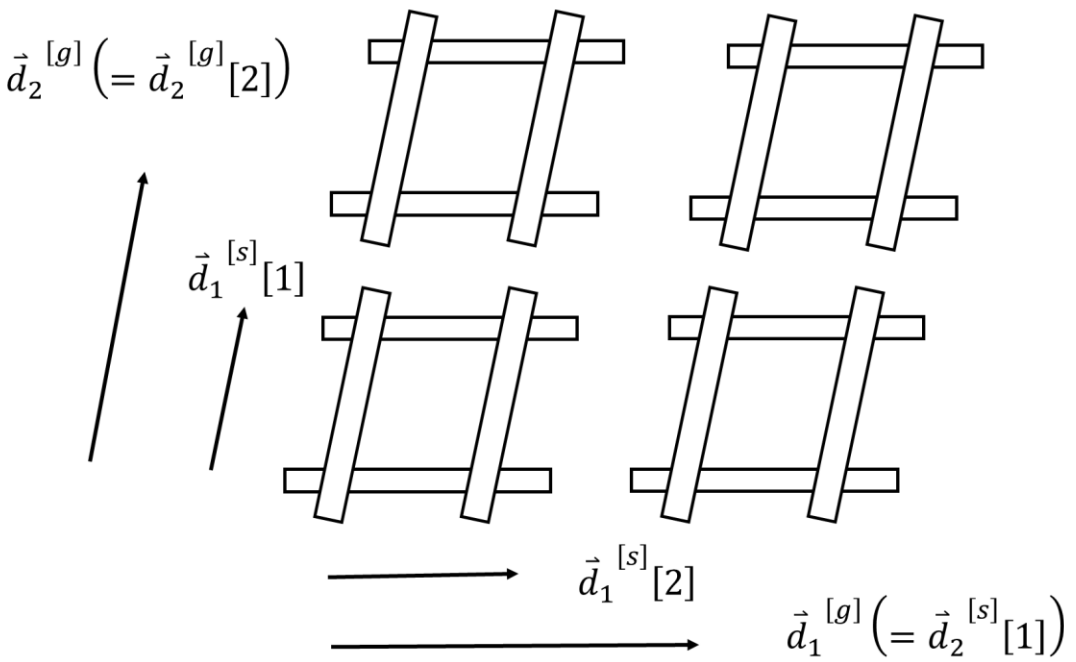

Figure 2.6. The period of bi-periodic grating illustrated the stratum-specific vectors.

$\varepsilon[\vec{r}]$ is a constant outside the grating structure, and it is independent of $\vec{r}$ within each stratum. $\varepsilon[\vec{r}]$ in substrate is $\varepsilon^{[sub]}$, while in superstrate, it is $\varepsilon^{[sup]}$. The top boundary coordinate is denoted as $a_1 l_1$ for stratum l_1 .

$$\varepsilon[\vec{r}] = \varepsilon 1[l_1][r_2, r_3] \quad \text{for } a_1[l_1 - 1] < r_1 < a_1[l_1] \tag{2.9}$$

$$\varepsilon 1[0][r_2, r_3] = \varepsilon^{[sub]} \tag{2.10}$$

$$\varepsilon 1[L_1 + 1][r_2, r_3] = \varepsilon^{[sup]} \tag{2.11}$$

The r_1 is independent of $\varepsilon 1$ since the bi-periodic grating walls are orthogonal to the substrate within every stratum. Based on equations 2.7 and 2.8, $\varepsilon 1$ satisfies the periodicity conditions.

$$\varepsilon 1[l_1]\left[r_2 + d_{2,1}^{[g]}, r_3 + d_{3,1}^{[g]}\right] = \varepsilon 1[l_1][r_2, r_3] \tag{2.12}$$

$$\varepsilon 1[l_1]\left[r_2 + d_{2,2}^{[g]}, r_3 + d_{3,2}^{[g]}\right] = \varepsilon 1[l_1][r_2, r_3] \tag{2.13}$$

Each stratum is characterised by two stratum-specific vector periods, including $\vec{d_1}^{[s]}$ and $\vec{d_2}^{[s]}$. The stratum-specific vectors are parallel to the substrate located beneath the grating and have the coordinate representations and the periods for each stratum, e.g., l_1 are denoted as $\vec{d_1}^{[s]}[l_1]$ and $\vec{d_2}^{[s]}[l_1]$. The permittivity in the stratum l_1 remains unchanged with respect to the translational displacement by $\vec{d_1}^{[s]}[l_1]$ or $\vec{d_2}^{[s]}[l_1]$ vectors.

$$\varepsilon 1[l_1]\left[r_2 + d_{2,1}^{[s]}[l_1], r_3 + d_{3,1}^{[s]}[l_1]\right] = \varepsilon 1[l_1][r_2, r_3] \qquad (2.14)$$

$$\varepsilon 1[l_1]\left[r_2 + d_{2,2}^{[s]}[l_1], r_3 + d_{3,2}^{[s]}[l_1]\right] = \varepsilon 1[l_1][r_2, r_3] \qquad (2.15)$$

The periodicity conditions mentioned in 2.14 and 2.15 are essential and relevant since they could be applied to all strata. For example, $\vec{d_1}^{[s]}[1]$ and $\vec{d_2}^{[s]}[1]$ illustrates periods for stratum 1, and $\vec{d_1}^{[s]}[2]$ and $\vec{d_2}^{[s]}[2]$ illustrates the periods for stratum 2. If $\vec{d_1}^{[s]}[l_1]$ and $\vec{d_1}^{[s]}[l_1]$ are considered in such a way that the cross product of them $\vec{d_1}^{[s]}[l_1] \times \vec{d_2}^{[s]}[l_1]$ has the least magnitude. The unit cell is defined by $\vec{d_1}^{[s]}[l_1]$ and $\vec{d_2}^{[s]}[l_1]$, probably have minimal area. These descriptions are valid for the bi-periodic stratum. Meanwhile for, a uni-periodic stratum is characterised by a single period $\vec{d_1}^{[s]}[l_1]$ which is chosen to be perpendicular to the grating lines in such a way that $\vec{d_2}^{[s]}[l_1]$ is perpendicular to the $\vec{d_1}^{[s]}[l_1]$ and having infinite length over r_2 dimension. A homogeneous stratum with a thickness consisting of a homogeneous film is not characterised by periods. $\vec{d_1}^{[s]}[l_1]$ and $\vec{d_2}^{[s]}[l_1]$ are implicitly infinite along r_2 dimension and r_3 dimensions respectively. In each stratum with corresponding periods is defined in terms of fundamental grating periods $\vec{d_1}^{[g]}$ and $\vec{d_2}^{[g]}$ and four strata-specific " harmonic indices" $h_{1,1}[l_1]$, $h_{1,2}[l_1]$, $h_{2,1}[l_1]$ and $h_{2,2}[l_1]$. For a bi-periodic stratum, the harmonic indices are non-singular.

$h_{1,1}[l_1]h_{2,2}[l_1] \neq h_{1,2}[l_1]h_{2,1}[l_1]$ (biperiodic stratum) (2.16)

And the stratum periods are defined in terms of matrix form as follows,

$$\begin{bmatrix} d_{2,1}^{[s]}[l_1] & d_{2,2}^{[s]}[l_1] \\ d_{3,1}^{[s]}[l_1] & d_{3,2}^{[s]}[l_1] \end{bmatrix} = \begin{bmatrix} d_{2,1}^{[g]} & d_{2,2}^{[g]} \\ d_{3,1}^{[g]} & d_{3,2}^{[g]} \end{bmatrix} \begin{bmatrix} h_{1,1}[l_1] & h_{1,2}[l_1] \\ h_{2,1}[l_1] & h_{2,2}[l_1] \end{bmatrix}^{-1} \tag{2.17}$$

As illustrated in Figure 2.6, the grating periods can be represented as follows: $\vec{d}_1^{\,[g]} = \vec{d}_2^{\,[s]}[1] = 2\vec{d}_1^{\,[s]}[2], \vec{d}_2^{\,[g]} = 2\vec{d}_1^{\,[s]}[1] = \vec{d}_2^{\,[s]}[2]$; in terms of matrix representation,

$$\begin{bmatrix} d_{2,1}^{[g]} & d_{2,2}^{[g]} \\ d_{3,1}^{[g]} & d_{3,2}^{[g]} \end{bmatrix} = \begin{bmatrix} d_{2,1}^{[s]}[1] & d_{2,2}^{[s]}[1] \\ d_{3,1}^{[s]}[1] & d_{3,2}^{[s]}[1] \end{bmatrix} \begin{bmatrix} 0 & 2 \\ 1 & 0 \end{bmatrix} = \begin{bmatrix} d_{2,1}^{[s]}[2] & d_{2,2}^{[s]}[2] \\ d_{3,1}^{[s]}[2] & d_{3,2}^{[s]}[2] \end{bmatrix} \begin{bmatrix} 2 & 0 \\ 0 & 1 \end{bmatrix} \tag{2.18}$$

Equation 2.18 implies the harmonic indices of stratum 1 and stratum 2 are,

$$\begin{bmatrix} h_{1,1}[1] & h_{1,2}[1] \\ h_{2,1}[1] & h_{2,2}[1] \end{bmatrix} = \begin{bmatrix} 0 & 2 \\ 1 & 0 \end{bmatrix}, \begin{bmatrix} h_{1,1}[2] & h_{1,2}[2] \\ h_{2,1}[2] & h_{2,2}[2] \end{bmatrix} = \begin{bmatrix} 2 & 0 \\ 0 & 1 \end{bmatrix} \tag{2.19}$$

For a uni-periodic stratum, the harmonic indices are $h_{1,1}[l_1] \neq 0$ or $h_{1,2}[l_1] \neq 0$; $h_{2,1}[l_1] = 0$ and $h_{2,2}[l_1] = 0$. (2.20)

Let us compute the spatial frequency vector coefficients to define the $\vec{d}_1^{\,[s]}[l_1]$,

$$\begin{bmatrix} f_{2,1}^{[s]}[l_1] & f_{3,1}^{[s]}[l_1] \end{bmatrix} = \begin{bmatrix} h_{1,1}[l_1] & h_{1,2}[l_1] \end{bmatrix} \begin{bmatrix} d_{2,1}^{[g]} & d_{2,2}^{[g]} \\ d_{3,1}^{[g]} & d_{3,2}^{[g]} \end{bmatrix}^{-1} \tag{2.21}$$

$$\begin{bmatrix} d_{2,1}^{[s]}[l_1] & d_{3,1}^{[s]}[l_1] \end{bmatrix} = \frac{\begin{bmatrix} f_{2,1}^{[s]}[l_1] & f_{3,1}^{[s]}[l_1] \end{bmatrix}}{\left[(f_{2,1}^{[s]}[l_1])^2 + (f_{3,1}^{[s]}[l_1])^2\right]} \tag{2.22}$$

For a homogeneous thin film, the harmonic indices are zero,

$$h_{1,1}[l_1] = h_{1,2}[l_1] = h_{2,1}[l_1] = h_{2,2}[l_1] = 0 \tag{2.23}$$

The grating is composed of two spatial frequency vectors, including $\vec{f_1}^{[g]}$ and $\vec{f_2}^{[g]}$, which has the cartesian coordinate representations,

$$\vec{f_1}^{[g]} = \hat{\jmath} f_{2,1}^{[g]} + \hat{k} f_{3,1}^{[g]} \tag{2.24}$$

$$\vec{f_2}^{[g]} = \hat{\jmath} f_{2,2}^{[g]} + \hat{k} f_{3,2}^{[g]} \tag{2.25}$$

The fundamental vector periods $\vec{d_2}^{[g]}$ and $\vec{d_2}^{[g]}$ are related to spatial frequency vectors in a reciprocal relationship as

$$\begin{bmatrix} f_{2,1}^{[g]} & f_{3,1}^{[g]} \\ f_{2,2}^{[g]} & f_{3,2}^{[g]} \end{bmatrix} \begin{bmatrix} d_{2,1}^{[g]} & d_{2,2}^{[g]} \\ d_{3,1}^{[g]} & d_{3,2}^{[g]} \end{bmatrix} = \begin{bmatrix} 1 & 0 \\ 0 & 1 \end{bmatrix} \tag{2.26}$$

Each stratum can be characterised by its own spatial frequency basis vectors for stratum l_1 , which have the same reciprocal relationship to the stratum basis vector periods $\vec{d_1}^{[s]}[l_1]$ and $\vec{d_2}^{[s]}[l_1]$,

$$f_1^{[s]}[l_1] = \hat{\jmath}\, f_{2,1}^{[s]}[l_1] + \hat{k} f_{3,1}^{[s]}[l_1] \tag{2.27}$$

$$f_2^{[s]}[l_1] = \hat{\jmath}\, f_{2,2}^{[s]}[l_1] + \hat{k} f_{3,2}^{[s]}[l_1] \tag{2.28}$$

$$\begin{bmatrix} f_{2,1}^{[s]}[l_1] & f_{3,1}^{[s]}[l_1] \\ f_{2,2}^{[s]}[l_1] & f_{3,2}^{[s]}[l_1] \end{bmatrix} \begin{bmatrix} d_{2,1}^{[s]}[l_1] & d_{2,2}^{[s]}[l_1] \\ d_{3,1}^{[s]}[l_1] & d_{3,2}^{[s]}[l_1] \end{bmatrix} = \begin{bmatrix} 1 & 0 \\ 0 & 1 \end{bmatrix} \tag{2.29}$$

Various types of stratum, including homogeneous, uni-periodic and bi-periodic- the basis frequency of the stratum are a linear combination of the fundamental basis frequencies of the grating.

$$\begin{bmatrix} f_{2,1}^{[s]}[l_1] & f_{3,1}^{[s]}[l_1] \\ f_{2,2}^{[s]}[l_1] & f_{3,2}^{[s]}[l_1] \end{bmatrix} = \begin{bmatrix} h_{1,1}[l_1] & h_{1,2}[l_1] \\ h_{2,1}[l_1] & h_{2,2}[l_1] \end{bmatrix} \begin{bmatrix} f_{2,1}^{[g]} & f_{3,1}^{[g]} \\ f_{2,2}^{[g]} & f_{3,2}^{[g]} \end{bmatrix} \tag{2.30}$$

The basis frequency vectors represent the reciprocal lattice vector, and the harmonic indices are analogous to Miller indices. For a uni-periodic stratum $\vec{f_1}^{[s]}[l_1] \neq 0$ and $\vec{f_2}^{[s]}[l_1] = 0$. For a bi-periodic stratum, $\vec{f_1}^{[s]}[l_1]$ and $\vec{f_2}^{[s]}[l_1]$ are non-zero and linearly independent, and for homogeneous thin film, the $\vec{f_1}^{[s]}[l_1] = \vec{f_2}^{[s]}[l_1] = 0$.

The electric field vector is characterised into two including, $\vec{E}^{[inc]}$ incident electric field vector and $\vec{E}^{[ref]}$ the reflected electric field vector in the top superstrate layer and $\vec{E}^{[tr]}$ in the bottom substrate layer. The incident optical signal is assumed to be a single-plane wave,

$$\vec{E}^{[inc]}[\vec{r}] = \vec{A}^{[inc]} e^{-i2\pi \vec{f}^{[inc]}} \cdot \vec{r} \tag{2.31}$$

Where $\vec{A}^{[inc]}$ is an amplitude vector and $\vec{f}^{[inc]}$ is the spatial frequency vector of the incident plane wave,

$$\vec{f}^{[inc]} = \hat{\imath} f_1{}^{[inc]} + \hat{\jmath} f_2{}^{[inc]} + \hat{k} f_3{}^{[inc]} \tag{2.32}$$

The reflected plane wave has an electric field $\vec{E}^{[ref]}$, consisting of a superposition of two-dimensional Fourier orders $ff\vec{E}^{[ref]}[m_1, m_2]$ with spatial-frequency vectors $\vec{f}^{[ref]}[m_1, m_2]$ which are denoted by $[m_1, m_2]$ two diffraction order indices along the x-dimension and y-dimension,

$$ff\vec{E}^{[ref]}[m_1, m_2][\vec{r}] = \vec{A}^{[ref]}[m_1, m_2] e^{-i2\pi \vec{f}^{[ref]}[m_1, m_2] \cdot \vec{r}} \tag{2.33}$$

ff denotes the two-dimensional Fourier expansion. The diffracted plane wave field's grating tangential spatial frequencies, i.e., the $\hat{\jmath}$ and $\hat{k}$ projections of spatial frequency vectors of reflected light differ from the incident field by multiples of the grating's fundamental frequency,

$$(\overrightarrow{f_2}^{[ref]}[m_1,m_2],\overrightarrow{f_3}^{[ref]}[m_1,m_2] = \left(f_2{}^{[inc]}, f_3{}^{[inc]}\right) + m_1\left(f_{2,1}^{[g]}, f_{3,1}^{[g]}\right) + m_2\left(f_{2,2}^{[g]}, f_{3,2}^{[g]}\right) \tag{2.34}$$

The plane waves' spatial frequency normal to the grating is determined from the tangential frequencies,

$$f_1{}^{[inc]} = -\surd\left({}^{\varepsilon\wedge[sup]}/_{\lambda^2} - \left(f_2{}^{[inc]^2}\right) - \left(f_3{}^{[inc]^2}\right)\right) \tag{2.35}$$

$$f_1{}^{[ref]} = -\surd\left({}^{\varepsilon\wedge[sub]}/_{\lambda^2} - \left(f_2{}^{[ref]}[m_1,m_2]^2\right) - \left(f_3{}^{[ref]}[m_1,m_2]^2\right)\right) \tag{2.36}$$

Equations 2.35 to 2.36 define the incident and reflected field's spatial frequencies based on $f_2{}^{[inc]}$ and $f_3{}^{[inc]}$and the grating frequencies. Generally, the order indices m_1 and m_2 range from $-\infty$ to $+\infty$, but only a finite number of orders were retained after computing the convergence study.

$$m_2 \in M_2 \tag{2.37}$$

$$m_1 \in M_1[m_2] \tag{2.38}$$

The m_1 the limit set is an element of M_1, a function of m_2. Consider an example as illustrated in Figure 2.7. The pair of integers represents diffraction order indices $[m_1, m_2]$.

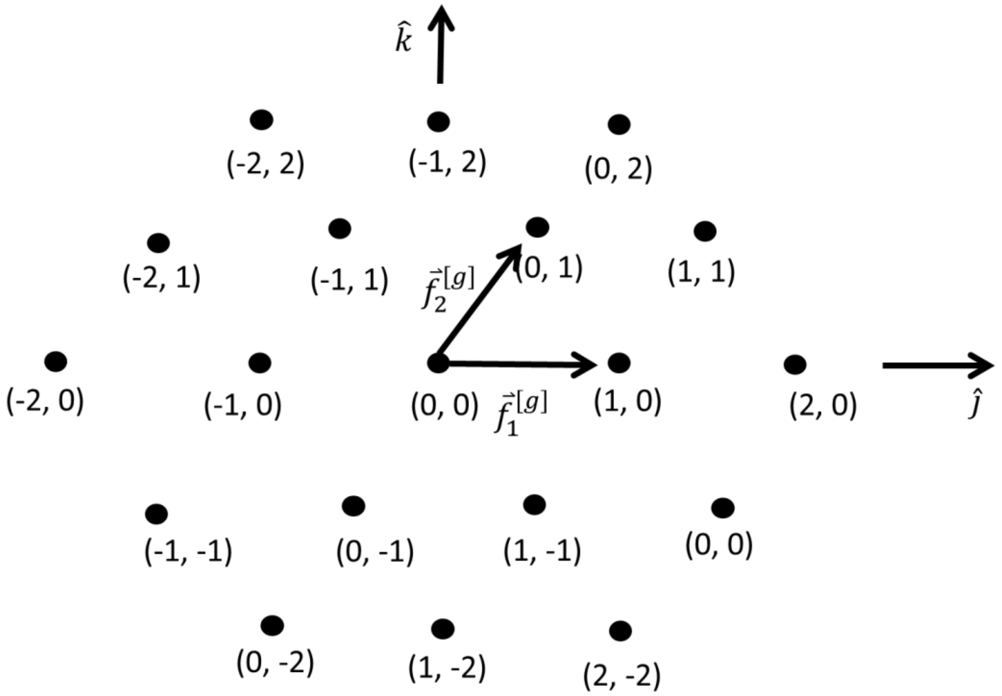

Figure 2.7. The distribution of electromagnetic field's tangential spatial frequencies[65].

If the incident field amplitude is perpendicular to $\vec{f}^{[inc]}$, then

$$\vec{f}^{[inc]} \cdot \vec{E}^{[inc]} = 0 \qquad (2.39)$$

$\vec{E}^{[inc]}$ is defined in terms of its projections onto two-unit orthonormal vectors $\hat{s}^{[inc]}$ and $\hat{p}^{[inc]}$ where $\hat{s}^{[inc]}$ is orthogonal to $\hat{\imath}$ and $\hat{p}^{[inc]}$ is orthogonal to $\hat{\jmath}$,

$$\hat{s}^{[inc]} = \hat{\jmath} {s_2}^{[inc]} + \hat{k} {s_3}^{[inc]} \qquad (2.40)$$

$$\hat{p}^{[inc]} = \hat{\imath} {p_1}^{[inc]} + \hat{\jmath} {p_2}^{[inc]} + \hat{k} {p_3}^{[inc]} \qquad (2.41)$$

The incident field can be represented as,

$$\vec{E}^{[inc]}[\vec{r}] = \hat{s}^{[inc]} E_s^{[i]}[\vec{r}] + \hat{p}^{[inc]} E_p^{[i]}[\vec{r}] \qquad (2.42)$$

$\hat{s}$ and $\hat{p}$ Orthonormal basis vectors are defined for the reflected and transmitted orders. The reflected waves are defined by,

$$\hat{s}^{[ref]}[m_1, m_2] = \hat{j}s_2{}^{[ref]}[m_1, m_2] + \hat{k}s_3^{[ref]} \tag{2.43}$$

$$\hat{p}^{[ref]}[m_1, m_2] = \hat{\imath}p_1{}^{[ref]}[m_1, m_2] + \hat{j}p_2{}^{[ref]}[m_1, m_2] + \hat{k}p_3^{[ref]}[m_1, m_2] \tag{2.45}$$

The diffracted fields from the grating are linearly dependent on the incident electric field, and the coefficients for order $[m_1, m_2]$ of reflected and transmitted waves will be represented through transmission and reflection matrices.

$$R[m_1, m_2] = \begin{bmatrix} R_{s,s}[m_1, m_2] & R_{s,p}[m_1, m_2] \\ R_{p,s}[m_1, m_2] & R_{p,p}[m_1, m_2] \end{bmatrix} \tag{2.46}$$

For defining the reflection matrix $R[m_1, m_2]$, the reflected and incident electric fields are calculated at $\vec{r} = \hat{\imath}a_1[L_1]$ on the top of the superstrate, as mentioned in equation 2.26. The two-dimensional Fourier transform of the **s** and **p** components of the electric field at the superstrate is defined by the matrix,

$$\begin{bmatrix} ffE_s^{ref}[m_1, m_2]\hat{\imath}a_1[L_1] \\ ffE_p^{ref}[m_1, m_2]\hat{\imath}a_1[L_1] \end{bmatrix} = \begin{bmatrix} R_{s,s}[m_1, m_2] & R_{s,p}[m_1, m_2] \\ R_{p,s}[m_1, m_2] & R_{p,p}[m_1, m_2] \end{bmatrix} \begin{bmatrix} E_s^{inc}\left[\hat{\imath}a_1[L_1]\right] \\ E_p^{inc}\left[\hat{\imath}a_1[L_1]\right] \end{bmatrix} \tag{2.47}$$

The power associated with the incident electric field propagating towards the grating is,

$$P^{[inc]} = -\left(\left|E_s^{[inc]}\right|^2 + \left|E_p^{[inc]}\right|^2\right) Re[\lambda f_1^{[inc]}] \tag{2.48}$$

Similarly, the reflected power $P^{[r]}[m_1, m_2]$ propagating away from the grating in the $+\hat{j}$ the direction in the order $[m_1, m_2]$ is,

$$P^{[ref]}[m_1,m_2] = \left(\left|ffE_s^{ref}[m_1,m_2]\right|^2 + \left|ffE_p^{ref}[m_1,m_2]\right|^2\right) Re\left[\lambda f_1^{[ref]}[m_1,m_2]\right] \tag{2.49}$$

The incident field amplitude and the reflected field amplitude are evaluated implicitly at $\vec{r} = \hat{\imath}a_1[L_1]$ in equations 2.48 and 2.49. Then the reflected diffraction efficiency is the ratio of incident power to reflected power,

$$\begin{aligned}\eta^{ref}[m_1,m_2] &= \frac{P^{[ref]}[m_1,m_2]}{P^{[inc]}} \\ &= \left(\frac{\left(\left|ffE_s^{ref}[m_1,m_2]\right|^2 + \left|ffE_p^{ref}[m_1,m_2]\right|^2\right) Re\left[\lambda f_1^{[ref]}[m_1,m_2]\right]}{-\left(\left|E_s^{[inc]}\right|^2 + \left|E_p^{[inc]}\right|^2\right) Re[\lambda f_1^{[inc]}]}\right)\end{aligned} \tag{2.50}$$

For linearly s-polarised input light,

$\left|E_s^{[inc]}\right| = 1, \left|E_p^{[inc]}\right| = 0$, By substituting in equation 2.47 → $\left|E_s^{ref}[m_1,m_2]\right| = R_{s,s}[m_1,m_2]$ and $\left|E_p^{ref}[m_1,m_2]\right| = R_{p,s}[m_1,m_2]$ Substituting in equation 2.50 implies,

$$\begin{aligned}R_s &= \left|\eta^{ref}[m_1,m_2]\right| = \text{Reflection efficiency for s} - \text{polarised input light} \\ &= \left(\frac{\left(\left|ffR_{s,s}[m_1,m_2]\right|^2 + \left|ffR_{p,s}[m_1,m_2]\right|^2\right) Re\left[\lambda f_1^{[ref]}[m_1,m_2]\right]}{Re[\lambda f_1^{[inc]}]}\right)\end{aligned}$$

GD-calc uses two methods to compute the diffraction efficiency of the structure; one is the S-matrix method, and the other is the fast Fourier factorisation method. The numerical algorithms are outlined in[65].

2.3.1.1 Reflection efficiency of an LCoS backplane without pixels and with grating using RCWA

An LCoS without pixels and grating has dimensions mentioned in[40] at the C-band operation. GD-Calc uses MATLAB environment to compute the diffraction efficiency from a grating structure. GD-Calc is limited by the requirement that gratings must be composed of optically homogeneous regions with boundaries that are parallel to a specified set of primary coordinate planes. GD-Calc has the advantage of diffraction order selection. Different stratum types define the grating; homogeneous stratum has grating layers with no stripe boundaries, uni-periodic stratum with homogeneous stripes and bi-periodic stratum with block boundaries, as illustrated in Figure 2.8. The analogy to the mesh size for performing convergence analysis in RCWA is the maximum number of orders retained in the computation.

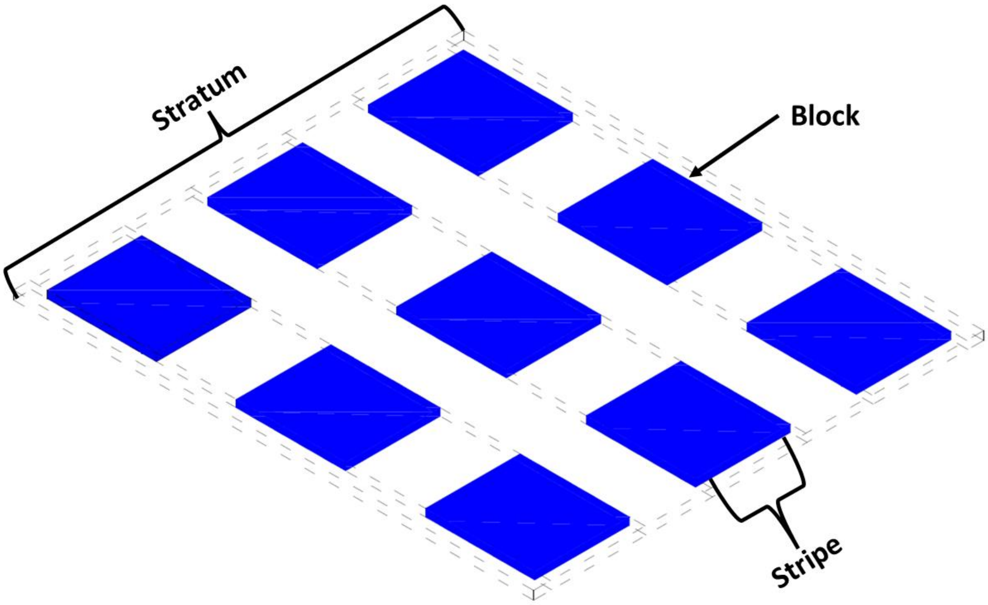

Figure 2.8. Illustrated an example of a grating stratum with stripes and blocks[65].

Let's consider the LCoS backplane structure mentioned in[48], which has a uni-periodic silicon HCG structure on top of the aluminium layer with a finite thickness of 80 nm. The grating's duty cycle (33%) is the fraction of high-index material to the low-index material surrounding it. The grating periodicity is 850 nm, and the width of high index material is 280 nm. The rectangular silicon rods are surrounded by low-index silica material. The thickness of silica below the grating is 210 nm, and the thickness above the grating is 100 nm. A plane wave with normal incidence with the direction of propagation along the z-dimension is incident on the grating surface, as shown in Figure 2.9. I have set the silica layer on top as the superstrate and air as the substrate.

The harmonic indices are chosen in such a way that the stripes are parallel to the fundamental grating vector periods $\vec{d}_2^{\,[g]}$ and have a periodicity defined by $\vec{d}_1^{\,[g]}$ with assigned values $h_{11} = 1$ and $h_{12} = 0$. Each stripe has boundary positions defined by the grating's duty cycle, which in turn determines one of the stripe's wall positions. The silica layer above the Silicon rectangular rod is a homogeneous layer with no stripe boundaries. The Aluminium layer with a finite thickness beneath the low index layer is also a homogeneous layer with no block boundaries. The low-index silica layer below the grating is also a homogeneous layer with a finite thickness along the z-dimension. More details of the implementation of the uni-periodic HCG are outlined in Appendix A. The schematic of the simulated structure is shown below in Figure 2.9.

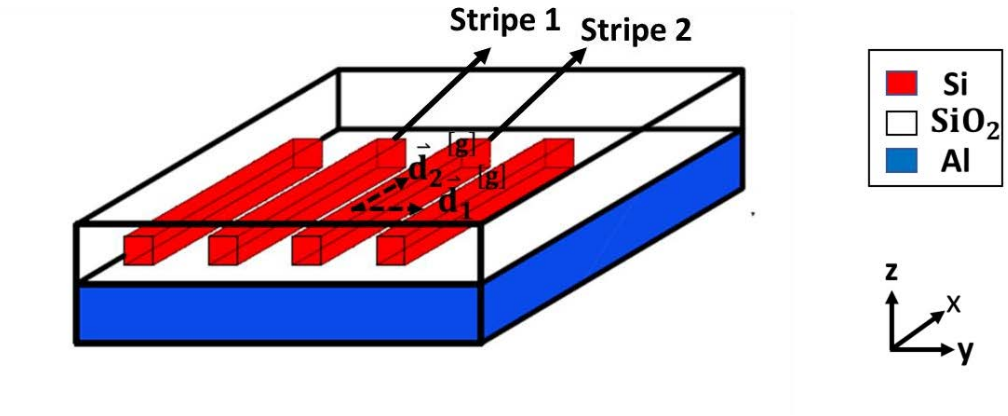

Figure 2.9. Illustrated an LCoS backplane without the pixels and uni-periodic silicon rectangular subwavelength gratings with stripes and fundamental grating periods in the RCWA platform.

Convergence analysis was performed to test the accuracy of the simulation. I have simulated the structure as shown in Figure 2.9 with a center wavelength of 1550 nm. Figure 2.10 (a) shows the simulated reflectivity over C-Band. The reflectivity LCoS backplane with silicon HCG converges at m_max=5, as illustrated in the convergence analysis in Figure 2.10 (b, c, d). Ideally, a logarithmic error of $10^{(-1)}$ is enough to obtain reasonable accuracy. However, $10^{(-5)}$ precision for R_S and R_P is useful for simulating complex structures like the LCoS backplane. Figure 2.10(e) shows the performance enhancement after the addition of HCG.

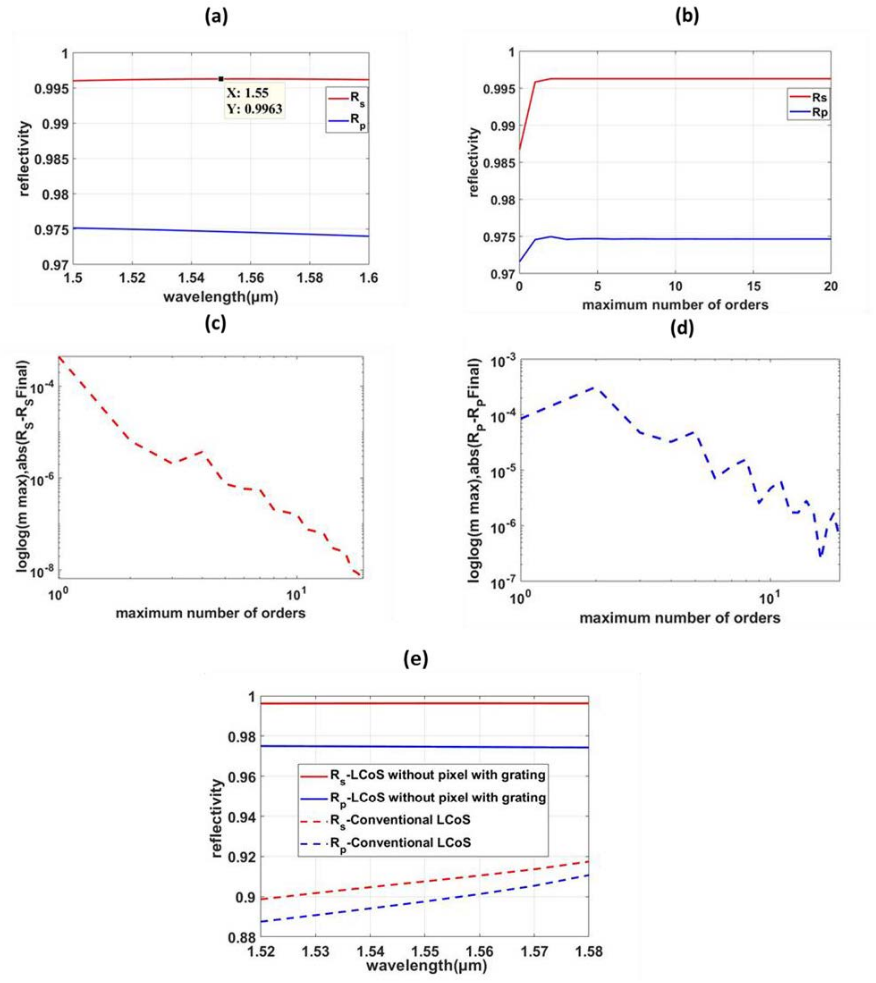

Figure 2.10 (a, b, c, d, e). Reflectivity of LCoS without pixels and with grating and convergence analysis. (a) Illustrates the simulated reflectivity of R_S and R_P over the C-band**.** (b) Illustrates the simulated reflectivity with R_s and R_p converges at a maximum number of orders=5. (c) Illustrates R_s linear, logarithmic convergence analysis with $10^{(-6)}$ error approaches at a maximum order=5. (d) Illustrates the linear, logarithmic convergence analysis where the R_p at 1550 nm converges at the maximum number of orders=5 with an error of $10^{(-5)}$. (e) Comparison of the reflectivity of LCoS with grating-without pixel and conventional LCoS.

2.3.2 Finite-difference time-domain(FDTD) method

FDTD is a state-of-the-art method for solving Maxwell's equation in complex geometries. It is a direct time and space solution such that FDTD offers solutions to various problems in electromagnetics and photonics. Kane Yee first proposed the FDTD method[66] in 1966. In addition, FDTD can also obtain the frequency solution by applying Fourier transforms, leading to the complex Poynting vector and the transmission reflection of light.

The finite difference time domain method solves Maxwell's curl equation in non-magnetic field materials.

$$\frac{\partial \boldsymbol{D}}{\partial t} = \nabla \times \boldsymbol{H} \text{……….} \ (1)$$

Where $\boldsymbol{D(\omega)}=\epsilon_0 \ \epsilon_r(\omega)\mathbf{E} \ (\omega)$………..(2)

$$\frac{\partial \boldsymbol{H}}{\partial t} = \frac{-1}{\mu_0} \nabla \times \boldsymbol{H} \text{……} \ (3)$$

$\epsilon_r(\omega)$=Complex relative dielectric constant=n^2; n is the refractive index.

In 3D; Maxwell's equation has six electro-magnetic field components they are,E_x, E_y and E_z andH_x, H_y and H_z. Let us assume that the structure is infinite in z-dimension and that the fields are independent of z. Then,

$$\epsilon_r(x, y, z, \omega) = \epsilon_r(x, y, \omega) \text{………} \ (4)$$

Also,

$$\frac{\partial \boldsymbol{E}}{\partial z} = \frac{\partial \boldsymbol{H}}{\partial z} = 0 \text{………..} \ (5)$$

Then Maxwell's equations split into two independent sets of equations composed of three vector quantities, each of which can only be solved in the x-y plane. These are the transverse electric(TE) and transverse magnetic(TM) equations. We can solve both sets of the equation with the following components;

TE: E_x, E_y, H_z.

TM: H_x, H_y, E_z.

For example, in the TM case, Maxwell's equation reduces to;

$$\frac{\partial}{\partial t}\left(\hat{x}\,D_x + \hat{y}\,D_y + \hat{z}D_z\right) = \begin{matrix} \hat{x} & \hat{y} & \hat{z} \\ \frac{\partial}{\partial x} & \frac{\partial}{\partial y} & \frac{\partial}{\partial z} \\ H_x & H_y & H_z \end{matrix}$$

By solving the above,

We get,

$$\frac{\partial D_Z}{\partial t} = \frac{\partial H_y}{\partial x} - \frac{\partial H_x}{\partial y} \ldots\ldots\ldots \text{(6)}$$

Also,

$$D_Z(\omega) = \epsilon_0\, \epsilon_r(\omega) Ez\,(\omega) \ldots\ldots\ldots\ldots \text{(7)}$$

Also,

$$\frac{\partial}{\partial t}\left(\hat{x}\,H_x + \hat{y}\,H_y + \hat{z}\,H_z\right) = \frac{-1}{\mu_0} \begin{matrix} \hat{x} & \hat{y} & \hat{z} \\ \frac{\partial}{\partial x} & \frac{\partial}{\partial y} & \frac{\partial}{\partial z} \\ E_x & E_y & E_z \end{matrix}$$

Then we get,

$$\frac{\partial H_x}{\partial t} = \frac{-1}{\mu_0}\frac{\partial E_z}{\partial y} \ldots\ldots (8)$$

$$\frac{\partial H_y}{\partial t} = \frac{1}{\mu_0}\frac{\partial E_z}{\partial x} \ldots\ldots. (9)$$

Thus the FDTD method solves equations (6), (8), and (9) on a discrete spatial and temporal grid, as shown in Figure 2.11, named Yee cell[66].

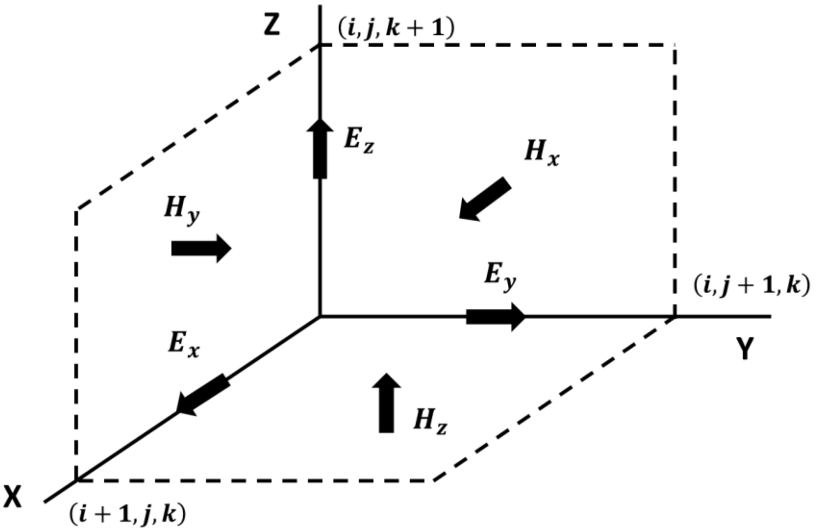

Figure 2.11. Schematic representation of Yee cell. The figure shows the electric fields along the cube edges; magnetic fields are on the cube faces. The cell origin is at (i,j,k). Every E field is located ½ cell width from the origin in the direction of its orientation. Every H field offset found ½the cell in each direction except its orientation. Reproduced from Ref[66] with permission from © 1966, IEEE.

2.3.2.1 Reflection efficiency of a uni-periodic grating using the 2D-FDTD method

Figure 2.12 demonstrates the LCoS backplane design schematic diagram in[40] the 2D-FDTD platform. A finite difference time domain developed by Lumerical Solution

Inc. is used to evaluate the reflectivity of the LCoS backplane. The perfectly matched layer (PML) boundary conditions are set along the Y-direction to absorb the incident light with the least reflections. PMLs are impedance matched[67-68] with the surrounding substrate and superstate to minimise the reflections. However, in reality, minimal reflections will always show up due to the discretization of the PML equations. Meanwhile, a periodic boundary condition is set along the X-direction. The grating is extended infinitely in the Z-direction, and the direction of the plane wave propagation is along the Y-direction with electric field oscillation in the X-direction. A frequency-domain power monitor is placed between the source and the PML located on top.

The unit cell of the high reflectivity backplane has a periodicity of 850 nm, a duty cycle of 33%, a thickness of the low index layer of 210 nm, a thickness of silica on top of 100 nm and silicon as a substrate having infinite thickness. It is hard to obtain the correct answer in numerical simulation; some numerical error always appears. One significant source of error is the non-uniform overlapping of the mesh region with the simulating structure. The acceptable level of error can be quantified by changing the mesh size. Therefore, convergence analysis was performed by changing the mesh size covering the aluminium metal layer. The mesh size varied from 5 nm* 5 nm to 35 nm* 35 nm and reflectivity for the s-polarised input light R_s's linear, logarithmic error was calculated. The finer mesh size of 10 nm* 10 nm approaches a linear, logarithmic error of 10^{-3} as shown in Figure (a), which is the least error for reasonable accuracy. Also, the mesh region covering the aluminium layer has 25 nm*25 nm size approaches 10^{-3} linear, logarithmic error. The reflectivity for s-polarised input light was simulated over C-band with a mesh size of 25 nm*25 nm and 10 nm*10 nm. For 25 nm*25 nm mesh, the reflectivity was found to be 99.76%, and for 10 nm* 10 nm, the reflectivity is 99.9% at 1550 nm, as shown in Figure 2.13(b). An acceptable error level of about 10^{-3} operated at a mesh accuracy of 4 with a mesh size of 10 nm*10 nm provides the least computational error. A comparison study of the reflectivity simulated via RCWA and FDTD was performed. The comparison shows a broad reflection efficiency of more than 99.6% over the C-band, verifying the accuracy of the numerical simulation.

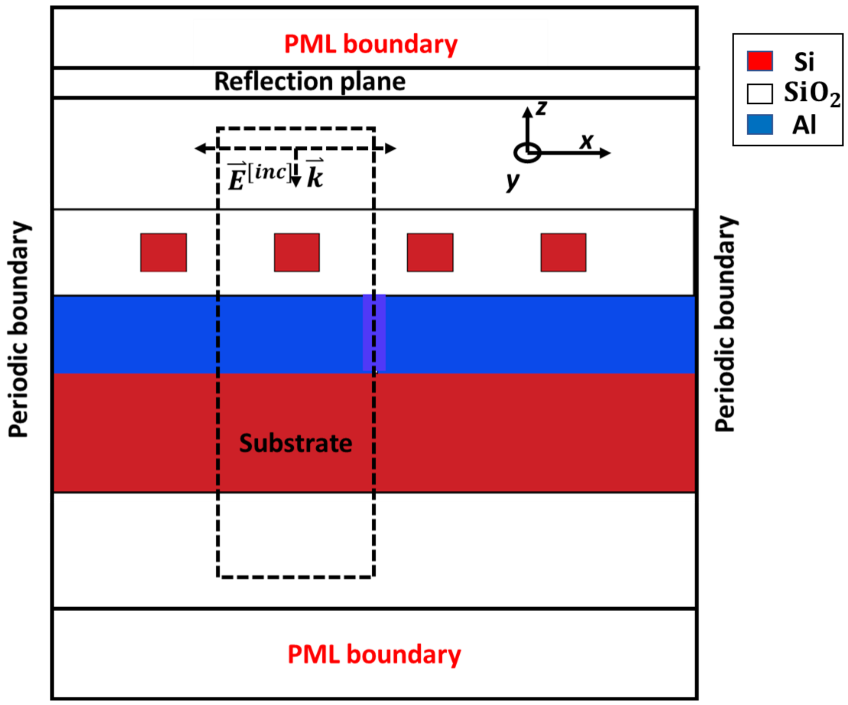

Figure 2.12. Schematic diagram of the LCoS backplane with one-dimensional uniperiodic silicon high contrast subwavelength grating. The dashed line represents the unit cell of the subwavelength grating in the LCoS backplane.

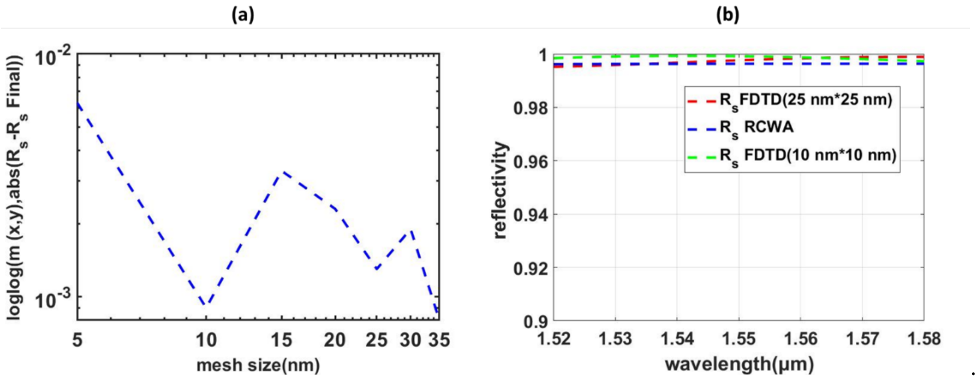

Figure 2.13(a, b). (a) Convergence analysis of LCoS backplane with one-dimensional uni-periodic silicon HCG using FDTD method. The linear, logarithmic error approaches $10^{(-3)}$ at mesh size along the x-dimension, and the y-dimension becomes 10 nm. (b) Comparison of the reflectivity using FDTD and RCWA. Simulated reflectivity of s-polarised input light using 2D-FDTD (red) using 25 nm*25 nm mesh size and 10 nm* 10 nm mesh size(green) over the C-Band and RCWA (blue). At the central wavelength of 1550 nm, the reflectivity corresponding to the s-polarised input light is more than 99.76% for both mesh sizes.

2.3.3 Comparison of the FDTD and RCWA

For complex optical structures such as the LCoS backplane, the RCWA method is more efficient. An LCoS backplane involves many layers, including homogeneous layers, uni-periodic grating, bi-periodic grating, grating inscribed in another layer and lock-like structures. If we perform a convergence study using the mesh analysis of the FDTD, these computations require a vast amount of time for an LCoS structure with pixels and grating. Also, FDTD is sensitive to mesh size. The computational costs can be drastically reduced if we implement the RCWA. For RCWA, a plane wave excitation and a plane wave solution are assumed in the far field. The convergence analysis in RCWA takes much lesser time compared to FDTD. Since the structures involved in the LCoS backplane have rectangular geometry, FDTD is reasonably accurate if we set the design parameters correctly.

A conventional LCoS backplane structure consists of bi-periodic aluminium pixels with an interpixel gap filled with silica. The pixel structure has a periodicity of 9.2 microns along the x-dimension and 9.18 microns along the y-dimension. The simulation time required to evaluate the unit cell over 10 points of wavelength over the c-band with a spacing of 10 nm requires almost 24 hours. Because of all these reasons, I mostly use RCWA instead of FDTD to design and simulate LCoS backplane structures. However, I have implemented 3D-FDTD to validate the near-field optical analysis of the pixelated structure to observe the standing waves' generation above the pixel layer and below the cap layer. Lumerical FDTD has a better graphical user interface and has the advantage of interoperability with other simulation environments like MATLAB. I have post-processed the data from near-field optical analysis with MATLAB directly from Lumerical.

3 CHAPTER 3: DESIGN OF HIGH REFLECTIVITY LCOSDS WITHOUT PIXELS IN NEAR-INFRARED

This chapter presents the introduction of high-contrast gratings in the LCoS platform. Here I have performed optimisation algorithms to introduce the broad reflectivity in LCoS in two important wavelength regimes: C-band (1520 nm to 1580 nm) and 1064 nm. The industry partner provided the grating parameters optimised and tested at the C-band of operation.

3.1 INTRODUCTION TO SUBWAVELENGTH HCGS

Diffraction gratings are very important in the field of optics. There are three regions of operations for diffraction gratings, including diffraction regime[69-70], deep subwavelength regime and near subwavelength regime. Diffraction regime refers to the regime in which the periodicity of the grating is comparable to the wavelength of the incident light. When the periodicity of the grating is much less than the wavelength of incidence, the diffraction grating operates in a deep subwavelength[71] regime. When the periodicity is less than the wavelength of the grating material and surrounding media, the region of diffraction is known as the subwavelength regime. The subwavelength regime exhibits distinct features compared to the typical diffraction grating. This uniqueness becomes pronounced when there is a significant refractive index contrast between the high-index grating bar and the surrounding medium. These features include high broadband reflectivity, broadband transmissivity and high-quality factor resonances[42-43, 72-73]. In this chapter, I model silicon HCG structures having near-subwavelength dimensions that enhance the reflection efficiency of conventional

LCoS. The feature of broadband reflection efficiency of subwavelength high contrast gratings is desirable for the performance enhancement of high reflectivity LCoS.

3.2 HCG STRUCTURES FOR HIGH REFLECTIVITY LCOSDS IN NEAR INFRA-RED

HCG with subwavelength dimensions can be applied to the front surface of an LCoS structure to pronounce the reflectivity to more than 99%. Adding multiple layers of dielectric coating may lead to inherent voltage fall created by the layers to suppress the pixel design. Due to coating stress, the flat optics concept would be difficult to achieve with the distributed Bragg mirror coating. Silicon HCG can make the device optically flat and enhance the performance of LCoSDs. Though DBR fabrication is less expensive than optical lithography, the coating stress and fringing field effects make the device less attractive. Inscribing a uni-periodic HCG on the front surface of LCoS backplane is a simple process using optical lithography, which ultimately enhances the performance of LCoSDs.

3.3 RESULTS AND DISCUSSION

3.3.1 Design of silicon high contrast grating in near infra-red

Silicon HCG structures are placed between the LC material and the electrode, as shown in Figure 3.1. The periodicity of the grating is uni-periodic and extends longitudinally along the x-dimension. The silicon grating bars are surrounded by a lower refractive index material, silicon dioxide (silica). At C-band operation, the refractive index of silica is about 1.5, and that of silicon is about 3.4. The significant difference in refractive index and near subwavelength dimensions of periodicity leads to high reflectivity over a broad wavelength range. As the refractive index contrast rises, the reflection efficiency broadens. The structure defined in[40] has a refractive index contrast of about 1.9, leading to a broader reflection of 60 nm bandwidth in the C-band with more than 99.5% reflectivity. The low index layer thickness is crucial for obtaining the mirror effect. The critical design parameters are the periodicity of the grating, duty cycle, grating thickness and thickness of the low index layer. I have designed and optimised the structure in two important near-infra-red wavelength regimes to observe the high reflection efficiency and design tolerance.

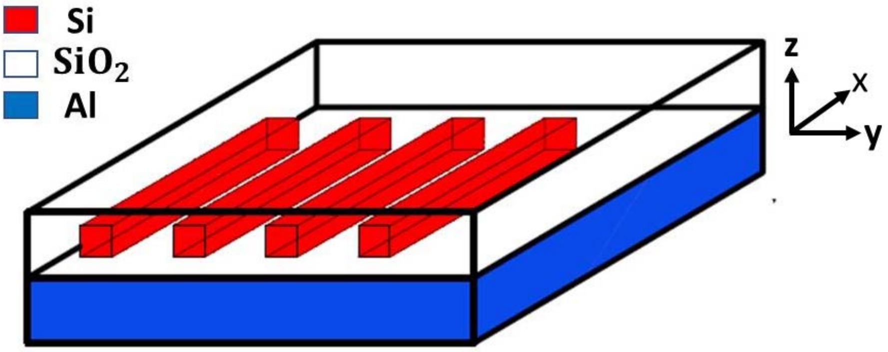

Figure 3.1. Schematic view of one-dimensional uni-periodic Si-high contrast grating structure without pixels and Al layer.

As discussed in chapter 2, the simulations are performed with GD-Calc using RCWA. More details of the simulation using GD-Calc are described in detail in Appendix A. The cap layer in the design is silica and is located on top of the high-contrast grating. The substrate is air, and the superstrate is silica in this design. The optimal grating parameters were obtained using two-dimensional grid optimisation, where the reflectivity of the grating is plotted as a function of grating parameters over a 2D grid. The initial grating parameters at 1550 nm were obtained from[48] and simulated over a two-dimensional grid. The grating period is crucial so that it determines the centre wavelength. The centre wavelengths as 1550 nm and 1064 nm have been set initially to perform the two-dimensional grid optimisation to optimise the grating parameters at these wavelengths. The reflectivity of s-polarised input light as a function of grating periodicity and width of silicon was simulated over a two-dimensional grid.

The 2D-grid optimisation is explained as follows: The grid consists of the grating period and width of silicon, and the optimal point corresponding to the maximum reflectivity was found. The point must be located inside the grid to be optimal. If the point corresponds to the optimal point situated on the edge of the grid, the range of the grating parameter must be extended until it is found inside the grid. A periodic boundary condition is set along the y-dimension where the periodicity exists. After completing two-dimensional grid optimisation, the reflected power for s and p polarisations was obtained for each variable combination. The optimised grating parameters at 1550 nm were found to be; periodicity(**d**) is 820 nm, the width of silicon(**w**) is 300 nm, grating thickness($\mathbf{t_g}$) is 180 nm, and the thickness of low index layer($\mathbf{t_l}$) is 210 nm. The reflection efficiency is over 60 nm at a central wavelength of 1550 nm. In the case of optimising the structure at 1064 nm, the optimised parameter at 1550 nm (provided by industry) is scaled by multiplying it by a constant of 1.064 and setting those parameters as initial grating parameters for repeating the performance at 1550 nm. The optimal grating parameters were found to be; periodicity(d) is 610 nm, the width of silicon(w) is 177 nm, grating thickness(t_g) is 170 nm and thickness of the low index layer(t_l) is 200 nm. Figure 3.2(a) shows the broad reflection efficiency over 60 nm centered at 1550 nm, and Figure 3.2(b) shows the broad reflection efficiency over the 40 nm band centered at 1064 nm.

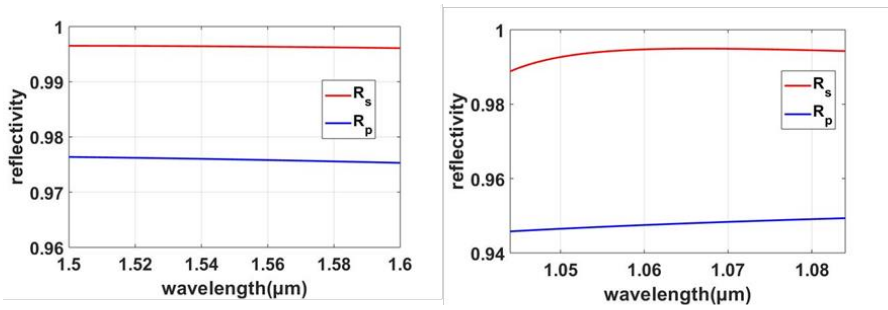

Figure 3.2 (a, b). Broad high reflectivity in near-infrared wavelengths. The broad high reflection efficiency of high contrast grating structure for silicon high contrast grating structure centered at 1550 nm (a) and 1064 nm (b) with optimised parameters corresponding to orthogonal (**s**(red) and **p**(blue)) polarisations.

Figure 3.3(a) shows that the two-dimensional grid is simulated over a grid consisting of 51*51 grid points. The **s** component of reflectivity is evaluated as a function of silicon's width and the periodicity of HCG; the reflectivity maximum is spotted on the surface plot, as shown in Figure 3.3 (a). The optimised periodicity and width of silicon are 820 nm and 299 nm, respectively, resulting in a duty cycle of 36%. Figure 3.3(b) shows the fabrication tolerance of the width of silicon. The R_S is more than 99.5%, with a width of Si varying from 200 nm to 400 nm. Excellent agreement regarding the consistency between Figure 3.3 (a) and Figure 3.3 (b) was obtained since the point on both plots corresponds to identical grating parameters. Both points were simulated with exact parameters that provide 99.6% reflection efficiency. Figure 3.3 (c) presents the two-dimensional grid with a grid size of 51*51 consisting of reflectivity as a function of grating thickness and wavelength. The fabrication tolerance of grating thickness would be 180 nm ± 60 nm to maintain the **s** component of reflection efficiency of more than 99% at 1550 nm. Excellent agreement regarding the consistency between Figure 3.3 (a), Figure 3.3 (b) and Figure 3.3 (c) was obtained since the point on all the plots correspond to identical grating parameters. Figure 3.3 (d) consists of reflectivity as a function of the wavelength and thickness of the low index layer. Excellent agreement regarding the consistency between Figure 3.3 (a), Figure 3.3 (b), Figure 3.3 (c), and Figure 3.3 (d) was obtained since the point on all the plots correspond to identical grating parameters. The fabrication tolerance of the thickness of the low index layer would be 210 ±90 nm to maintain a reflection efficiency of more than 99%. The optimisation results are summarised in the table, as shown in Table 3.1.

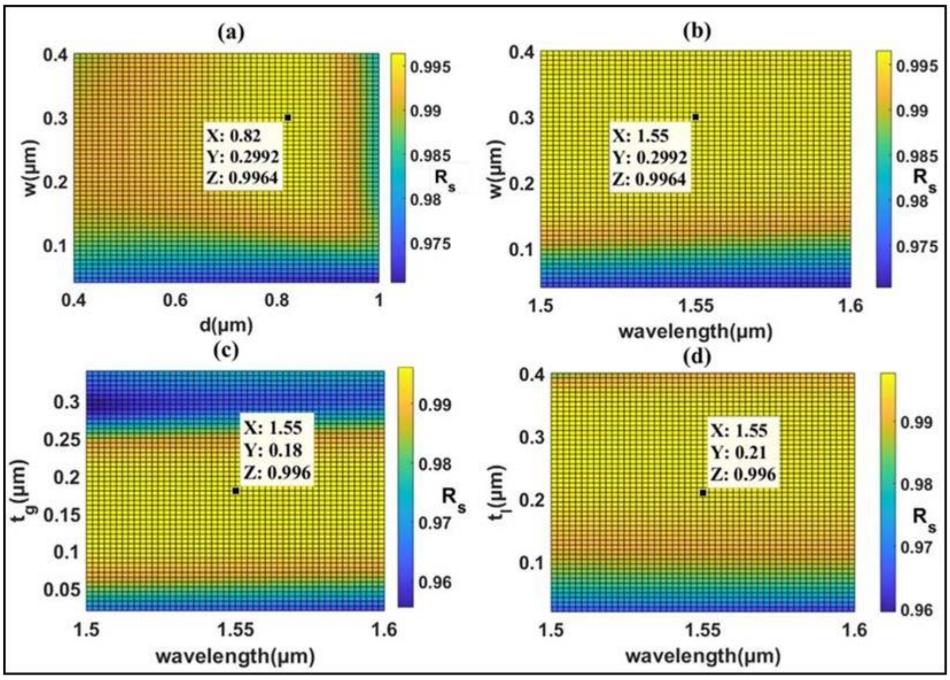

Figure 3.3 (a, b, c, d). Optimisation and fabrication tolerance of LCoS without pixels and with grating. (a) The two-dimensional grid consists of the width of silicon(w) along the x-axis and period(d) along the y-axis against the R_s component of reflection efficiency with a grid size of 51*51. The optimised value of period and width of Si for a maximum reflectivity of 99.6% as 820 nm and 299 nm, respectively. (b) A two-dimensional grid showing the fabrication tolerance of the width of Si along with the x-axis and wavelength band along the y-axis against the R_s component of reflection efficiency-optimised width of Si is 299 nm. (c) The two-dimensional grid shows the fabrication tolerance of grating thickness and its optimised value of 180 nm. (d) Two-dimensional grid showing the fabrication tolerance of low index layer and its optimised value is 210 nm.

Wavelength of incidence	Optimal periodicity(d) at 1550 nm	Optimal width of Si(w) at 1550 nm ±tolerance	Optimal grating thickness(t_g) at 1550 nm ±tolerance	Optimal thickness of low index layer(t_l) at 1550 nm ±tolerance
1500 nm-1600 nm	820 nm	300 nm ±100 nm (more than 99.5% of R_S)	180 nm ±60 nm (more than 99% of R_S)	210 nm ±90 nm (more than 99% of R_S)

Table 3.1. Optimised parameters and fabrication tolerances at around 1550 nm.

The optimisation for 1064 nm wavelength is shown in Figure 3.4(a,b,c,d); The two-dimensional grid, as shown in Figure 3.4(a), is simulated over a grid consisting of 51*51 grid points. The **s** component of reflectivity is evaluated as a function of silicon's width, and the periodicity of HCG and maxima is spotted on the surface plot, as shown in Figure 3.4(a). The optimised periodicity and width of silicon are 610 nm and 177 nm, respectively, resulting in a duty cycle of 29%. Figure 3.4(b) shows the fabrication tolerance of the width of silicon. The R_S is more than 99.5%, with a width of Si varying from 200 nm to 400 nm. Excellent agreement regarding the consistency between Figure 3.4 (a) and Figure 3.4(b) was obtained since the point on both plots corresponds to identical grating parameters. Both points were simulated with exact parameters that provide 99.5% reflection efficiency. Figure 3.4(c) presents the two-dimensional grid with a grid size of 51*51 consisting of reflectivity as a function of grating thickness and wavelength. The fabrication tolerance of grating thickness would be 170 nm ± 20 nm to maintain the **s** component of reflection efficiency of more than 99% at 1064 nm.

The narrow minima determined by the grating thickness appearing in the reflectance spectra near the wavelength of 1064 nm are due to constructive interference of the two waveguide array modes at both the input and exit planes of the silicon grating bars. The HCG with an aluminium layer at the bottom acts as a high-Q[74-75] resonator; each waveguide array mode strongly couples to each other at the input plane vanishing reflection. So it can be interpreted as a constructive interference at the grating bottom, including grating bars, low index layer, and the Aluminium layer top interface. The reflectivity spectrum (Figure 3.4 (c)) shows that the resonant grating exhibits high-Q resonances at around 1064 nm, characterised by asymmetric transitions from 99% to ~0% reflectivity. The optimal grating thickness of 170 nm is chosen to have maximum reflectivity at a wavelength of incidence of 1064 nm with broad reflectivity. The HCG acts as a high-Q-resonator at a grating thickness of 203 nm without conventional mirrors. Figure 3.4 (d) consists of reflectivity as a function of the wavelength and thickness of the low index layer. Excellent agreement regarding the consistency between Figure 3.4 (a), Figure 3.4 (b), Figure 3.4 (c), and Figure 3.4 (d) is attained since the point on all the plots correspond to identical grating parameters.

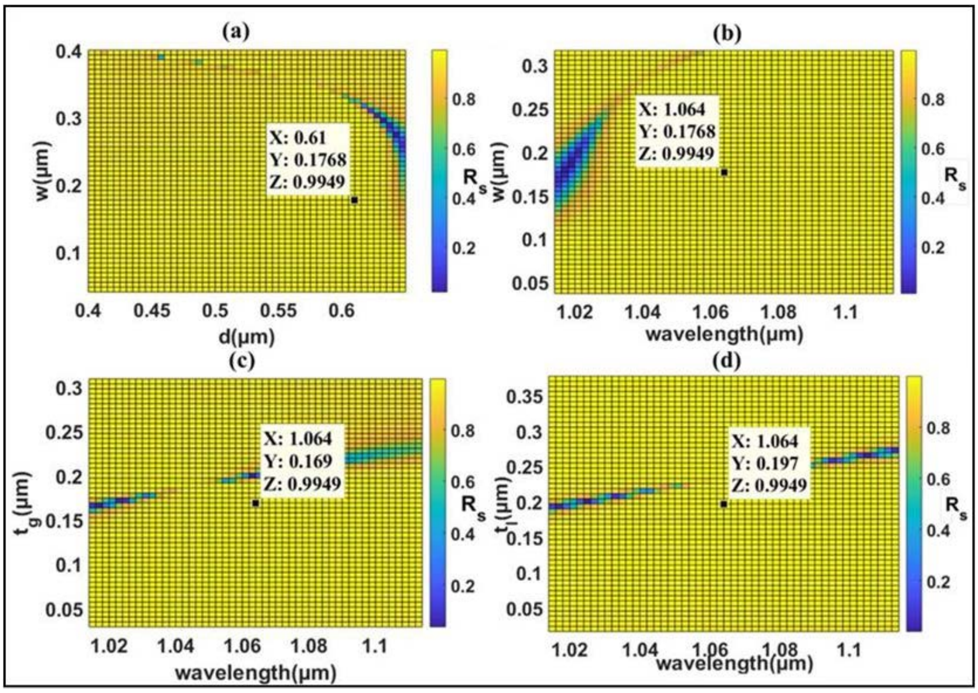

Figure 3.4 (a, b, c, d). Optimisation and fabrication tolerance of LCoS without pixels and grating at around 1064 nm. (a) The two-dimensional grid consists of the width of silicon(w) along the x-axis and period(d) along the y-axis against the R_s component of reflection efficiency with a grid size of 51*51. The optimised value of period and width of Si for a maximum reflectivity of 99.5% as 610 nm and 177 nm, respectively. (b) A two-dimensional grid showing the fabrication tolerance of the width of Si along with the x-axis and wavelength band along the y-axis against the R_s component of reflection efficiency-optimised width of Si is 177 nm. (c) Two-dimensional grid showing the fabrication tolerance of grating thickness and its optimised value is 170 nm. (d) Two-dimensional grid showing the fabrication tolerance of low index layer and its optimised value is 200 nm.

The thickness of the low index layer's fabrication tolerance would be 200 ±60 nm to maintain more than 99% of the reflection efficiency. From the above analysis, HCG in LCOSDs can be treated as a Fabry-Perot cavity, composed of the waveguide array with the HCG thicknesses as cavity length. The input plane is the HCG interface, and the exit plane is the Aluminium layer top interface serving as two mirrors. Waveguide array modes are supported by the Fabry-Perot cavity and interact and interfere with each other at the input and exit plane, giving rise to distinct characteristics of HCG. The optimisation results are summarised in the table, as shown in Table 3.2.

Wavelength of incidence	Optimal periodicity(d) at 1064 nm	Optimal width of Si(w) at 1064 nm ±tolerance	Optimal grating thickness(t_g) at 1064 nm ±tolerance	Optimal thickness of low index layer(t_l) at 1064 nm ±tolerance
1014 nm-1064 nm	610 nm	177 nm ±80 nm (more than 99% of R_S)	170 nm ±20 nm (more than 99% of R_S)	200 nm ±60 nm (more than 99% of R_S)

Table 3.2. Optimised parameters and fabrication tolerances at around 1064 nm.

3.4 CONCLUSION

I have optimised the silicon high contrast uni-periodic grating structures in the two most highly though-after wavelength ranges in near-infrared. The s-component of reflection efficiency relevant to LCoS design shows more than 99% of reflection efficiency in both designs. Based on our analysis, we confirm that the subwavelength HCG with optimised parameters will be suitable for embedding on top of conventional LCoS backplanes operating at a wavelength of 1064 nm. The duty cycle of the silicon HCG at 1064 nm is 29% which would be possible to fabricate by the industry. The next chapter will discuss the detailed approach to integrating the subwavelength HCG design on bi-periodic conventional LCoS pixels to study reflectivity enhancement.

4 CHAPTER 4:DESIGN OF HIGH REFLECTIVITY LCOSDS WITH PIXELS AND GRATING IN NEAR INFRARED AND INVESTIGATION OF STANDING WAVES IN PIXELS

Pixellated backplane consists of the bi-periodic pixel array in conventional LCoS. As the high contrast grating could be implemented as a broadband high reflective grating, integrating a HCG structure on top of pixels alleviates the diffractive optical losses associated with the pixel geometry. In this chapter, I have studied the reflectivity properties of high reflectivity LCoS by modelling HCGs on top of pixels using RCWA in near-infrared wavelength region and performed the comparison study of reflectivity of conventional LCoS. Moreover, I have numerically investigated the standing waves generated inside pixels using near-field optical analysis based on 3D-FDTD.

4.1 HIGH REFLECTIVITY LCOS WITH PIXELS AND GRATING

Frisken et al. demonstrated that the addition of silicon HCG[40] alleviates the diffractive optical losses associated with the pixel geometry of the conventional LCoS in the C-band. An increase of reflectivity of 9% was reported after introducing the HCG[40] in C-band. In the case of a conventional LCoS optical phase modulator, the diffractive optical losses are due to the pixels working in a diffraction regime. In conventional LCoS, the typical periodicity of pixels along the x-axis and y-axis are 9.2 microns and

9.18 microns, respectively. With a wavelength of incidence at 1064 nm, the periodicity is about nine times the wavelength of the incident light, i.e., the conventional LCoS operates in a diffraction regime. Figure 4.1 shows a high reflectivity LCoS for modulating the phase of an incident optical signal propagating along the z-axis as referred in[40]. The uniperiodic silicon HCG with subwavelength dimensions is placed between the pixels and the alignment layer.

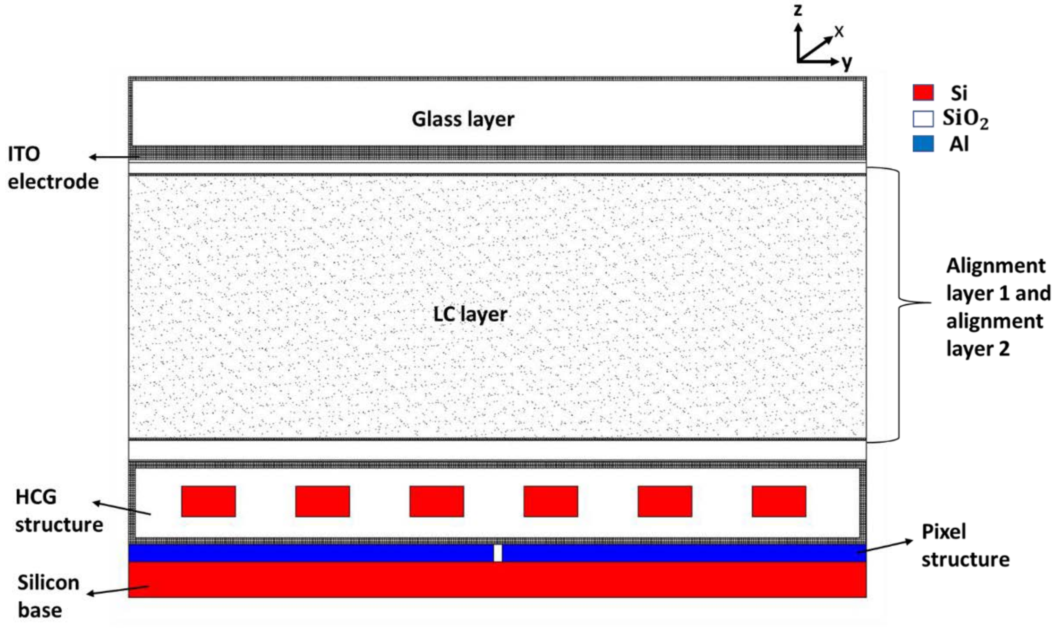

Figure 4.1. Sectional side view of the liquid crystal on silicon with pixels and grating[40].

The grating structure includes an array of silicon bars extending longitudinally along the x-axis and are partially surrounded by low refractive index silica dielectric material. With the high refractive index contrast and near subwavelength dimensions, a range of wavelengths exists where two zeroth-order diffraction modes carry the most energy. By selecting a suitable grating thickness, the transmitted modes experience destructive interference, and the grating acts as a mirror by reflecting the zeroth order mode. The near-unity reflectivity occurs as the zeroth mode can not interact with the pixel geometry.

4.2 METHODS, RESULTS AND DISCUSSION

4.2.1 Design of high reflectivity LCoS with pixels and grating in near-infrared and fabrication tolerances

Using RCWA, the pixel structure was simulated from 1014 nm to 1114 nm with periodic boundary conditions along the x and y dimensions. In the simulation, the incident plane wave propagating in the first dimension along z and silicon is considered the substrate and air is the superstrate. GD-Calc using RCWA has the advantage of mode order selection, and I have chosen the zeroth-order reflectivity corresponding to s-polarised light. The diffractive optical losses are apparent since the conventional LCoS backplane operates in a diffraction regime.

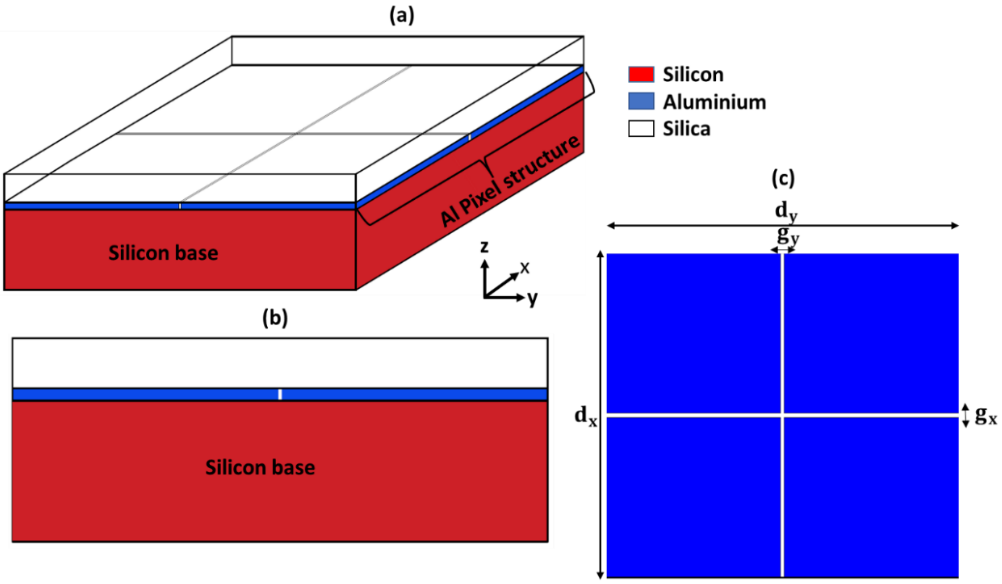

Figure 4.2 (a, b, c). Schematic diagrams of the conventional LCoS pixels. (a) Exploded perspective sectional view of the unit cell of conventional LCoS pixelated backplane with silicon as a substrate. (b) Sectional side view of the unit cell of conventional LCoS as shown in (a). (c) Schematic of the top view of the unit cell of the pixelated mirror.

Referring to Figure 4.4, the reflectivity corresponding to **s**-polarised input light simulated from 1014 nm to 1114 nm becomes 92.4% at 1064 nm. Referring to Figure 4.2 (c), the dimensions of the conventional LCoS single pixels are 9.2 microns(d_x) along x and 9.18 microns (d_y) along y, with an interpixel gap of 0.2 microns (g_x) and 0.24 microns (g_y) along x and y dimensions, respectively. Corresponding to the optimised grating parameters, the addition of silicon HCG enhances the reflection efficiency of conventional LCoS from 92.4% to 98.9% at 1064 nm. The simulated reflection efficiency plots show a broad reflection efficiency of 40 nm centred at 1064 nm. I have implemented two-dimensional grid optimisation for the LCoS structure. The critical design parameters for the grating include the periodicity of the grating, the width of silicon grating, the thickness of the grating and of the low index layer. The material silica forms the low index layer with a refractive index in[76]. The refractive index of aluminium is from[77], and the refractive index of silicon is from[78] for simulating the model. Figure 4.3 (a, b) illustrates silicon high contrast gratings deposited on top of aluminium pixels to alleviate the diffractive optical losses. The typical pixel parameters are of periodicity of 9.2 microns along the x-dimension and 9.18 microns along the y-dimensions, with a pixel gap of 200 nm and 240 nm along the x-dimension and y-dimension, respectively. The thickness of the Al pixels layer is typically 600 nm along the z-dimension.

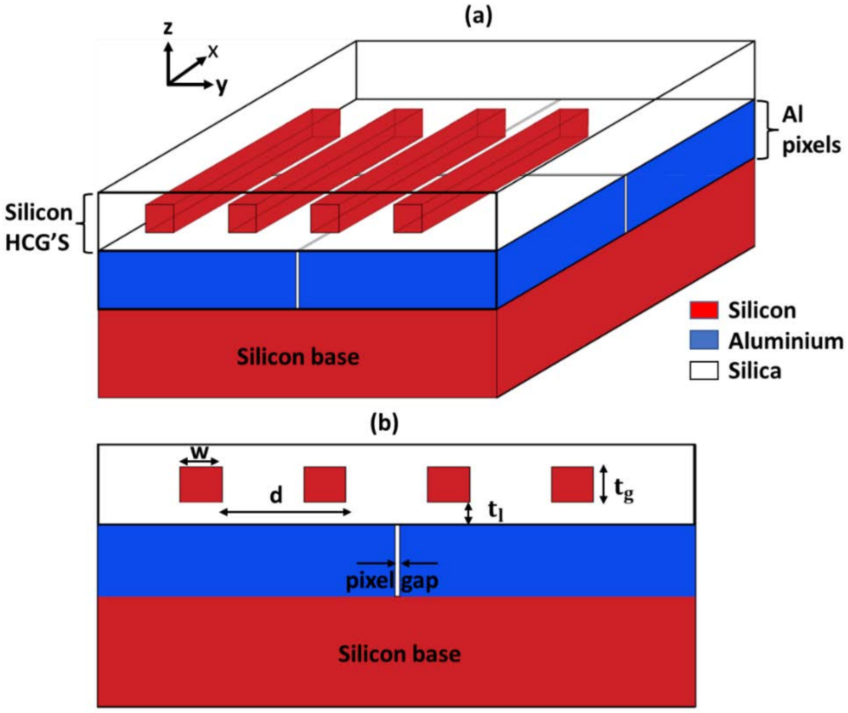

Figure 4.3 (a, b). Schematic diagram of the HCG integrated on top of LCoS pixels (a) Exploded perspective sectional view of high contrast grating embedded on top of conventional LCoS pixels. (b) Sectional side view of high reflectivity LCoS as shown in (a).

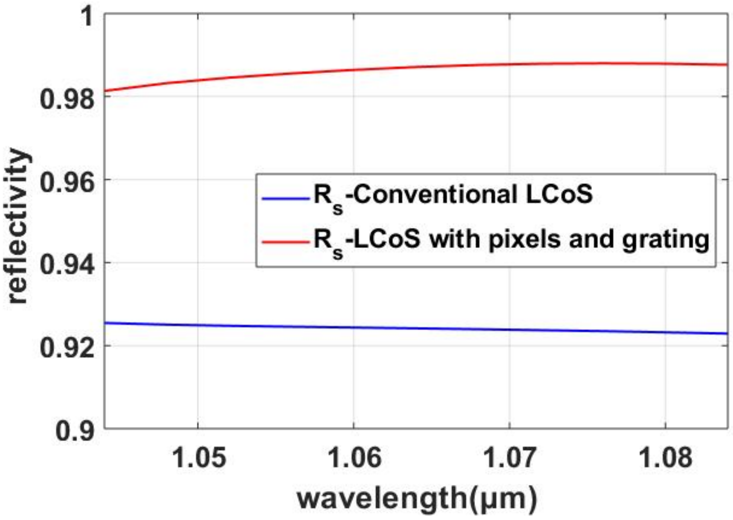

Figure 4.4. Reflectivity comparison between LCoS with grating and pixels and conventional LCoS. Increase in R_s reflectivity (red) provided by the addition of silicon high contrast grating uni-periodic structure with optimised parameters on top of conventional LCoS pixels compared to the R_s(blue) for conventional LCoS at 1064 nm.

The addition of HCG structure on top of conventional pixels with optimised parameters has increased the reflectivity from 92 % to 98.9% at a wavelength of 1064 nm. The broad reflection efficiency of 40 nm is obtained with the optimised grating parameters, as shown in Figure 4.4. Further explanation of optimisation is described in detail in the next session.

4.2.2 Two-dimensional grid optimisation and fabrication tolerance of grating parameters.

Optimal grating parameters for enhancing broad reflectivity are determined by carefully choosing the initial grating parameters. The periodicity of the grating defines the central wavelength to which the broad reflection efficiency emerges. Two-dimensional grid optimisation is performed to obtain the optimal grating parameters. The goal is to optimise the reflectivity corresponding to linearly-s-polarised input light for high reflectivity LCoSDs. We are interested in the wavelength of 1064 nm to carry out the optimisation and fabrication tolerance analysis. Referring to Figure 4.5 (a), I have started with two-dimensional grid optimisation plotted with R_s as a function of the periodicity of the grating and width of silicon. The reflectivity maximum was obtained at the wavelength of 1064 nm with a 98.9% **s** component of reflection efficiency. The optimal periodicity value is 650 nm, and the optimal width of silicon is 201 nm.

Referring to figure 4.5 (b), the s-component of reflection efficiency is plotted as a function of the wavelength and width of the silicon. The optimised parameters were fixed, including the grating thickness, the thickness of the low index layer and periodicity; the optimised width of silicon and the broad wavelength were simulated over a two-dimensional grid to plot the fabrication tolerance of the width of silicon.

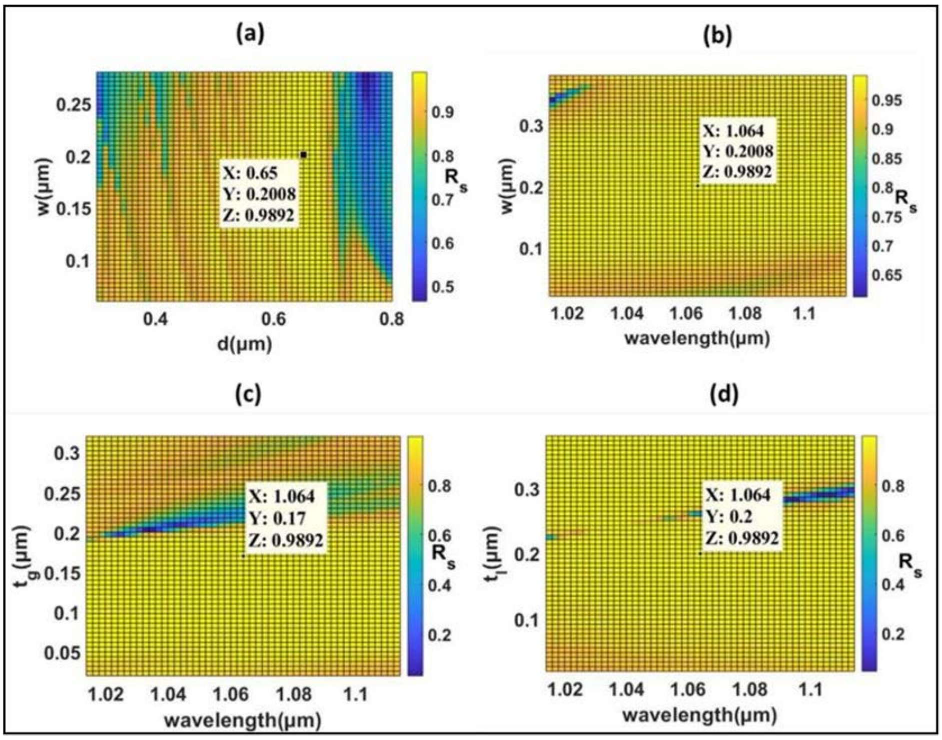

Figure 4.5 (a, b, c, d). Optimisation and fabrication tolerance of LCoS with grating and pixel at around 1064 nm. (a) The two-dimensional grid consists of the width of silicon(w) along the x-axis and period(d) along the y-axis against the Rs component of reflection efficiency with a grid size of 51*51. The optimised value of period and width of Si for a maximum reflectivity of 98.9% as 650 nm and 201 nm, respectively. (b) Two-dimensional grid showing the fabrication tolerance of the width of Si along with the x-axis and wavelength band along the y-axis against the R_s component of reflection efficiency; the optimised width of Si is 201 nm. (c) Two-dimensional grid showing the fabrication tolerance of grating thickness by plotting the R_s component of reflection efficiency as a function of wavelength and grating thickness; the optimised value of grating thickness is 170 nm. (d) Two-dimensional grid showing the fabrication tolerance of the thickness of low index layer by plotting R_s as a function of wavelength and thickness of low index layer; and its optimised value of the thickness of low index layer is 200 nm.

The width of silicon has a tolerance of 201 nm ± 70 nm to maintain the s-component of reflection efficiency of more than 98%. Referring to Figure 4.5 (c), the s-component of reflection efficiency was plotted as a function of grating thickness and wavelength. The grating thickness has a 170 nm ±24 nm tolerance to maintain more than 97% reflectivity. Figure 4.5 (d) illustrates the two-dimensional grid showing the fabrication tolerance of the thickness of the low index layer for maintaining high reflectivity. The optimal value of the low index layer's thickness was 200 nm, as shown in Figure 4.5 (d). The fabrication tolerance of the thickness of the low index layer is 200 nm ± 43 nm for maintaining a high reflectivity of more than 98%. From Figure 4.5 (a)-4.5 (d), the points on the two-dimensional grid correspond to optimised grating parameters. Excellent agreements were obtained regarding the consistency of the plots because all the points give rise to the same s-component of reflectivity. Table 4.1 summarises the optimised values' results and the grating parameters' fabrication tolerance obtained after the modelling.

Wavelength of incidence	Optimal periodicity(d) at 1064 nm	Optimal width of Si(w) at 1064 nm ±tolerance	Optimal grating thickness(t_g) at 1064 nm ±tolerance	Optimal thickness of low index layer(t_l) at 1064 nm ±tolerance
1014 nm-1114 nm	650 nm(width=201 nm)	201 nm ±70 nm (more than 98 % of R_S)	170 nm ±24 nm (more than 97% of R_S)	200 nm ±43 nm (more than 98% of R_S)

Table 4.1. Optimised parameters and fabrication tolerances of LCoS with grating and pixels at around 1064 nm.

4.3 NUMERICAL INVESTIGATION OF STANDING WAVES IN PIXELATED BACKPLANE

The enhancement of the standing waves generated at the inter-pixel gap may lead to optical losses. The standing wave generation in the visible wavelength range on the LCoS backplane was numerically and experimentally verified in[79]. Using RCWA, I have numerically investigated the standing waves generated along the interpixel gap and the layer above the pixel and below the silica layer. The near-field analysis was performed using FDTD to observe the field enhancement at the local reflectivity minima.

4.3.1 Simulation method

Conventional LCoS backplane simulated with air as superstrate, silicon as substrate and silica on top of bi-periodic pixels as shown in Figure 4.6 (b). I have set periodic boundary conditions along the x and y dimensions to simulate the bi-periodic pixels. To solve all diffraction orders in reflection, the light is made to incident from air as superstrate to individual layers, including silica, pixel, and the silicon substrate. We are interested in the **s**-component of reflection efficiency since the WSS and WaveShaper employing LCoSDs as switching elements work efficiently in s-polarised input light. The structure was simulated over 1 micron to 2 microns, and I found the local minima and maxima in the reflectivity plot, as shown in Figure 4.6 (a). The zeroth-order diffracted mode carries the most energy, and the pixels work in a diffraction regime. Since the periodicity of the pixels are multiples of the wavelength of incoming light, total energy splits into multiples of orders resulting in diffractive optical losses.

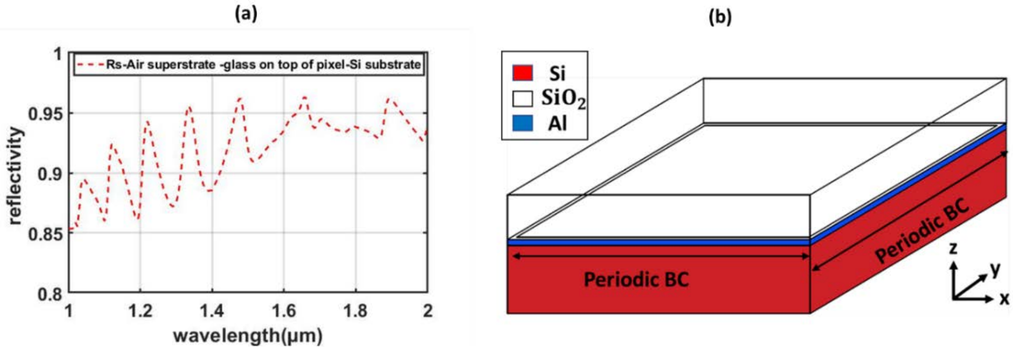

Figure 4.6 (a, b). Broad reflectivity of conventional LCoS simulated to observe local minima and maxima. (a) Reflection efficiency (R_S) of pixelated structure simulated over 1 micron to 2 microns. (b) Schematic diagram of the pixelated design with 9.2 microns periodicity along x and 9.18 microns periodicity along y with interpixel gap 200 nm and 240 nm along x and y, respectively.

The local minima and local maxima could be explained with the help of near-field optical analysis. In the case of reflectivity from 1000 nm to 1200 nm, the reflectivity maxima occur at 1054 nm, and reflectivity minima occur at 1069 nm, as shown in Figure 4.6(a).

4.4 RESULTS AND DISCUSSION

4.4.1 Near optical field analysis using FDTD

Here I have performed 3D-FDTD to simulate the bi-periodic pixel structure. The FDTD simulation is illustrated in Figure 4.7. I have set periodic boundary conditions along the x-dimension and y-dimension. A perfectly matched layer (PML) boundary condition along the direction of plane wave propagation was placed along z-dimensions to minimize the reflections along the z-direction. A plane wave with normal incidence having TE polarisation is made to incident on the structure. The field profile monitor was placed along the YZ plane's cross-section and normal to the XZ plane, providing the electric field distribution (average time value) as a function of position and frequency. The field monitor uses continuous wave normalisation to obtain the field along the cross-section.

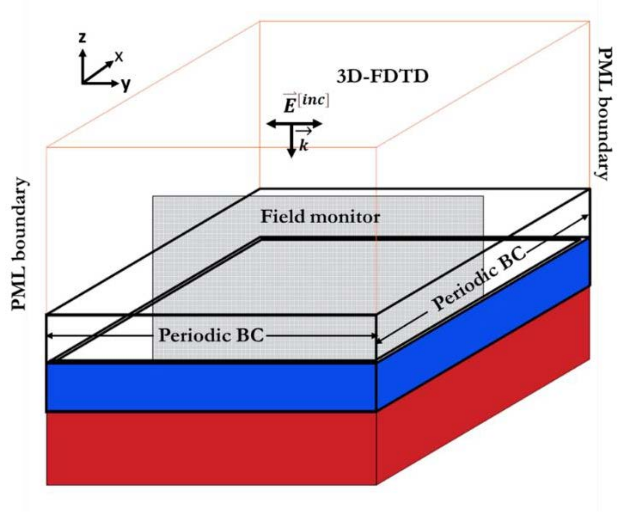

Figure 4.7. Schematic diagram of the 3D-FDTD (rectangular pink box extending vertically) simulation. Periodic boundary conditions are set along the x-dimension and the y-dimension. PMLs are placed along the z-direction. The periodicity of the pixel along the x and y dimensions are 9.18 µm and 9.2 µm, respectively. Interpixel gaps along the x and y dimensions are 0.2 µm and 0.24 µm, respectively. A transverse electric polarised plane wave is made to incident on the structure along the z-direction from the top. A two-dimensional frequency domain field monitor is placed normal to the XZ plane to record the electric field distribution along the cross-section.

Figures 4.8 (a) and 4.8 (d) show the near field for the reflectivity for the ideal pixel shape at a shorter wavelength of 1054 nm and a longer wavelength of 1069 nm, respectively. As one can see, the white dashed line is the pixel shape and above it is the silica layer on top of the pixel. Figure 4.8 (a,b,c,d) shows that the standing waves getting enhanced between the silica and the pixel layers. One can see the less pronounced standing waves for a wavelength of 1054 nm, where a local maximum has been shown. Meanwhile, one can see a similar pattern with pronounced standing waves for a higher wavelength of 1069 nm, where a local minimum has shown up. One can observe from 1054 nm to 1069 nm; the standing wave pattern gets enhanced inside the pixel gap region, above the pixel gap, and below the silica layer. The electric field enhancement from 1054 nm to 1069 nm is summarised in Table 4.2.

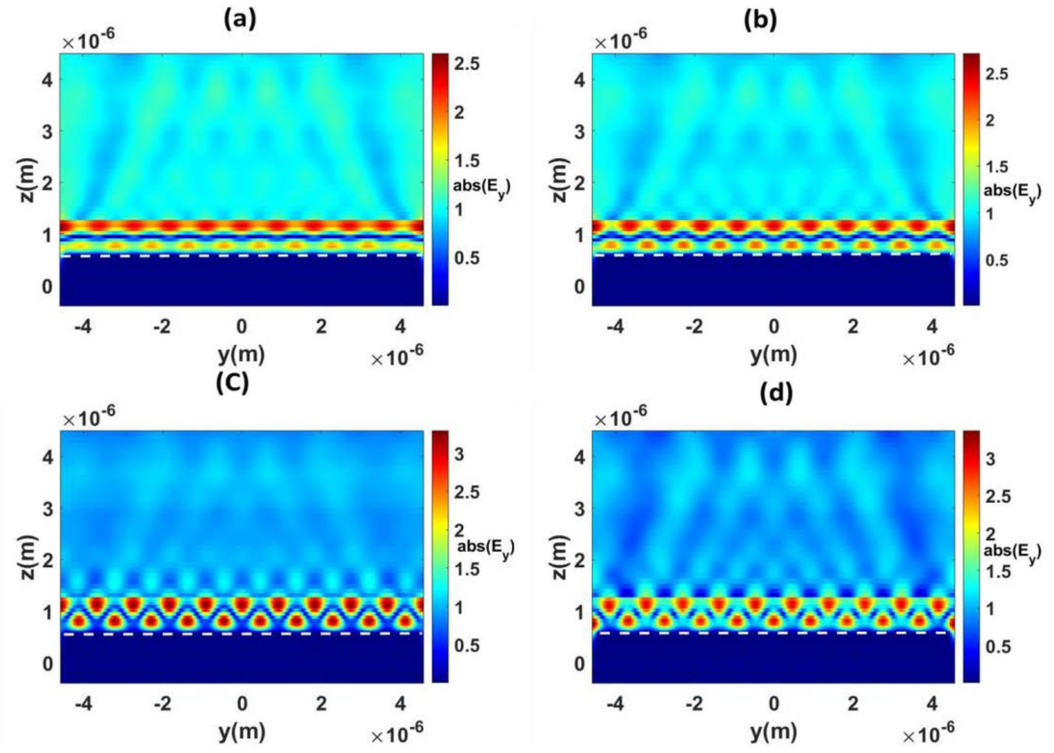

Figure 4.8 (a, b, c, d). Near field optical analysis of conventional LCoS pixels. (a) $|\mathbf{E_y}|$ corresponding to the local maximum from the reflectivity plot, as shown in Figure 4.5(a) at a wavelength of 1054 nm (b) $|\mathbf{E_y}|$ corresponding to the wavelength of 1058 nm (c) $|\mathbf{E_y}|$ corresponding to the wavelength of 1063 nm (d) $|\mathbf{E_y}|$ Corresponding to the local minimum from the reflectivity plot as shown in Figure 4.5(a) at a wavelength of 1069 nm showing a pronounced standing wave pattern above the pixel layer and between the interpixel gap.

Wavelength(nm)	Maximum electric field($\lvert \mathbf{E_y} \rvert$)Volt/meter
1054 nm	2.55 Volt/meter
1058 nm	2.64 Volt/meter
1063 nm	3.27 Volt/meter
1069 nm	3.34 Volt/meter

Table 4.2. The table illustrates the maximum electric field $\lvert \mathbf{E_y} \rvert$ of the standing waves generated inside the pixel gap region, above the pixel gap, and below the silica layer, as shown in Figure 4.8.

4.5 CONCLUSION

I have performed a range of numerical parameter scans to obtain the optimal grating parameters corresponding to the maximum s-component of reflection efficiency of high reflectivity LCoSD with pixels and grating at the near-infrared wavelength of 1064 nm. It is important to note that this wavelength is of high interest since WaveShapers with high reflectivity LCoS as a switching element are being developed for use with high-power pulsed LASERs at around 1064nm. The enhancement of the s-component of reflectivity by adding silicon HCG alleviates the diffractive optical losses associated with the conventional LCoS device. Adding HCGs would minimize the cavity size for the device to perform as a broadband high-reflectivity LCoS. The optimum thickness of the grating is 170 nm. Applying HCG on top of conventional LCoS pixels prevents pixel structure's coating with multilayer dielectric coating, further reducing the inherent voltage drop over many layers for overcoating to suppress the diffractive optical losses. However, even though the coating with multiple layers of Bragg mirrors is less costly, the industry is focusing more on reducing the device's size and mitigating the thermally induced stress for a better product. With cautiously chosen grating parameters using the two-dimensional grid optimisation, I have obtained a destructive interference at the boundary starting the low index layer below the grating thickness $\mathbf{t_g}$ along z-dimension, so the energy is prevented from coupling to the pixel structure and high reflection is achieved. I have obtained the optimal duty cycle of the grating, defined as the fraction of the high index material to be 31%, which is within the fabrication limits of optical lithographic standards. I have qualitatively shown the critical grating parameters' fabrication tolerance for obtaining a high reflectivity of more than 98% over a broad wavelength range. The layers above the pixel region and the dead space or interpixel gap would create standing waves, as mentioned in section 4.4.1. I have carried out numerical investigation of the standing wave phenomenon in the near-infrared region and shown the enhancement of the standing waves at the interpixel gap and the layers above the pixel structure with near-field optical analysis. The high reflectivity LCoSDs performance is essential to extend to a visible wavelength range for beam shaping, adaptive optics, microscopy applications and optical tweezers. Silicon HCGs become highly absorbing in visible wavelengths, and a better candidate must be substituted instead of silicon in the high reflectivity LCoS design. In the next chapter, I will propose silicon nitride high contrast high reflectivity LCoS as they possess high reflectivity and less absorption in the visible wavelength range of operation.

5

CHAPTER 5: DESIGN OF LCOSDS IN VISIBLE WAVELENGTHS

This chapter shows a detailed study of Si_3N_4 gratings as a broadband reflector in the visible wavelength of operation, which is suitable for enhancing the performance of high-reflectivity LCoS spatial light modulators. In this chapter, I proposed Si_3N_4 LCoS without pixels in two critical visible wavelengths of operation and briefly discussed two essential optimisation algorithms, including genetic and two-dimensional grid optimisation.

5.1 INTRODUCTION TO SILICON NITRIDE HCG

Here I am optimising the LCoS without pixels and with Si_3N_4 grating and the LCoS with pixels and Si_3N_4 grating in the visible wavelength range. Silicon nitride HCGs are promising candidates in the visible wavelength range for high reflectivity LCoSDs as they possess less absorption and provide more reflection efficiency. Compared to semiconductor HCGs, the wavelength flexibility of the Si_3N_4 platform is very promising in the visible wavelength range. Prof.Thomas F Krauss et al. designed and fabricated[80] tunable optical filters based on Si_3N_4 HCGs in the visible wavelength range.

Here, I am incorporating silicon-rich silicon nitride HCGs as a broadband reflector in LCoS as they possess near unity reflection in the visible wavelength range. Typically, HCG is a subwavelength grating surrounded by low-index materials. Silicon nitride gratings have the properties shown by the HCGs[42-43, 72-73, 81], such as broadband reflectivity and phase control.

5.2 DESIGN OF SILICON NITRIDE HCG LCOS IN THE VISIBLE WAVELENGTHS

The reflection of the silicon nitride gratings are simulated using rigorous coupled-wave analysis by GD-Calc[64]. The proposed LCoS with silicon nitride grating structure is schematically shown in Figure 5.1(a) and can be described as a one-dimensional periodic array of Si_3N_4 rectangular bars surrounded by silica.

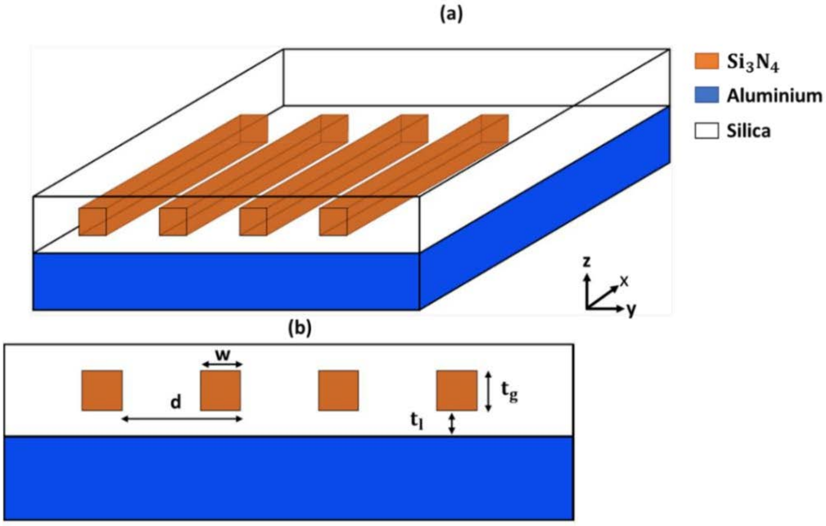

Figure 5.1 (a, b). Schematic diagram of Si_3N_4 grating LCoS without pixels (a) Exploded perspective sectional view of the LCoS device without pixels and with Si_3N_4 grating and aluminium layer. (b) Sectional side view of an LCoS device as shown in (a).

RCWA splits the LCoS with grating without pixels into homogeneous regions in the normal z-direction and implements periodic boundary conditions to obtain a transfer matrix for individual layers in the frequency domain in Bloch modes. The incident optical signal from superstrate to substrate with a given k-vector can then propagate from one layer to another to solve all individual diffraction orders in reflection. In the normal incidence case, a plane wave is incident from the superstrate as air, normal to the grating plane with the polarisation of the electric field orthogonal to the gratings.

5.3 OPTIMISATION METHODS

5.3.1 Genetic algorithm to set initial grating parameters for optimisation in the visible wavelength

Genetic optimisation[82-84] is an example of multi-parameter optimisation. In the initial phase, candidate solutions are generated and then tested against the objective function. The first generation evolves through selection, crossovers, and mutations into subsequent generations. From one generation to the next, selection refers to retaining the best-performing parent. The crossover process selects similarities between the different parent variables and maintains those for the next generation of children variables. The final one is the mutation, which takes parents and mutates certain variables to take on random values and create a child based on the mutation. Genetic algorithm evaluates all initial populations and determines each population's fitness function. Then it will select a few reasonable solutions for the parents to continue to the next generation and use those good solutions to create the subsequent generations. Genetic algorithms generate those new points through selection, crossover, and mutation and then evaluate the new population. The iteration repeats the process of developing new generations until the algorithm converges. As soon as a certain number of generations has been reached, the genetic algorithm converges. Alternatively, the best objective function or fitness function value may converge when it no longer changes by a minimal amount. More details of the genetic algorithm optimisation are outlined in Appendix B.

In my proposed design, the critical design parameters include the thickness of silicon nitride grating, the thickness of the low-index silica layer, the width of silicon nitride grating, and the grating periodicity. I'm interested in optimising the **s**-component of reflection efficiency $\mathbf{R_S}$. To set the algorithm, I need to set global and local variables. Global variables are the permittivity values of silica[76], silicon nitride[85], aluminium[77] and air, and local variables are the critical design parameters. In a genetic algorithm, a population of candidate solutions to an optimisation problem is evolved towards a better solution. To start with, an initial generation of candidate solutions that are tested against the objective function. In each generation, the fitness value of every individual in the population is evaluated; in our case fitness value is 1-R_S. The algorithm converges when the best fitness function value approaches the function tolerance, which is $10^{(-6)}$. When the number of variables involved in the optimisation is more than five, the population size is 200; when the number of variables is less than or equals five, the population size is 50. The maximum number of generations before the iteration halts equals 100* variables involved in the optimisation problem. After performing the genetic algorithm optimisation, the optimal parameters generated correspond to R_s maximum. I will perform a two-dimensional grid optimisation to obtain the fabrication tolerance analysis of the critical design parameters.

5.4 RESULTS AND DISCUSSION

5.4.1 Four parameter optimisation of R_s using genetic algorithm at 800 nm

The LCoS design without pixels and grating refers to Figure 5.1(a,b), optimised to obtain high reflectivity at 800 nm. I have performed genetic algorithm optimisation with RCWA using GD-Calc to get initial grating parameters for optimising the design. Destructive interference of the waveguide array modes strongly coupled to the zeroth order diffraction grating can be obtained at the plane below the silicon nitride grating thickness and above the silica layer with cautiously chosen optimised parameters. This prevents the energy from being coupled into the transmission channel of the aluminium layer, which results in a high reflectivity, as shown in Figure 5.2 (b). The local variables that are selected over here are the periodicity of the grating (**d**), the width of silicon nitride(**w**), the thickness of the grating($\mathbf{t_g}$) and the thickness of the low index layer($\mathbf{t_l}$). Then the number of design variables equals four. The maximum number of generations before the iteration halts equals 400. Figure 5.2 (a) shows the generation vs fitness value plot. The optimisation terminated once the average change in the fitness value less than the function tolerances, as shown in Figure 5.2 (a). We have obtained the optimal grating parameters to be as grating thickness ($\mathbf{t_g}$) equals 294 nm, the thickness of low index layer ($\mathbf{t_l}$) equals 300 nm, grating period (**d**) equals 539 nm, and the width of silicon nitride equals(**w**) 207 nm.

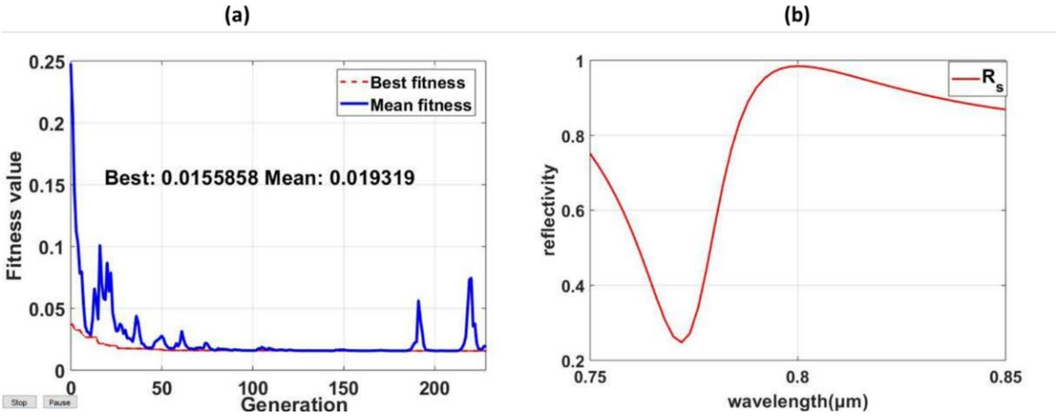

Figure 5.2 (a, b). Genetic algorithm optimisation and broad reflectivity correspond to optimal parameters. (a) Genetic algorithm plot showing the number of generations Vs Fitness value. The algorithm converges when the average change in the best fitness function value is less than or equal to $10^{\wedge(-6)}$. (b) R_s component of reflectivity simulated over the wavelength range 750 nm to 850 nm with central wavelength 800 nm with the optimised parameters from the genetic algorithm.

Figure 5.2 (b) shows the simulated reflection of silicon nitride grating corresponding to the optimised gratin parameters from genetic algorithm optimisation. The simulated R_S reflectivity shows 98.44% at 800 nm. The reflectivity is more than 80% from 785 nm to 815 nm, with a maximum of 98.44% at 800 nm, as shown in Figure 5.2 (b).

5.4.2 Fabrication tolerance analysis of silicon nitride grating without pixels at 800 nm

Two-dimensional grid optimisation was carried out to determine the optimal periodicity and duty cycle with the initial grating parameters obtained from genetic algorithm optimisation referring to Figure 5.2 (a, b). Excellent agreement was obtained with genetic optimisation simulation and two-dimensional grid optimisation at the wavelength of 800 nm. Referring to Figures 5.3 (a) and 5.2(a), the optimal grating parameters were found to be the same, validating the simulation's accuracy. The fabrication tolerance of the width of silicon nitride grating was 207 nm ± 70 nm to maintain the reflectivity of more than 98% at 800 nm, as shown in Figure 5.3(b). Referring to Figure 5.3(c), the fabrication tolerance of the thickness of grating is found to be 294 nm ±30 nm to maintain the reflectivity of more than 98% at 800 nm, as shown in Figure 5.3(c). From Figure 5.3 (d), the optimised thickness of the low index layer is 300 nm; fabrication tolerance is found to be 300 nm ± 30 nm to maintain high reflectivity of more than 98%.

It is possible to broaden the high reflectivity range by changing the thickness of the low index layer by keeping all the other parameters the same. Near unity reflectivity can be achieved at the thickness of the low index layer of more than 600 nm, making the system bulkier. The 40 nm broad high reflectivity of more than 92% with 100% reflectivity achieved at 800 nm could increase the low index layer thickness. All the points, as shown in Figure 5.3 (a) to Figure 5.3 (d), simulate the same reflectivity corresponding to optimal grating parameters, validating the consistency of the simulation. The optimisation and fabrication tolerances at around 800 nm are summarised in Table 5.1.

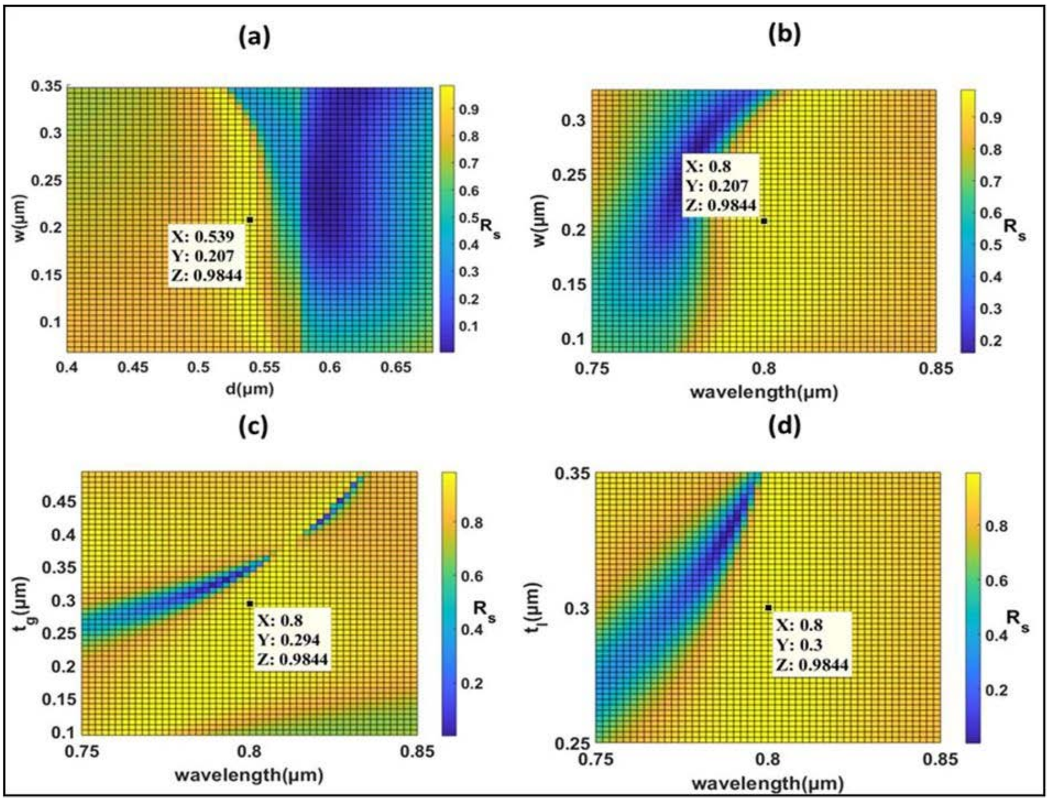

Figure 5.3 (a, b). Optimisation and fabrication tolerance analysis of Si_3N_4 grating LCoS without pixels at around 800 nm (a) Simulated two-dimensional grid with the initial grating parameters from genetic optimisation algorithm. The grid is formed by calculating the s-component of reflection efficiency R_s as a function of silicon nitride's grating period and width. The periodicity of the grating varies from 678 nm to 400 nm, and the width of silicon varies from 67 nm to 347 nm over the grid consisting of 51*51 points. The optimal point is marked as a black dot with an R_s maximum corresponding to a periodicity of 539 nm and a duty cycle of 38%. (b) Simulated R_s as a function of the width of grating and wavelength, and the black dot on the grid shows the optimal point corresponding to R_s maximum of 98.44% with optimal width of the grating as 207 nm at 800 nm wavelength. (c) Simulated R_s as a grating thickness and wavelength function, and the black dot shows the optimal point where the R_s is 98.44%. The optimal grating thickness corresponding to the maximum reflectivity is 294 nm at 800 nm. (d) Simulated R_s as a function of the thickness of the low index layer and wavelength; the optimal reflectivity obtained is 98.44%, and the corresponding thickness of the low index layer is 300 nm.

Wavelength of incidence	Optimal periodicity(d) at 800 nm	Optimal width of Si(w) at 800 nm ±tolerance	Optimal grating thickness(t_g) at 800 nm ±tolerance	Optimal thickness of low index layer(t_l) at 800 nm ±tolerance
750 nm-850 nm	539 nm(38% Duty Cycle)	207 nm ±70 nm (more than 98% of R_S)	294 nm ±30 nm (more than 98% of R_S)	300 nm ±30 nm (more than 98% of R_S)

Table 5.1. Summary of optimisation at around 800 nm. The table summarises the optimisation and fabrication tolerance of the LCoS backplane without pixels with grating.

5.4.3 Four parameter optimisation of R_s using genetic algorithm at 532 nm

Genetic algorithm optimisation was carried out on the silicon nitride grating structure, as shown in Figure 5.1(a, b), to determine initial grating parameters for optimising the structure at the wavelength of 532 nm. I have defined the upper and lower bound values within a range of 550 nm to 100 nm for the thickness of low index layer $\mathbf{t_l}$, 50 nm to 650 nm for grating thickness $\mathbf{t_g}$, 300 nm to 650 nm for grating periodicity **d**, 60 nm to 280 nm for the width of Si_3N_4. The algorithm computes 50 combinations of randomly chosen local variables for each generation and obtains 50 score values. In our case, 1-R_s is the score value, and the local variables are the grating parameters. Then it takes the minimum out of 50 score values and the corresponding set of local variables for the next generation. The process continues, and the optimisation terminates once the fitness value average becomes less than the function tolerance. I have obtained optimal grating parameters, including the thickness of the low index layer as 550 nm, the thickness of grating as 115 nm, the periodicity of the grating as 347 nm and the width of silicon nitride grating as 152 nm. The optimal grating parameters provide a unity reflectivity at 532 nm wavelength, as shown in Figure 5.4(b).

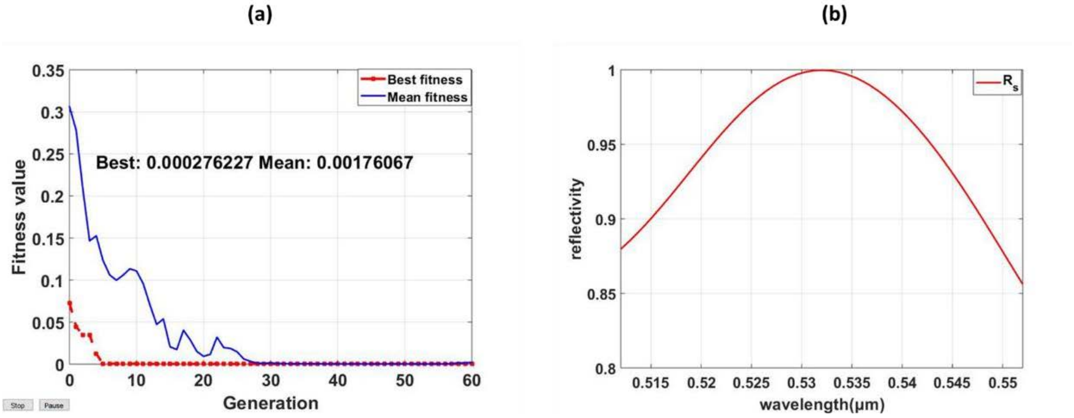

Figure 5.4 (a, b). Genetic algorithm optimisation and broad reflectivity corresponding to optimal parameters (a) Genetic algorithm converge at the 60th generation. The optimisation terminates once the average change in the best fitness value approaches 10^$^{(-6)}$. (b) Simulated broad reflectivity spectrum with a centre wavelength of 532 nm. The high reflectivity of 98.44% was obtained at 800 nm. At 532 nm, we get 99.9% near unity reflectivity corresponding to s-polarised input light.

5.4.4 Fabrication tolerance analysis of silicon nitride grating LCoS without pixels at around 532 nm

Two-dimensional grid optimisation was carried out to determine the optimal periodicity and duty cycle with the initial grating parameters obtained from genetic algorithm optimisation referring to Figure 5.4(a, b). Excellent agreement was obtained with both the genetic optimisation algorithm and two-dimensional grid optimisation at the wavelength of 532 nm. Referring to Figures 5.4 (a) and 5.2(a), the optimal grating parameters were found to be the same, validating the simulation's accuracy. The fabrication tolerance of the width of silicon nitride grating is 150 nm ± 50 nm to maintain the reflectivity of more than 99% at 532 nm, as shown in Figure 5.5(b). Referring to Figure 5.5(c), the fabrication tolerance of grating thickness is 114 nm ± 24 nm to maintain the reflectivity of more than 98% at 532 nm, as shown in Figure 5.5(c). From figure 5.5(d), the optimised thickness of the low index layer is 550 nm;

fabrication tolerance is 550 nm ± 50 nm to maintain high reflectivity of more than 99%.

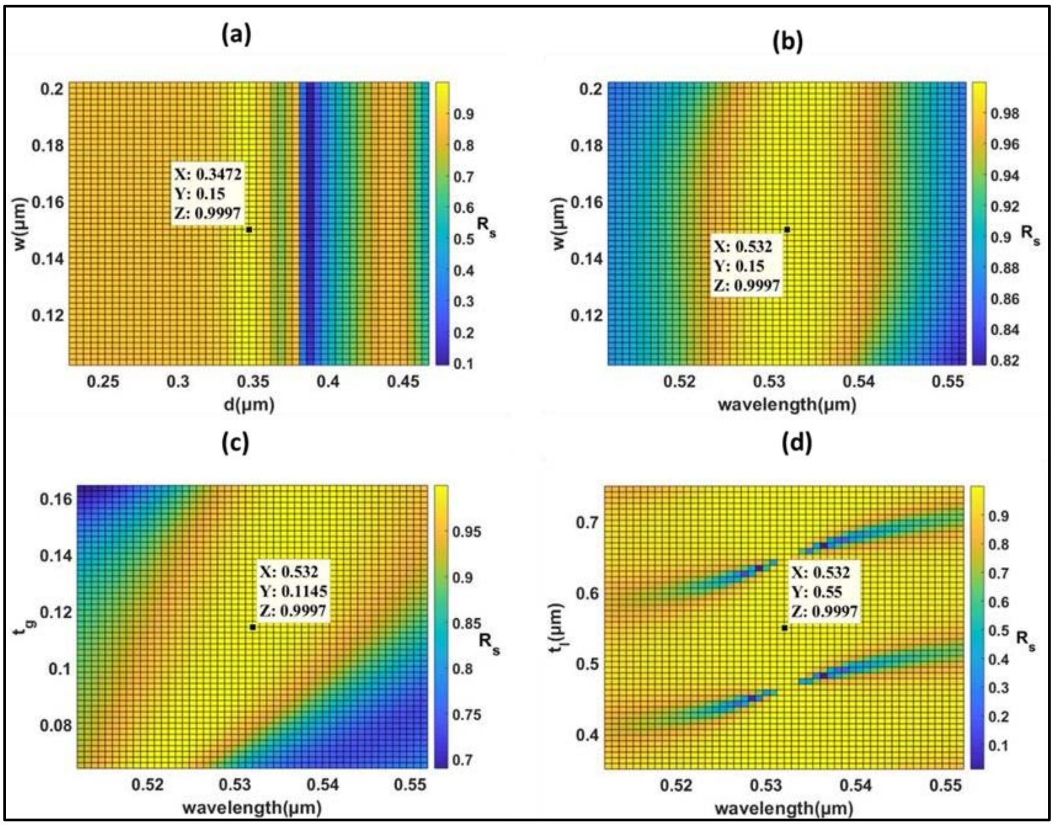

Figure 5.5 (a, b,c,d). Optimisation and fabrication tolerance analysis of Si_3N_4 grating LCoS without pixels at around 532 nm (a) Simulated two-dimensional grid with the initial grating parameters from genetic optimisation algorithm. The grid is formed by calculating the s-component of reflectivity R_S as a function of silicon nitride's grating period and width. The periodicity of the grating varies from 467 nm to 227 nm, and the width of silicon varies from 102 nm to 202 nm over the grid consisting of 51*51 points. The optimal point is marked as a black dot with R_s maximum corresponding to a periodicity of 347 nm and a duty cycle of 43%. (b) Simulated R_s as a function of the width of grating and wavelength, and the black dot on the grid shows the optimal point corresponding to R_s maximum of 99.7 % with optimal width of the grating as 150 nm at 532 nm wavelength. (c) Simulated R_s as a function of grating thickness and wavelength, and the black dot shows the optimal point where the R_s is 99.7 %. The optimal grating thickness corresponding to the maximum reflectivity is 114 nm at 532 nm. (d) Simulated R_s as a function of the thickness of the low index layer and wavelength; the optimal reflectivity maximum obtained is 99.7 %, and the corresponding thickness of the low index layer is 550 nm.

It is possible to broaden the high reflectivity range by changing the thickness of the low index layer by keeping all the other parameters the same. 100 % reflectivity can be achieved at the thickness of the low index layer of more than 600 nm, making the system bulkier. All the points, as shown in Figure 5.5(a) to Figure 5.5(d), simulate the same reflectivity maxima corresponding to optimal grating parameters, validating the consistency of the simulation.

As one can observe, the high Q resonance occurs at a low index layer thickness of 638 nm and 454 nm at around 528 nm, as shown in Figure 5.5(d). This resonance can be interpreted as the GMR effect[62], as the periodicity of the silicon nitride grating is of subwavelength dimensions, and the effective refractive index of the grating layer is $\sqrt{2.055^2 + 1.46^2}$ equal to 2.52, which is greater than the refractive index of the waveguide layer made of silica.

Wavelength of incidence	Optimal periodicity(d) at 532 nm	Optimal width of Si(w) at 532 nm ±tolerance	Optimal grating thickness(t_g) at 532 nm ±tolerance	Optimal thickness of low index layer(t_l) at 532 nm ±tolerance
512 nm-552 nm	347 nm(43.2% Duty Cycle)	150 nm ±50 nm (more than 99.5% of R_S)	115 nm ±24 nm (more than 98% of R_S)	550 nm ±50 nm (more than 99% of R_S)

Table 5.2. Summary of optimisation at around 532 nm. The table summarises the optimisation and fabrication tolerance of the LCoS backplane without pixels and with grating.

5.4.5 Design of silicon nitride grating on top of conventional LCoS pixels.

We have seen the performance of silicon nitride grating in the visible wavelength range from 750 nm to 850 nm as a broadband high reflectivity mirror. We can improve the high reflectivity and the range of high reflectivity by adequately choosing the thickness of the low index layer. Adding silicon nitride subwavelength grating on top of pixels could alleviate the diffractive optical losses associated with conventional LCoS pixels.

In[40], silicon HCG was implemented to improve the diffraction efficiency of conventional LCoS. Due to high index contrast and subwavelength dimensions, silicon HCG is a good candidate in the near-infrared C-Band and 1064 nm range.

Meanwhile, silicon HCG becomes less attractive in the visible range since silicon undergoes high absorption and can not act as a high-reflectivity mirror. Silicon nitride HCGs have the wavelength flexibility to perform as a promising candidate in the LCoS platform as a spatial light modulator in WSS. In[79], silicon nitride is implemented as a highly reflective coating layer on top of conventional LCoS. Here I propose a structure showing excellent improvement in the reflectivity of conventional LCoS backplanes by integrating silicon nitride subwavelength grating on top of conventional LCoS pixels.

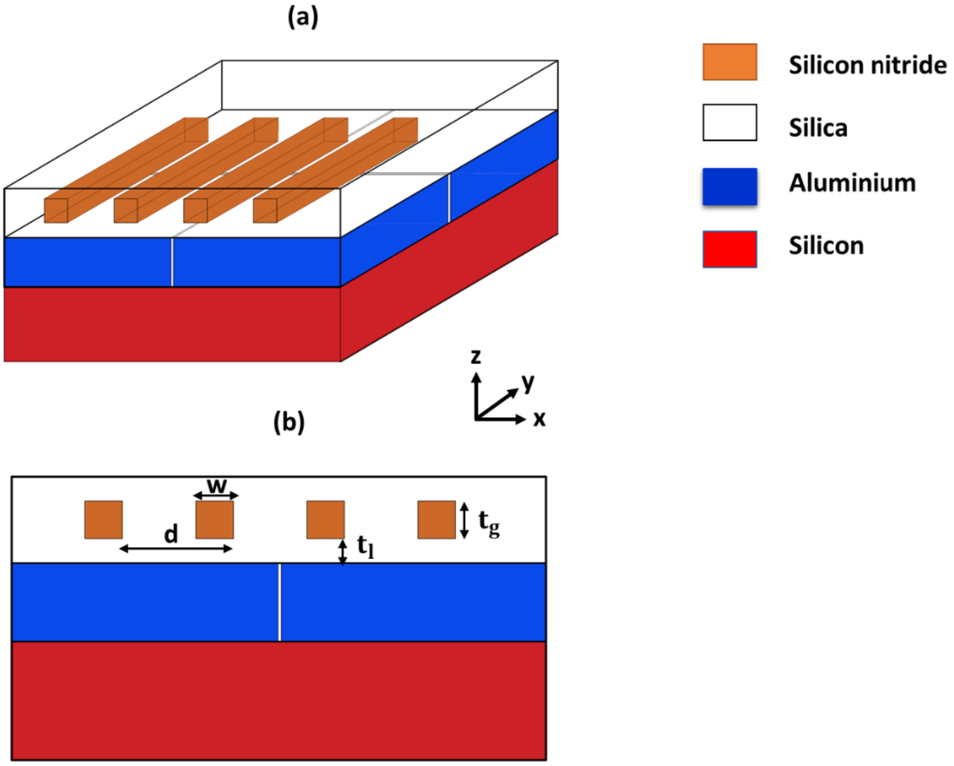

Figure 5.6 (a, b). Schematic diagram of LCoS with Si_3N_4 grating and pixels (a) Exploded perspective sectional view of the LCoS device with pixels and Si_3N_4 grating. (b) Sectional side view of the LCoS device as shown in (a).

Important design parameters for the proposed structure are the periodicity of the grating(**d**), the width of Si_3N_4(**w**), the thickness of the low index silica layer below grating($\mathbf{t_l}$) and grating thickness($\mathbf{t_g}$). Figure 5.6 (a, b); shows the schematic of the simulated Si_3N_4 subwavelength grating on top of the conventional LCoS pixels. We have considered silicon as the substrate and air as the superstrate. The boundary conditions are set to periodic in both x and y dimensions. The typical inter-pixel gap along the x and y dimensions is set to 200 nm and 240 nm, respectively. The optimal grating parameters are obtained through two-dimensional grid optimisation with initial grating parameters obtained from genetic algorithm optimisation, as shown in section 5.1. Linear, logarithmic convergence study was carried out on the simulation to test the accuracy of the simulation, and the structure converges at the maximum number of diffraction orders at m_max=15, as shown in Figure 5.7(a).

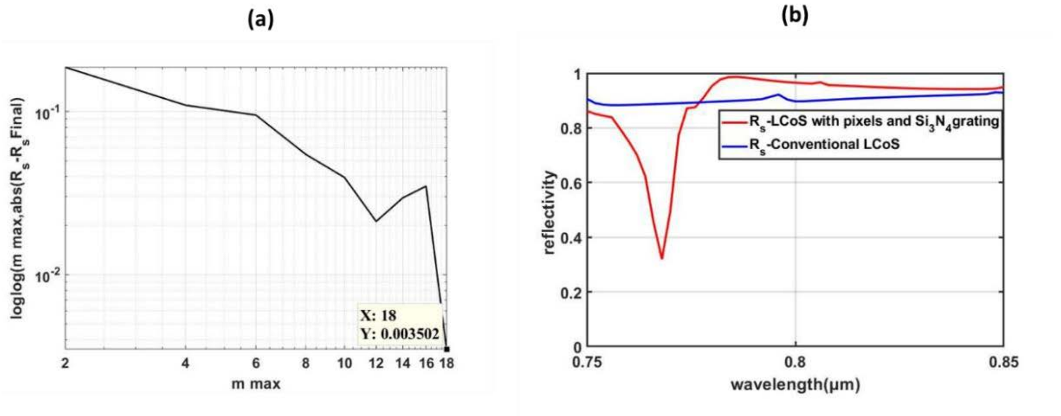

Figure 5.7 (a, b). Convergence plot and broad reflectivity comparison at around 800 nm (a)Linear, logarithmic convergence shows that the simulation converges to the least error of 3*10^$^{(-3)}$ at the maximum number of orders=18. (b) The increase of R_s reflectivity provided by the inclusion of the high contrast grating with optimised parameters (red) compared to conventional LCOS (blue).

With carefully chosen grating parameters via genetic algorithm optimisation followed by two-dimensional grid optimisation, destructive interference can occur at the exit plane just before the pixelated geometry along z-dimension($\mathbf{z=t_l}$), and the energy is blocked from coupling to the aluminium pixels. High reflection is achieved, as shown in Figure 5.7 (b).

5.4.6 Optimisation of Si_3N_4 subwavelength grating LCoS using two-dimensional grid optimisation at 800 nm

I have implemented the method of two-dimensional grid optimisation to find the optimal grating parameters of the proposed design. Figure 5.8 (a) illustrates the two-dimensional grid simulated with R_s as a function of the width of silicon nitride and the periodicity of silicon nitride grating. The grid consists of 400 elements with periodicity(d) values ranging from 400 nm to 800 nm and the width of silicon nitride ranging from 60 nm to 280 nm. I have plotted the R_s in the log scale and obtained the optimal periodicity of 526 nm and duty cycle of 33%. Figure 5.8 (b) illustrates the reflection efficiency of the LCoS simulated over a two-dimensional grid consisting of R_s as a function of the thickness of the low index layer and grating thickness. The thickness of the low index layer value ranges from 50 nm to 350 nm, and the grating thickness ranges from 40 nm to 400 nm along the two-dimensional grid. The optimal thickness of the low index layer is 223 nm, and the optimal grating thickness is 361 nm, as illustrated in Figure 5.8 (b).

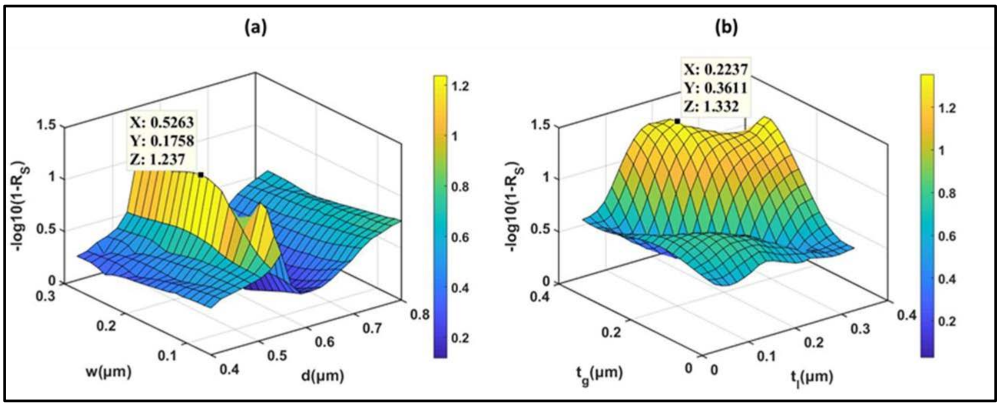

Figure 5.8 (a, b). Two-dimensional grid optimisation in log scale. (a) Illustrates the simulated two-dimensional grid plot to show the optimised width of silicon (w) and periodicity(d) corresponding to a maximum reflectivity. Optimised period equals 526 nm, and the width of silicon equals 176 nm resulting in a 33% duty cycle. (b) Illustrates the simulated two-dimensional grid plot in log scale to show the optimised thickness of the low index layer and grating thickness. The optimal thickness of grating equals 361 nm, and the optimal thickness of the low index layer equals 223 nm.

Wavelength of incidence	Optimal periodicity(d) at 800 nm	Optimal width of Si(w) at 800 nm	Optimal grating thickness(t_g) at 800 nm	Optimal thickness of low index layer(t_l) at 800 nm
750 nm-850 nm	526 nm (33% Duty Cycle)	175 nm (more than 96% of R_S)	361 nm (more than 96% of R_S)	223 nm (more than 96% of R_S)

Table 5.3. Summary of optimised parameters of the LCoS with pixels and Si_3N_4 grating.

5.5 CONCLUSION

I have simulated the silicon nitride high contrast subwavelength gratings in two significant visible wavelength ranges. For both 800 nm and 532 nm wavelengths, the HCG structure shows excellent broadband reflectivity with near-unity reflectivity at the centre wavelength of operation. I have successfully modelled the subwavelength silicon nitride HCGs on top of conventional LCoS pixels using genetic algorithm optimisation followed by two-dimensional grid optimisation. I have optimised high reflectivity LCoSDs at around 1064 nm using silicon HCGs (Demonstrated in chapter 4), as well as optimised high reflectivity LCoSDs at around 532 nm using silicon nitride HCGs, which can be highly useful for WaveShapers implemented for pulsed high-power LASERs operating at these wavelengths.

Adding a high-contrast silicon nitride grating with a rectangular rod cross-section on top of a bi-periodic Aluminium pixel structure of conventional LCoS increases the R_s component of reflectivity from 89% to over 96.5% at the wavelength of 800 nm. LCoS using silicon nitride gratings opens the possibility of optical beam shaping, and beam steering in the visible wavelength range has applications in the biosensing platform. They have an excellent ability to control the light phase at any point on the grating. I will be researching the applications of LCoS using silicon nitride gratings in a visible wavelength range for beam steering and beam shaping.

6

CHAPTER 6: POLARISATION INDEPENDENT HCGS FOR HIGH REFLECTIVITY LCOSDS

This chapter presents the design of polarisation-independent gratings and their reflectivity studies in two near-infrared wavelength ranges, including C-Band and 1064 nm.

6.1 POLARISATION-INDEPENDENT HCGS FOR HIGH-REFLECTIVITY LCOS IN NEAR-INFRARED

The proposed structure consists of a single layer of cross-linked silicon polarisation-independent high-contrast grating structures embedded on top of a conventional bi-periodic LCoS backplane.

I have numerically optimised reflectivity associated with the linearly polarised s and p input light from cross-linked gratings to increase the efficiency of LCoSDs and observed a significant polarisation-independent increase in the reflectivity in telecommunication C-band and 40nm wavelength range around 1.064 microns for two different designs.

6.1.1 Introduction

Subwavelength gratings are periodic structures with many properties and applications since they can be easily fabricated. A two-dimensional sub-wavelength HCG features broadband reflectivity and is much thinner than the conventional Bragg reflectors proposed based on[41] guided-mode resonance. It is known that LCoSDs suffer from diffractive losses due to the structure consisting of a 2D- array of metallic pixels that are individually addressable. Previous efforts to remove these losses employed Bragg reflector mirrors [86]and diffractive gratings[87-88]. In this work, I use a cross-linked HCG[89] to significantly increase the reflectivity of LCoS pixel structure in broad wavelength ranges for both **s** and **p** polarisations. I have also numerically investigated the fabrication tolerances of the proposed LCoS design in the two different wavelength regimes of an optimised structure.

6.1.2 Polarisation-independent high contrast grating

Figure 6.1(a, b) shows high contrast grating structure, consisting of two-dimensional cross-linked silicon grating with rectangular rod cross-section on top of a bi-periodic aluminium pixel structure with dimensions of a typical LCoS [88]. The design parameters for the grating are the grating thickness ($\mathbf{t_g}$), thickness of low index layer ($\mathbf{t_l}$), width of silicon grating ($\mathbf{w_x,w_y}$) and pitch of the grating ($\mathbf{d_x,d_y}$). Since the proposed structure is designed to have a broad reflection efficiency for LCoS devices, the reflection from the silicon substrate's back surface need not be considered [90].

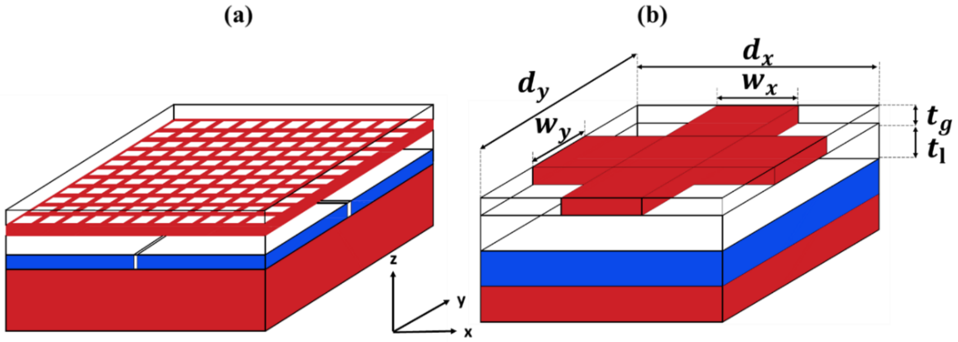

Figure 6.1 (a, b). Schematic diagram of the crosslinked grating on top of LCoS pixels and unit cell (a) Schematic of high-contrast silicon grating on top of conventional LCoS pixels. The single layer of cross-links consists of a rectangular rod cross-section of silicon and silica (b) The unit cell of HCG describes the pitch along the x-axis as d_x and pitch along with y-axis d_y and width of high index material silicon along x-axis w_x and width along y-axis w_y, t_g is the thickness of the grating structure, and t_l is the thickness of low index layer as shown in the figure.

I have optimised the structure to have high reflection efficiency and a broad wavelength band centred at 1550 nm and 1064 nm using rigorous coupled-wave analysis (RCWA) with GD-Calc[91] under MATLAB environment.

6.2 RESULTS AND DISCUSSION

6.2.1 Numerical simulation

The design of the cross-linked structure having silicon high HCG structure surrounded with low index silica material begin with the materials and parameters of one-dimensional grating mentioned in [88] and found that a set of parameters including periodicity of HCG along with x and y $\mathbf{d_x} = \mathbf{d_y}$ =750 nm, the width of silicon HCG $\mathbf{w_x} = \mathbf{w_y}$ =280 nm, the thickness of grating $\mathbf{t_g}$=180 nm, the thickness of aluminium layer below silica layer $\mathbf{t_l}$=80 nm. I have simulated the cross-linked high contrast grating structure without pixel with a plane wave having normal incidence from 1520 nm to 1580 nm and observed both the s and p polarisation component of reflection efficiency overlaps over 60 nm band giving rise to polarisation independent high reflectivity more than 99% shown in Figure 6.2 (b). In setting simulation parameters, Silicon act as the substrate having infinite thickness along Z-axis, air as the superstrate, the homogeneous low index silica layer is beneath the cross-linked grating, and the homogeneous aluminium layer is below the silica grating. I have considered the boundary condition of the two-dimensional grating to be periodic in the x and y dimensions, as shown in Figure 6.2(a). The unit cell of the crosslinked HCG on top of silica is simulated using GD-Calc, and the detailed process of generating the structure is outlined in Appendix A.1.2.

Figure 6.2(a) shows that the 90° rotational symmetry of the cross-linked grating structure introduces polarisation-independent reflectivity. Suppose multiple guided resonance modes combine and happen to locate at close spectral vicinity and have the ability to couple well together. In that case, Figure 6.2(b) shows that maximum reflection efficiency can be attained in a broad wavelength range [41].

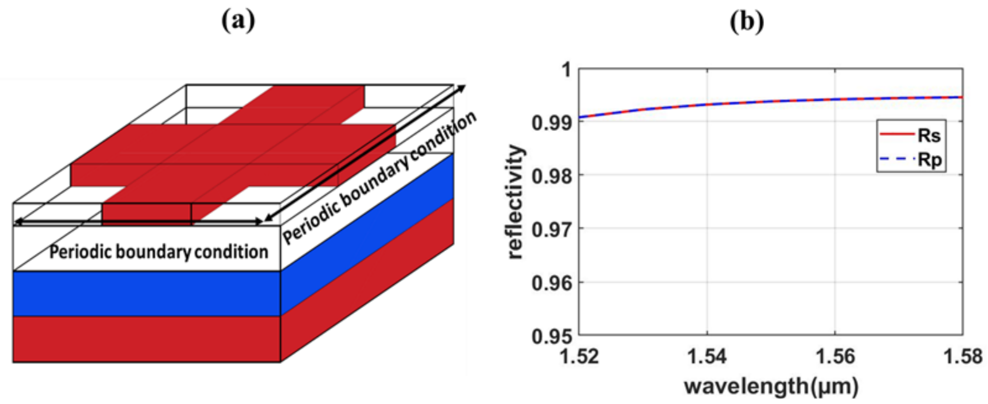

Figure 6.2 (a, b). Cross-linked 2D grating with periodic boundary conditions along x and y, reflectivity simulated in C-Band (a) The unit cell of cross-linked two-dimensional high contrast grating structure without pixels and periodic boundary condition on x and y axes (b) Reflection efficiency simulated with a plane wave of normal incidence, obtain a broad reflection efficiency of more than 99% from 1520 nm to 1580 nm band centred at 1550 nm. The reflection efficiency enhances after adding cross-link HCG on top of the aluminium layer.

6.2.2 Conventional LCoS backplane

Conventional LCoS refers to the LCoS backplane consisting of bi-periodic aluminium pixels on top of a silicon substrate [88]. Figure 6.3(a) shows a periodicity of 9.2 microns and a dead space or pixel gap of 200 nm on both axes. The metallic pixel introduces diffractive optical losses. Coating with distributed Bragg reflector mirrors on top of the pixelated backplane could lead to a larger cavity size for mitigating [86]diffractive optical losses associated with the pixel structure. I have defined the boundary conditions of the bi-periodic metallic unit cell periodic along x and periodic along y, set air as superstrate, silica layer on top of the pixel with finite thickness and silicon as a substrate having infinite thickness along z. The addition of a cross-linked structure, as shown in Figure 6.1(b) on top of the pixelated design shown in Figure 6.3(a), leads to a novel high reflectivity LCoS structure, as shown in Figure 6.1(a). The simulated reflection efficiency of the LCoS with grating and pixels offers lower optical loss associated with the absorption and diffraction that occur from the pixelated electrode.

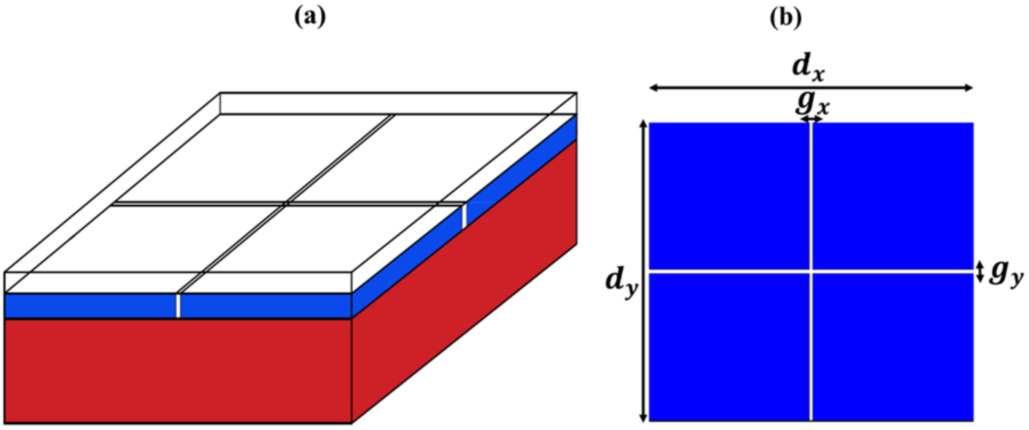

Figure 6.3 (a, b). Schematic diagram of the conventional LCoS backplane with equal periodicity (a) Perspective view of conventional LCoS having bi-periodic metallic pixels on top of aluminium substrate. (b)The top view of the LCoS structure shows the periodicity along x and y as $\mathbf{d_x}$ and $\mathbf{d_y}$, respectively, pixel gap filled with silica along x and y as $\mathbf{g_x}$ and $\mathbf{g_y}$, respectively.

The LCoS structure optimised for telecom wavelength C-band and 1-micron range, enhancement of reflection efficiency components showed the enhanced broad reflection range observed in Figure 6.4(a,b).

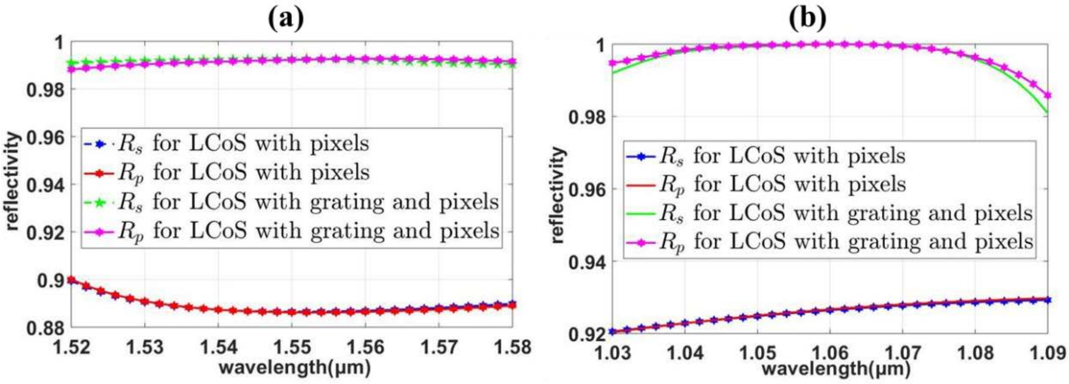

Figure 6.4 (a, b). Comparison of reflectivity in C-band and at around 1064 nm. The increase of R_s (pink) and R_p (green) reflectivity provided by the inclusion of the HCG with optimised parameters compared to R_s (red) and R_p (blue) for conventional LCoS at 1550 nm (a) and 1064 nm (b).

The zeroth-order reflection efficiency of the **s** and **p** linear polarisation components gets an enhancement of 99.3% at 1550 nm after adding the cross-linked two-dimensional high contrast grating. Similarly, the reflection efficiency of LCoS enhances from 92% to 100% at 1064 nm. The guided resonance modes in close spectral vicinity between the grating thickness and the low index layer contribute to the maximum reflection efficiency in a broad wavelength range [41].

6.2.3 Two-dimensional grid optimisation and fabrication tolerance

When the LCoS with grating and pixel has been fabricated, one of the critical design parameters of the LCoS with grating and pixel prone to error is the width of silicon due to its small dimensional features. The first step is to find the optimum periodicity and width of silicon corresponding to maximum reflection efficiency with the initial design parameters of the 1D grating size mentioned in[88]. The two-dimensional grid consists of grating periodicity along the x-axis, the width of silicon grating along the y-axis plotted against reflection efficiency at the wavelength of 1550 nm and 1064 nm, respectively, as shown in Figures 6.5(a) and 6.5(b). The maximum value of reflection efficiency and its corresponding periodicity and width of silicon was observed and plotted against a 100 nm wavelength range in telecom wavelength C-band and 1-micron range as fabrication tolerances for individual design parameters.

For the case of 1550 nm optimisation, I have varied the periodicity value from 300 nm to 850 nm and the width of silicon from 60 nm to 280 nm. I have obtained the optimum value of periodicity and width of silicon as 800 nm and 270 nm, as shown in Figure 6.5(a). Figure 6.5(b) shows a two-dimensional grid consisting of silicon width varying from 130 nm to 330 nm and wavelength ranging from 1500 nm to 1600 nm plotted against reflection efficiency. The optimised width of silicon is 270 nm, and its tolerance value goes from 130 nm to 320 nm. The fabrication tolerance of silicon width will be ±50 nm to maintain a reflectivity higher than 99% at a wavelength of 1550 nm. Optical lithography could be able to meet the grating width with ±50 nm tolerance[92]. Figure 6.5(c) shows the fabrication tolerance of the grating thickness. The grating thickness varies from 140 nm to 340 nm. At 180 nm grating thickness, the reflection efficiency is 99.3%, and the fabrication tolerance is ±40 nm for more than 99% of the reflection efficiency. Figure 6.5(d) shows the fabrication tolerance of the low-index layer. The thickness of the low index layer beneath the grating varies from 170 nm to 570 nm, and the incidence wavelength ranges from 1500 nm to 1600 nm. The maximum value of reflection efficiency equals 99.3% at 1550 nm, and the corresponding optimum value of the thickness of the low index layer equals 210 nm, as shown in Figure 6.5(d). The fabrication tolerance of the thickness of the low index layer is 210 nm ±40 nm to keep the reflectivity greater than 99% at 1550 nm. The optimisation and fabrication tolerances at around 1550 nm are summarised in Table 6.1.

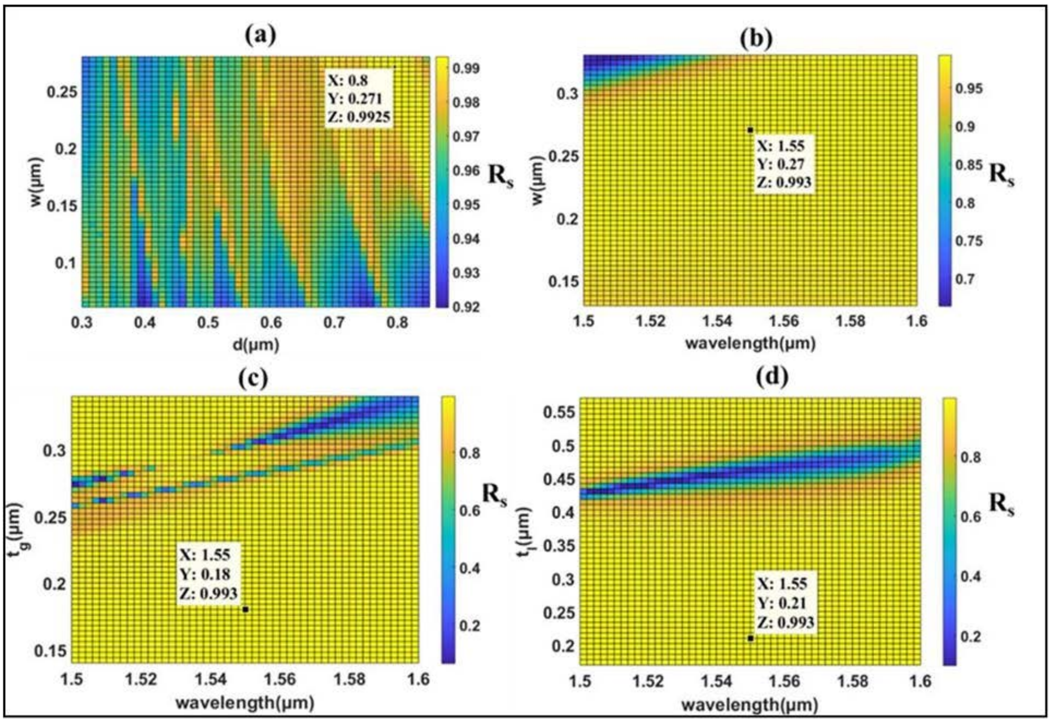

Figure 6.5 (a, b, c, d). Two-dimensional grid optimisation and fabrication tolerance at around 1550 nm. (a) The two-dimensional grid consists of the width of silicon(w) along the x-axis and period(d) along the y-axis against the R_s component of reflection efficiency with a grid size of 51*51. The optimised value of period and width of Si for a maximum reflectivity of 99.3% as 800 nm and 270 nm, respectively. (b) A two-dimensional grid showing the fabrication tolerance of the width of Si along with the x-axis and wavelength band along the y-axis against the R_s component of reflection efficiency-optimised width of Si is 270 nm. (c) The two-dimensional grid shows the fabrication tolerance of grating thickness and its optimised value of 180 nm. (d) Two-dimensional grid showing the fabrication tolerance of low index layer and its optimised value is 210 nm.

Wavelength of incidence	Optimal periodicity(d) at 1550 nm	Optimal width of Si(w) at 1550 nm ±tolerance	Optimal grating thickness(t_g) at 1550 nm ±tolerance	Optimal thickness of low index layer(t_l) at 1550 nm ±tolerance
1500 nm-1600 nm	800 nm (33.8% Duty Cycle)	270 nm ±50 nm (more than 99% of R_S)	180 nm ±40 nm (more than 99% of R_S)	210 nm ±40 nm (more than 99% of R_S)

Table 6.1. Summary of optimisation at around 1550 nm. The table summarises the optimisation and fabrication tolerance of the LCoS backplane with pixels and polarisation-independent HCG.

For the case of 1064 nm optimisation, I have varied the periodicity value from 300 nm to 800 nm and the width of silicon from 60 nm to 280 nm. I have obtained the optimum value of periodicity and width of silicon as 524 nm and 214 nm for a maximum reflectivity value, as shown in Figure 6.6(a).

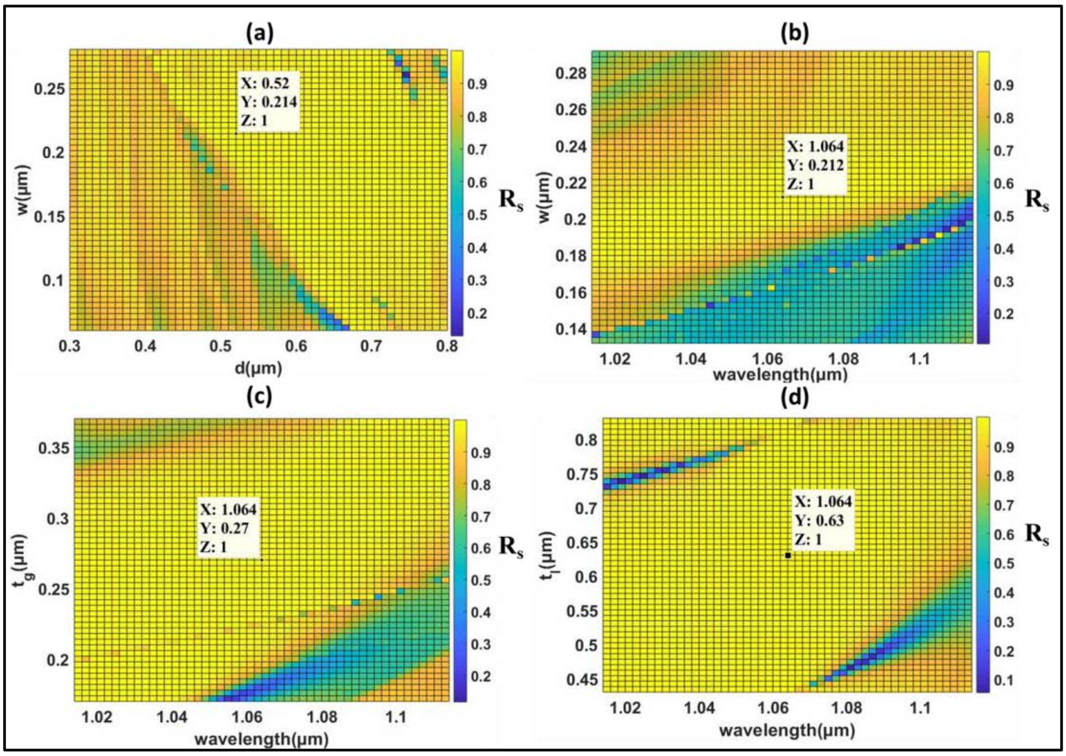

Figure 6.6 (a, b, c, d). Two-dimensional grid optimisation and fabrication tolerance at around 1064 nm. (a) The two-dimensional grid consists of the width of silicon(w) along the x-axis and period(d) along the y-axis against the R_s component of reflection efficiency with a grid size of 51*51. The optimised value of the period and width of Si for a maximum reflectivity of 100% is 520 nm and 214 nm, respectively. (b) A two-dimensional grid showing the fabrication tolerance of the width of Si along with the x-axis and wavelength band along the y-axis against the R_s component of reflection efficiency-optimised width of Si is 212 nm. (c) Two-dimensional grid showing the fabrication tolerance of grating thickness and its optimised value is 270 nm. (d) Two-dimensional grid showing the fabrication tolerance of low index layer and its optimised value is 630 nm.

Figure 6.6(b) shows a two-dimensional grid consisting of silicon width varying from 130 nm to 330 nm and wavelength ranging from 1014 nm to 1114 nm plotted against reflection efficiency. The optimised width of silicon is 214 nm, and its tolerance value goes from 190 nm to 230 nm. The optimised duty cycle is 40% for near-unity reflection at 1064 nm. The fabrication tolerance of silicon width will be ±20 nm to maintain near unity reflection of 100% at a wavelength of 1064 nm. Optical lithography could be able to meet the grating width with ±20 nm tolerance[92]. Figure 6.6(c) shows the fabrication tolerance of grating thickness from 1014 nm to 1114 nm. The grating thickness in the two-dimensional grid varies from 170 nm to 370 nm, and 100% reflection was obtained at 1064 nm. The optimum value of grating thickness equals 270 nm, and its fabrication tolerance is ±40 nm to maintain near unity reflection over 40 nm. Figure 6.6(d) shows the fabrication tolerance of the low-index layer. The thickness of the low index layer beneath the grating varies from 430 nm to 830 nm, and the wavelength ranges from 1014 nm to 1114 nm. The maximum value of reflection efficiency equals 100% at 1064 nm, and the corresponding optimum value of the low index layer thickness equals 630 nm, as shown in Figure 6.6(d). The fabrication tolerance of the thickness of the low index layer is 630 nm ±80 nm to keep the 100% reflection efficiency at 1064 nm. The optimisation and fabrication tolerances at around 1064 nm are summarised in Table 6.2.

Wavelength of incidence	Optimal periodicity(d) at 1064 nm	Optimal width of Si(w) at 1550 nm ±tolerance	Optimal grating thickness(t_g) at 1550 nm ±tolerance	Optimal thickness of low index layer(t_l) at 1550 nm ±tolerance
1014 nm-1114 nm	520 nm(41% Duty Cycle)	214 nm ±20 nm (more than 99.5% of R_S)	270 nm ±40 nm (more than 99.9% of R_S)	630 nm ±80 nm (more than 99.9% of R_S)

Table 6.2: Summary of optimisation at around 1064 nm. The table summarises the optimisation and fabrication tolerance of the LCoS backplane with pixels and polarisation-independent HCG.

6.3 CONCLUSION

I have optimised the design of a two-dimensional cross-linked high contrast grating structure to increase the performance of LCoS in near-infrared wavelength ranges for both linear polarisation components of the reflectivity. The optimised parameters for the LCoS at C-band, including the periodicity, equals 800 nm, the width of the silicon stripe equals 270 nm, the duty cycle equals 33.7%, the silicon stripe thickness is 180 nm, and the thickness of low index silica layer below grating equals 210 nm. The LCoS structure was optimised for a more than 99% broadband reflection efficiency from 1520 nm to 1580 nm centred at 1550 nm. The fabrication tolerance of the design parameters is adequate for optical lithography and the ease of fabrication. For 1064 nm optimisation, the cross-linked LCoS structure acts as a broadband reflector having both polarisation components overlapping to 100% of reflection efficiency. The unity reflection of LCoS at 1064 nm is observed at a cavity length of 270 nm, which is much shorter than the cavity length of LCoS employing a DBR mirror. Bragg mirror coatings introduce fringing fields; the layer's stress makes it impossible for an optically flat LCoS. The industry aims to mitigate the stress associated with the coating of multilayer Bragg mirrors on top of conventional LCoS. They have implemented optical lithography to inscribe the HCGs. Though the coating with the multi-layer Bragg mirrors is less expensive, the industry aims to focus on the device size and mitigate the thermally induced stress for a better product. In the next chapter, I will manipulate the linear polarisation components using uni-periodic metal-dielectric grating. I aim to modulate both polarisation states in phase with a relative phase shift of 180 degrees.

7

CHAPTER 7: METAL-DIELECTRIC GRATING FOR POLARISATION INDEPENDENT LCOSDS

This chapter represents the study of the phase response of metal-dielectric uniperiodic pixels inscribed on the LCoS backplane, which rotates the s- and p polarisation components to 180 degrees, providing polarisation-independent reflectivity. Here I optimise the structure at 1550 nm and 1064 nm for polarisation-independent reflectivity and π-phase difference.

7.1 INTRODUCING ANISOTROPIC STRUCTURE VIA UNI-PERIODIC METAL-DIELECTRIC GRATING

The LCoSDs are known for being implemented as optical phase modulators. It's an efficient platform for manipulating light by imposing a spatially dependent phase profile on the optical signal. Beam steering, signal compensation and wave-shaping are significant examples of LCoS. A conventional LCoS, as mentioned in Figure 7.1, consists of LC material filled between transparent glass layers with a transparent electrode. The biperiodic pixelated backplane is embedded on top of silicon CMOS circuitry. Each pixel is individually addressable by a voltage signal to provide a local phase change to the transmitted optical light from LC material. This leads to the formation of a two-dimensional array of phase-manipulating regions. The layers align along the long axis of the individual LC crystals, thereby defining the slow axis of the LC molecule. The LC medium enacts as an anisotropic dielectric with the birefringent axis (as shown in Figure 1.2(a)) in the direction of the long axis of the LC molecule. The alignment layers generally consist of tiny grooves by rubbing polyamide layers, which align the long axis of the LC cells to the slow axis of the LC element. Thus, LC elements are inherently polarisation-dependent.

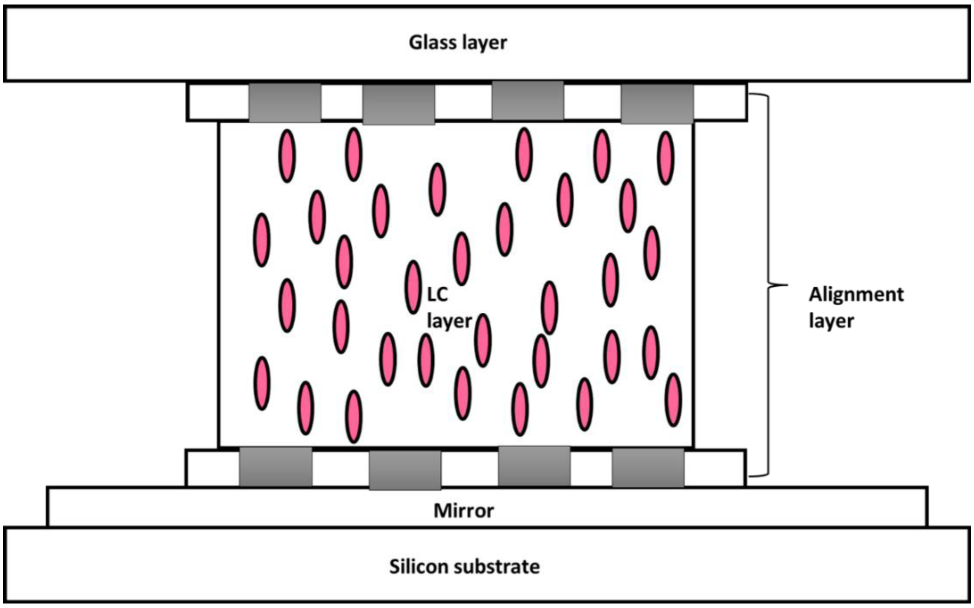

Figure 7.1. Conventional LCoS with pixelated backplane embedded on the silicon CMOS panel[49].

In the non-normal angle of incidence, the light transmitted through the LCoS devices, one of the phase of the linear polarisation components, undergoes a phase change to a greater degree than the other linear orthogonal polarisation component. One of the methods implemented earlier would be possible to account for the polarisation dependence by spatially separating one linear polarisation component and sending one component to a half-wave plate or double pass through a quarter-wave plate. G.D Love et al.[93] introduced this technique to implement LCoS devices insensitive to polarisation changes introduced by LC cells by combining the double pass of the LCoS and quarter-wave plate, as shown in Figure 7.2.

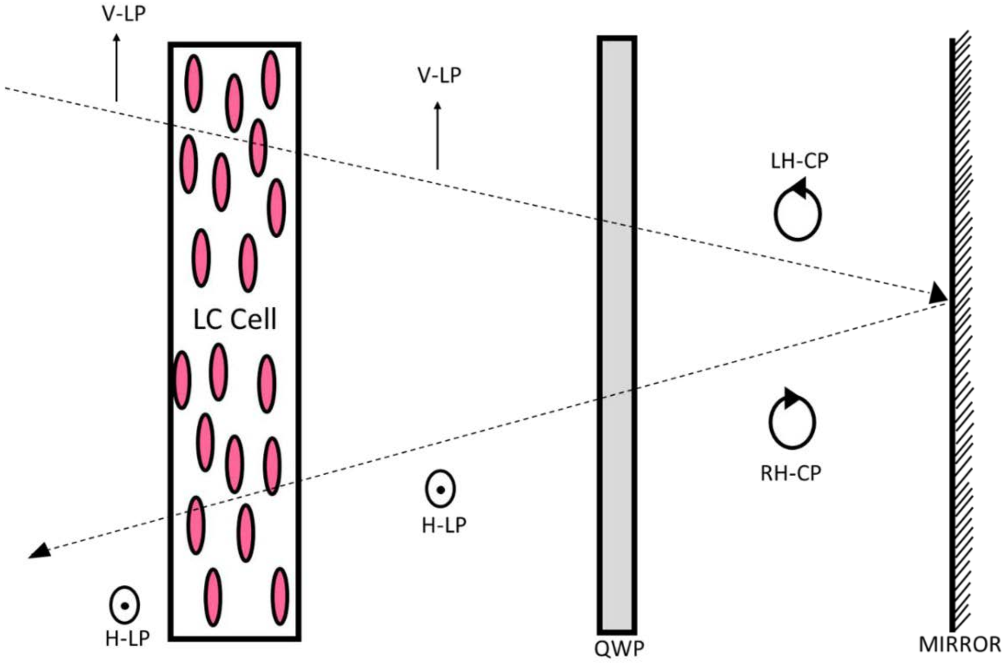

Figure 7.2. The schematic diagram of standard LCoS[93] made polarisation insensitive by double passing the optical signal into the quarter-wave plate.

As shown in Figure 7.2, the schematic diagram describes a vertically polarised light made to incident o an LC cell that will be converted into circularly polarised light after propagation through a quarter waveplate. After the passage from the mirror, the left circularly polarised light becomes the right circularly polarised light. Then the RHCP (right-handed circularly polarised) light again passes through the quarter waveplate. Then, the light passes back through the liquid crystal cell polarised at 90 degrees to the input polarisation leading to a π-phase shift between linear orthogonal polarisation components. The LC thickness typically varies between 6 microns to 10 microns, plus the quarter-wave plate thickness of about 40 microns for telecom wavelength increases the device thickness, enhancing the required drive voltages.

One technique involves the inclusion of twisted nematic liquid crystal, at least in a transmission configuration. The twisted nematic LCs twist accordingly with the applied voltage up to 90 degrees. This leads to controlling the LC by using a predetermined voltage.

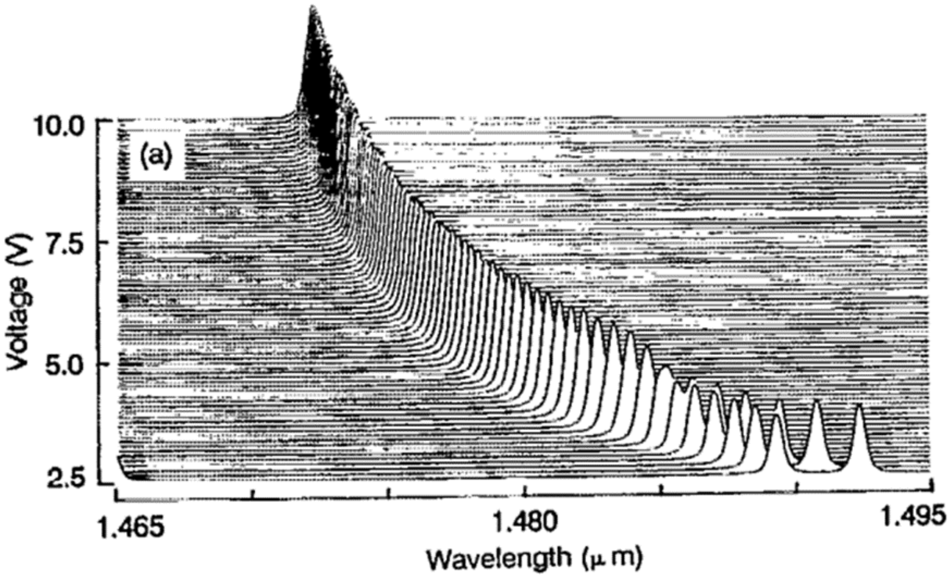

Figure 7.3. Illustration of Fabry-Perot resonance in a twisted nematic liquid crystal cell explained in[94] . Adapted with permissions from © AIP Publishing.

In[94], a twisted nematic LC is implemented as a Fabry-Perot cavity, and the resonance is independent of the polarisation of the incoming optical signal. The refractive index change associated with the orthogonal polarisation components was the same to perform as a polarisation-independent Fabry-Perot cavity. As shown in Figure 7.3, there is a threshold[94] for the polarisation independence operation. At a lower applied voltage value, the peaks are separated with a significant gap; meanwhile, the peaks are close at higher voltages. At low drive voltages, orthogonally polarised inputs experience slightly different resonance positions, i.e., the LC behaves birefringent and polarisation dependent. Meanwhile, at higher voltages, much higher than the threshold, the polarisation dependence is significantly reduced.

The bi-periodic island HCG in chapter 6 indeed provides polarisation-independent reflectivity. To switch the **s** and **p** polarisation components, Finisar[49] introduced a sub-wavelength metal-dielectric grating structure that exhibits an anisotropic refractive index profile in orthogonal lateral dimensions. I have optimised the design in the near-infrared wavelength range. The incident light through the liquid crystal element and metal-dielectric grating is reflected and experiences a phase difference of 180 degrees between its polarisation components. It rotates each **s** and **p** component into orthogonal orientation upon reflection. Here I analyse the polarisation independent uni-periodic metal-dielectric pixel structure in[49]. Finisar invented an LCoS device to ease the polarisation diversity, thereby embedding a thoughtful subwavelength design in each pixel, preferably having a periodic metallic profile in at least the first lateral dimensions. Here I have optimised the structure to have independent polarisation reflectivity and π-phase shift between orthogonal polarisation components of reflectivity.

The structure consists of silicon as a substrate and silica as a superstrate. The refractive indices of Aluminium[77], Silicon[78] and Silica[76], are 15.657+ i (1.5723), 3.48, and 1.38, respectively. The uni-periodic grating has a pitch along the X-axis of 0.75 microns. The width of aluminium material between the silica bars is 0.25 microns along the X-axis, as shown in Figure 7.4. The simulated structure is shown in figure 7.4; the whole system is divided into four strata to model the design in GD-Calc. The top stratum or the superstrate is a homogeneous silica layer having a thickness along the z-axis of 0.12 microns. The second stratum is uni-periodic consists of both aluminium and silica, constituting the subwavelength structure having a thickness of 0.32 microns. The homogeneous stratum beneath the uni-periodic stratum is the aluminium layer, with a thickness of 0.08 microns. The silicon is the substrate layer having an infinite thickness.

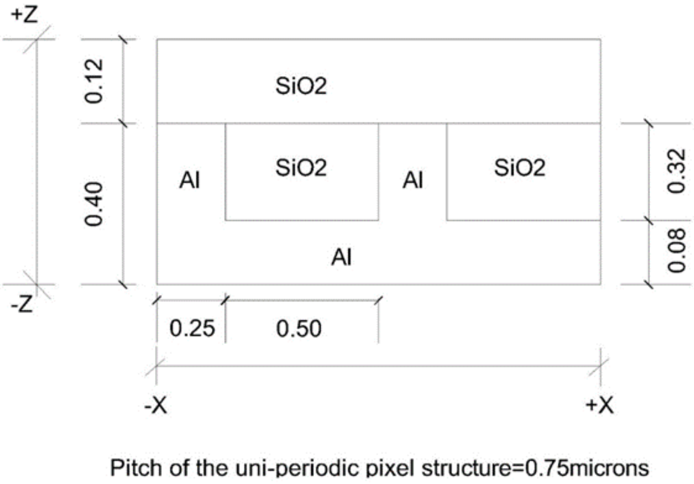

Figure 7.4. X-Z view of the uni-periodic subwavelength structure with a periodicity of 0.75 microns as shown in[49] (all dimensions are in microns).

7.1.1 Working principle of the metal-dielectric subwavelength grating

The optical phase modulator developed by Finisar consists of LC element and a pair of opposing electrodes for supplying a voltage across the LC element to drive the liquid crystals in a predetermined configuration. The grid of individually addressable pixels includes a uni-periodic metal-dielectric subwavelength grating that provides an anisotropic refractive index profile in orthogonal lateral dimensions. The effective index profile creates a material form birefringence, thereby introducing the reflected light to a relative phase difference of 180 degrees between its constituent polarisation components—each **s** and **p** polarisation component during operation experiences equal phase retardation by the liquid crystal element. The axis is defined by the subwavelength grating structure on pixels ideally kept at 45 degrees to the slow axis of the LC element to achieve equal phase retardation. The polarisation-independent LCoS optical phase modulator developed by Finisar, as shown in Figure 7.5, operates with a substantially reduced polarisation independence. As per the patent, the reflection efficiency difference associated with the linear polarisation components is 2%. Here I employ optimisation algorithms to improve the ideal reflection efficiency difference of near-zero and the 180-degree phase difference in 1550 nm and 1064 nm wavelengths. Furthermore, the uni-periodic metal-dielectric grating on top of pixels itself acts as a conducting electrode and provides the polarisation rotation; no other phase retardation layers are required, such as a quarter-wave plate. As a result of the absence of additional elements, the associated voltage drop or optical attenuation experienced with known devices is further reduced, and polarisation independence is achieved.

Figure 7.5 consists of the silicon substrate and an outer transparent aqua glass superstrate for receiving and transmitting light from a source. The LC element is sandwiched between alignment layers formed of polyimide. These layers align the LC crystals' long axis within the element's predefined orientation. The electrode is situated between the glass and alignment layers formed of index-matching indium tin oxide to reduce the refraction of incoming light passing through the electrode. The electrode consists of individually drivable pixels for independently driving local LCs in a predefined manner, and the periodic grating is disposed between the alignment layer and silicon substrate. The pixels are electrically isolated with an interpixel gap filled with silica.

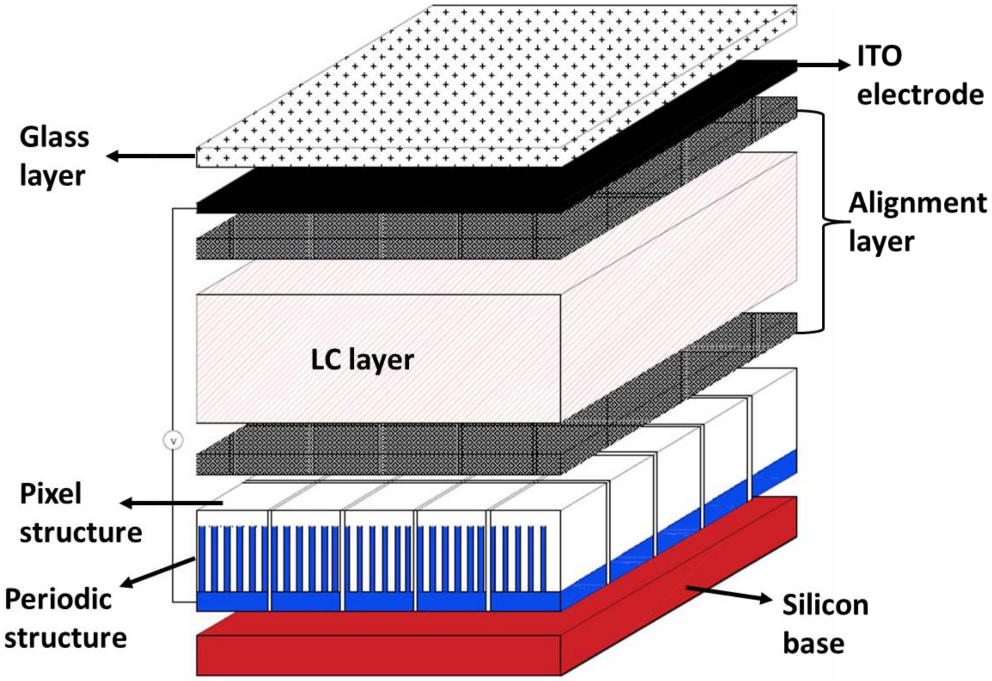

Figure 7.5. Exploded perspective view of polarisation independent LCoS[49] having uni-periodic metal-dielectric grating embedded on pixels.

The periodic grating structure is formed to mesh together in the projecting regions consisting of a lower electrically conductive aluminium layer and a recess region composed of silicon-dioxide layer in a key-like form, as shown in Figure 7.5. The `periodic subwavelength grating structure in the x-dimensions alters the effective index of refraction of the incident light polarised in the x-dimension with respect to the y-dimension. This relative refractive index difference and the subwavelength dimensions provide birefringence in the material, introducing relative phase changes between **s** and **p** polarisation components. The relative phase difference of 180 degrees provided by the subwavelength grating rotates the **s** and **p** polarisation components by 90 degrees.

Figure 7.6 represents the ray diagram of incident light through the LC element and reflected back from the electrode pixel having a subwavelength metal-dielectric uniperiodic structure extending vertically.

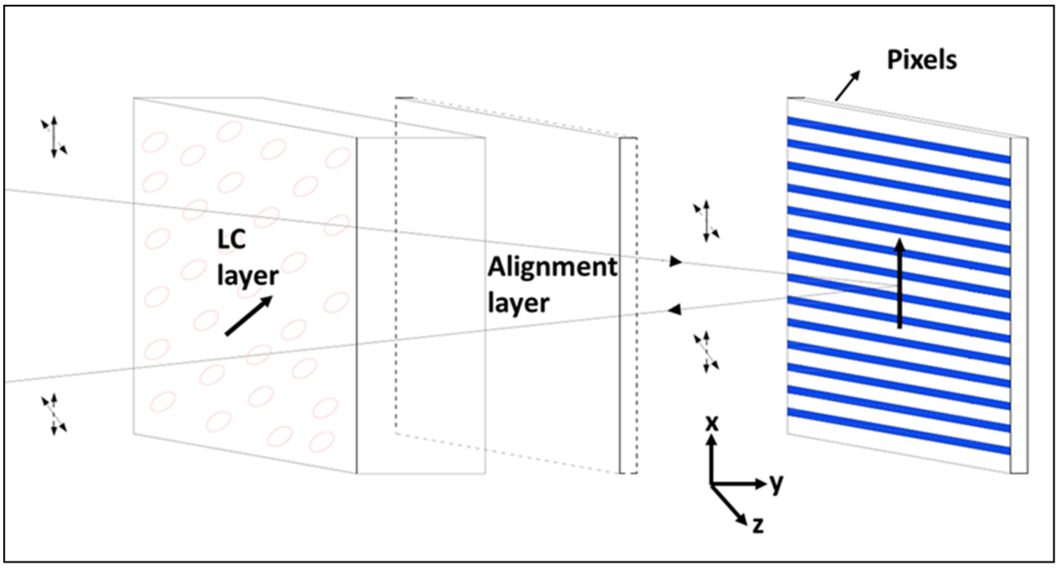

Figure 7.6. Side exploded perspective view of polarisation independent LCoS[49] showcasing the polarisation modification process.

The alignment layer doesn't contribute to the polarisation alteration process. The polarisation of the incident optical signal is resolved into **P**(vertical-solid arrow) and **S**(horizontal-dashed arrow) vectors. In use, the light initially passes through the LC element, and the slow axis of the LC element is modified by phase retardance. The orthogonal polarisation component to the slow axis does not undergo phase retardance. Then the light passes through the aluminium pixel and reflects back by experiencing a 180 degrees relative phase difference. In effect, the polarisation components are being swapped after reflecting off the pixel, such that the original vertical components are horizontal and vice versa. The subwavelength grating nullifies the polarisation difference introduced by the LC element. The device performs as a polarisation-independent phase modulator by applying an appropriate driving potential across the LC element.

7.2 RESULTS AND DISCUSSION

7.2.1 Polarisation independent LCoS optimisation at 1550 nm

For polarisation-independent LCoS, the conditions that must be satisfied include near polarisation-independent reflectivity, i.e., (the difference between orthogonal linear polarisation component of reflectivity must be near zero) and 180-degree phase rotation among orthogonal reflection components. The model I have obtained from[49] has an orthogonal reflection efficiency difference of nearly 2% and shows 180 degrees of phase rotation. Ideally, the structure must show a polarisation-independent reflectivity, i.e., the R_s-R_p=0 at 1550 nm with a phase difference between s and p components of 180 degrees.

7.2.1.1 The Optimisation of uni-periodic metal-dielectric structure using surface plots and pseudo-colour plots

I initially implemented the grid optimisation algorithm to observe how the model behaves to the critical design parameters including periodicity, and width of Al grating. The surface plot consists of grating periodicity along the x-axis from 0.5 microns to 1 micron, the width of aluminium along the y-axis varying from 0.4 microns to 0.05 microns and phase difference along the z-axis modelled at 1550 nm wavelength of incidence as shown in Figure 7.7(a). The grid consists of 51*51 points, and I have observed many points having pi-phase differences, as shown in Figure 7.7(a).

I have simulated the structure having grating parameters from the surface plot with a plane wave of normal incidence from 1.45 microns to 1.65 microns and observed the difference of Rs and Rp as nearly 1% with a phase difference of 180 degrees, as shown in Figure 7.7(b) and Figure 7.7(c) respectively. The two-dimensional grid phase plot indicates that many points correspond to the π-phase shift. A polarisation-independent LCoS ideally needs to have a near-zero reflection efficiency difference.

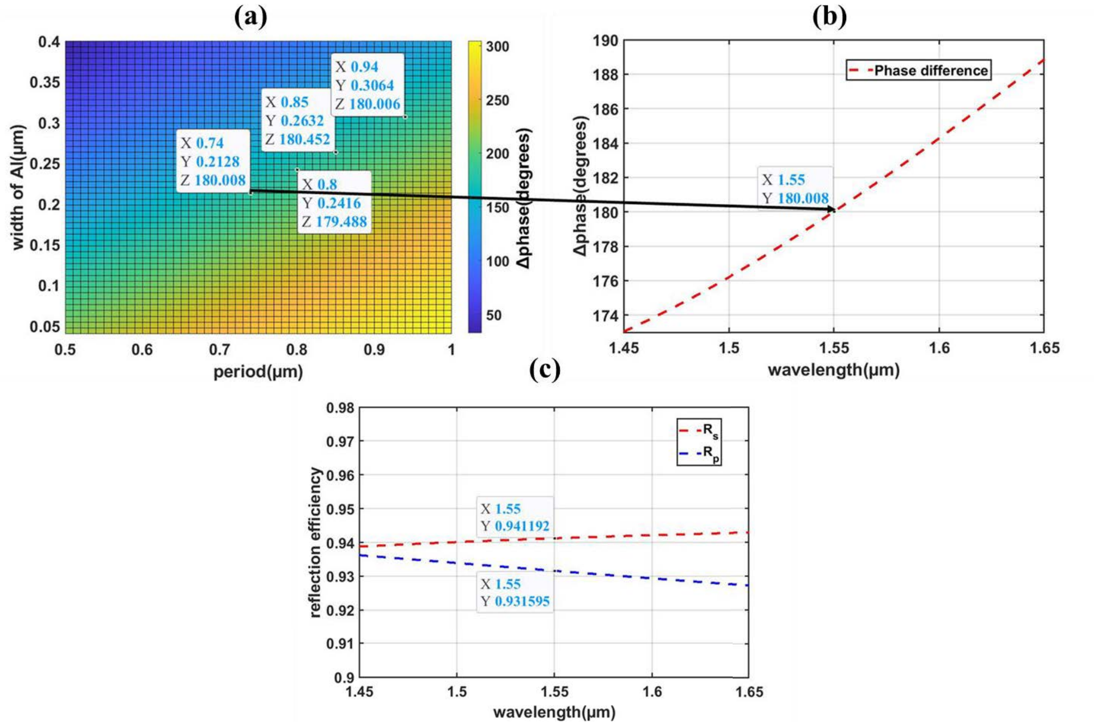

Figure 7.7 (a, b, c). Grid optimisation to observe the grating parameters dependent on the phase difference. The two-dimensional grid consists of the period along the x-axis and width of Al grating, the y-axis and phase difference along the z-axis. The points correspond to pi-phase rotation between the s and p components. (b) With periodicity equal to 740 nm and width of Al equal to 213 nm, the phase difference was simulated and observed 180-degree phase rotation at 1550 nm. (c) The reflection efficiency plot was simulated over 1450 nm to 1600 nm and observed a 1% difference in reflection efficiency between **s** and **p** components at 1550 nm.

The phase plot shows that the phase difference of 180 degrees occurs at many grating parameter combinations, as shown in Figure 7.7 (a). The difference in reflection efficiency components at 1550 nm is R_s-R_p = 1%, which must be optimised. Then I simulated the pseudo color plots corresponding to the minimum of R_s-$R_p = \Delta R$ and phase angle (phase angle-180 degrees) within the range of 0.5 microns to 1 microns periodicity and 0.05 microns to 0.4 microns width of Al as shown in Figure 7.7 (a) and Figure 7.7 (b) respectively. Both pseudo-colour plots clearly show how the minimum value of both parameters varies along with the grid plot. The point of intersection of the curves represents the grating parameters corresponding to both Δ*R* nearly equal to zero and phase difference almost equal to 180 degrees.

Figures 7.8 (a) and (b) represent the pseudo-colour plots of the ΔR and phase difference minimum, respectively. The non-linear curves intersect at a point where both the condition of polarisation independent operation satisfies. But at this interval of periodicity and width of grating, the non-linear curves (blue curves shown in Figure 7.8 (a,b)) do not intersect, and I have extended the interval limits towards the left, as shown in Figure 7.9 (a,b). Al grating width and periodicity vary from 50 nm to 180 nm and 200 nm to 600 nm in a 2D grid. Here I have optimised the point of intersection at a period of 392 nm and a width of 65 nm, as shown in Figure 7.9(c).

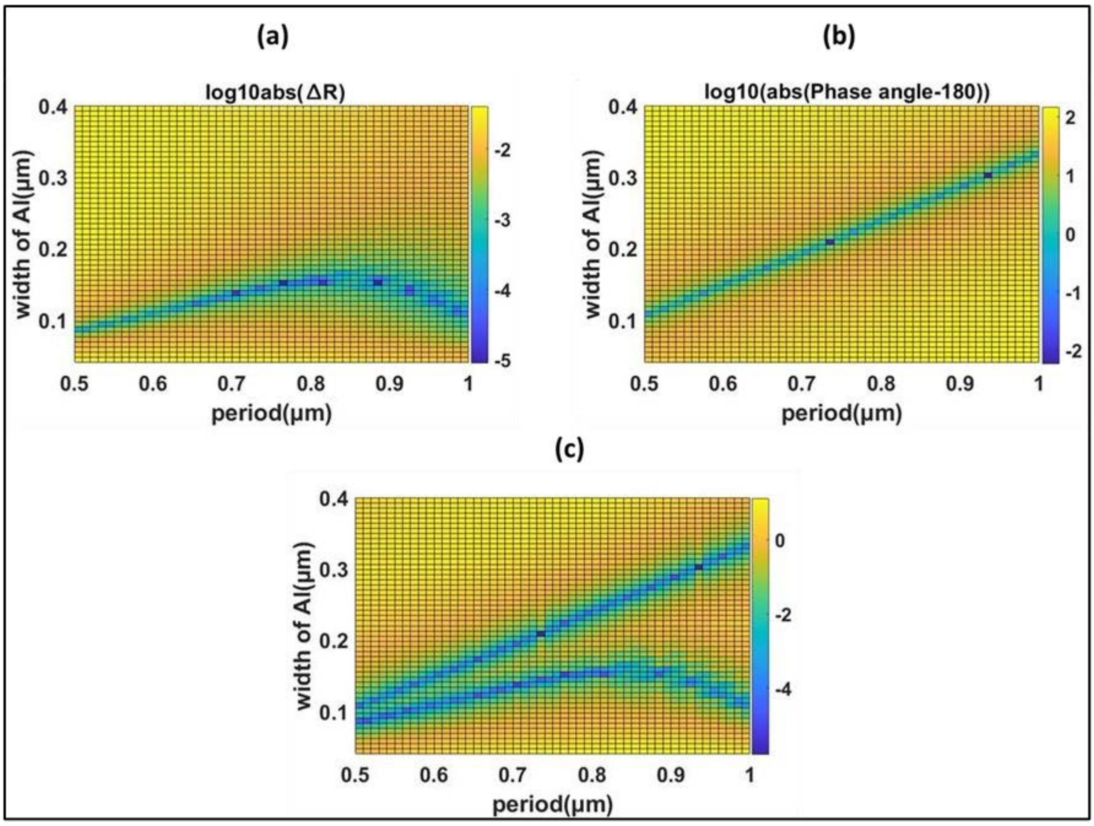

Figure 7.8 (a, b, c). Pseudo colour optimisation of phase difference and reflectivity difference. Pseudo-colour plots consist of a minimum of Δ*R* (a), minimum of phase angle (b), and (c) normalised minimum of both((a) and (b)), representing the overlapping of (a) and (b).

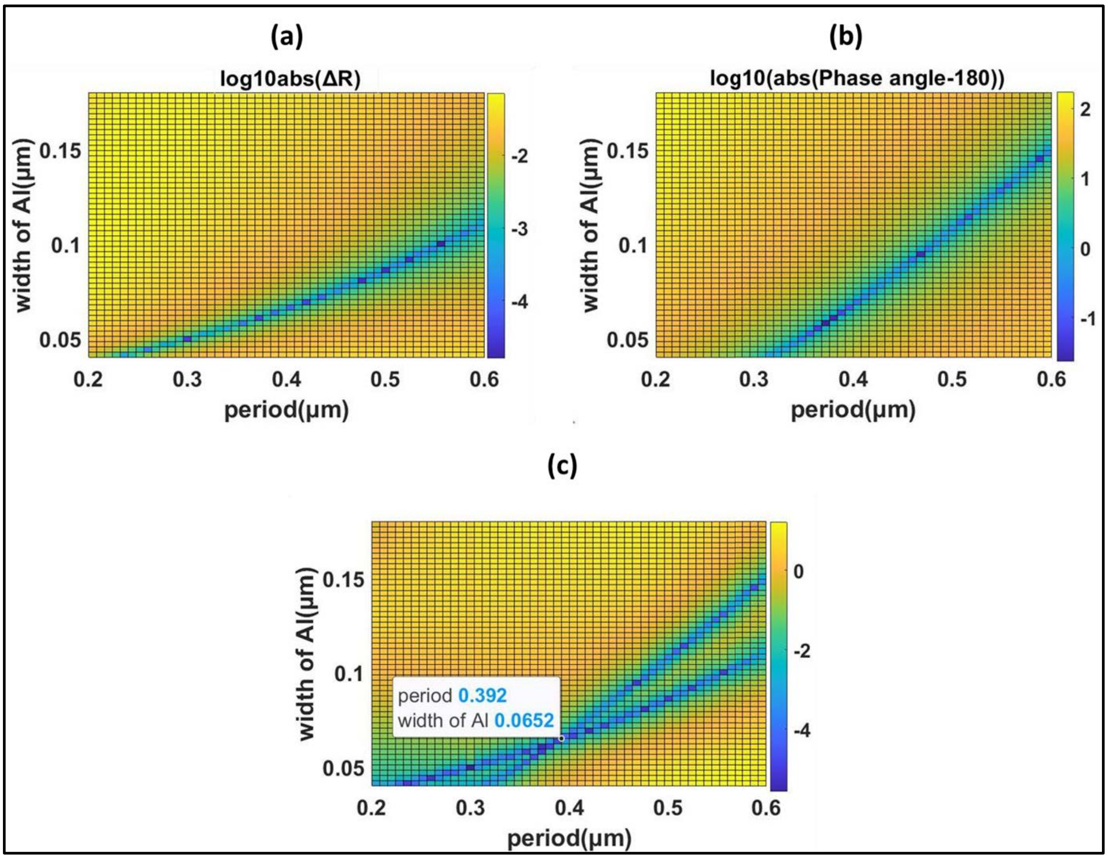

Figure 7.9 (a, b, c). Pseudo colour optimisation of phase difference and reflectivity difference. Pseudo-colour plots consist of a minimum of Δ*R* (a), minimum of Δ phase(b), and (c) representing the point of intersection of (a) and (b), i.e., period-=392 nm and width=65 nm.

The optimised parameter from Figure 7.9(c) is of deep-subwavelength dimensions; the periodicity is much less than the incident wavelength of the plane wave. Figure 7.9(c) shows that at wavelength =1550 nm, the Δ*R*=0 and phase difference is 180 degrees. The optimal grating periodicity is of deep-subwavelength dimensions and satisfies both polarisation independence conditions. The reflectivity corresponding to optimal grating parameters was plotted as shown in Figure 7.10(a). At 1550 nm, the difference in reflection corresponds to the s and p linearly polarised input light being zero.i.e., Δ*R*=0. I have simulated phase differences corresponding to the optimal grating parameters, as shown in Figure 7.10(b). At 1550 nm, the phase difference corresponds to the input light's linear polarisation components, which achieves a π phase shift.

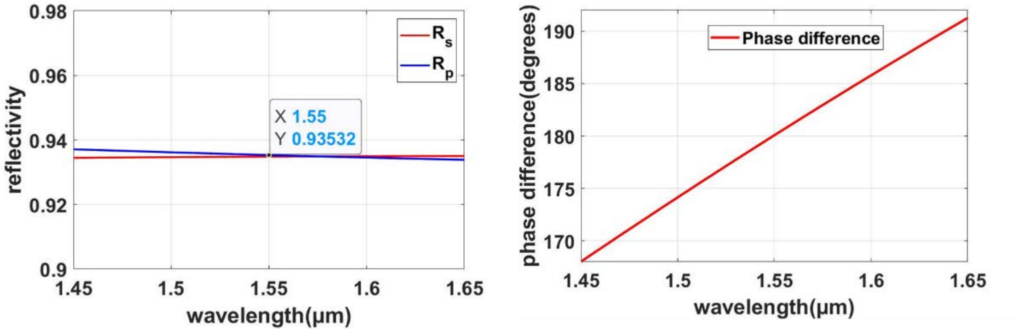

Figure 7.10 (a, b). Broad reflection efficiency from the optimised parameters. (b) phase difference simulated from 1450 nm to 1650 nm with the optimised parameters.

7.2.2 Polarisation independent LCoS optimisation at 1064 nm

Here I am optimising the uniperiodic metal-dielectric grating structure at 1064 nm wavelength to perform the design to show both conditions of phase retardance of 180 degrees and reflection efficiency difference of zero corresponding to the orthogonal polarisation components.

The uni-periodic structure simulated over a two-dimensional grid consists of grating periodicity varying from 800 nm to 300 nm and the width of Al ranging from 40 nm to 250 nm. As shown in Figure 7.11(a), the pseudo colour plot shows the phase difference plot as a function of the width of Al grating and periodicity. The dark blue spots refer to the phase difference having 180 degrees difference between the **s** and **p** polarisation components of reflected light. Figure 7.11(b) shows the reflection efficiency difference associated with the **s** and **p** polarisation as a function of the width of Al grating and the periodicity of the grating. Figure 7.11(b) shows that the dark blue spots describe the grating parameters associated with the zero reflection efficiency difference corresponding to **s**-and **p** polarisation components. Figure 7.11(c) refers to the overlapping of both curves, as shown in Figure 7.11(a) and Figure 7.11(b). It is evident that both the curves do not overlap and couldn't provide the optimal grating parameters satisfying both polarisation-independent conditions. Further optimisation is needed to meet the polarisation independence conditions, including π-phase difference and zero-reflection efficiency differences between the linear polarisation components.

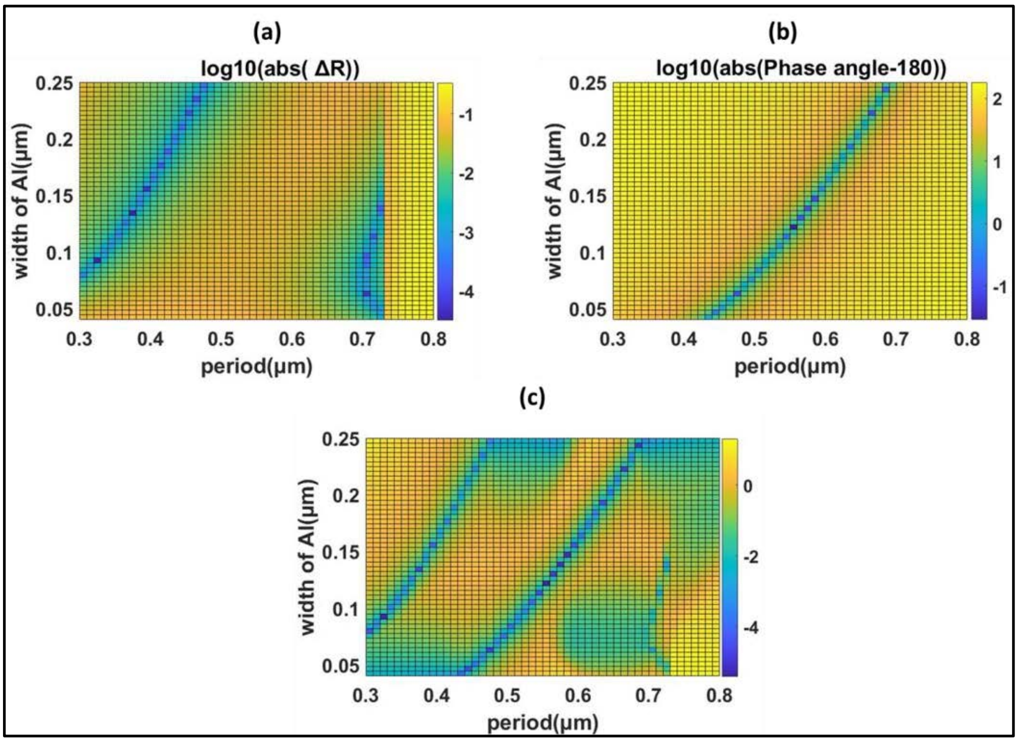

Figure 7.11 (a, b, c). Pseudo colour optimisation of phase difference and reflectivity difference. Pseudo-colour plots consist of a minimum of ΔR (a) with a period of grating varying from 300 nm to 800 nm and a width of Al ranging from 40 nm to 250 nm, a minimum of phase angle with a period of grating varying from 300 nm to 800 nm and the width of Al varying from 40 nm to 250 nm with grating thickness 300 nm at 1064 nm. (b), and (c) normalised minimum of both((a) and (b)) representing the overlapping of (a) and (b).

One of the significant grating design parameters includes the thickness of the uni-periodic grating. Here we analyse the impact of grating thickness by incrementing its value from 300 nm to 600 nm. From Figure 7.12(c), we can observe that we obtained two points of intersection. One has a deep subwavelength periodicity, and the other has near subwavelength periodicity. The near subwavelength periodicity point has a 590 nm periodicity, and the aluminium width is 69 nm (12% duty cycle); meanwhile, deep subwavelength dimensions are 400 nm periodicity and 82 nm width aluminium (21% duty cycle). However, the points don't match the optimal points and cannot provide the 180-degree phase difference and near-zero polarisation-independent reflectivity.

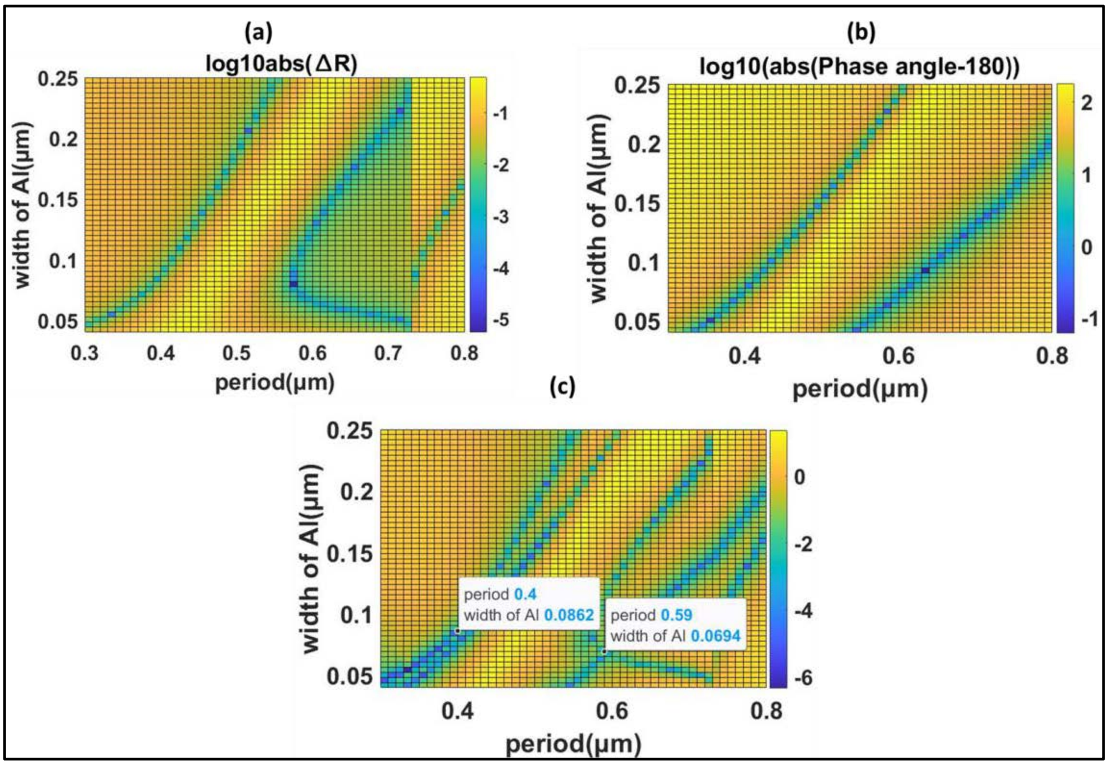

Figure 7.12 (a, b, c). Pseudo colour optimisation of phase and reflectivity difference associated with linear polarisation components of the input light. (a) Showing the pseudo color 2d-grid plot of reflection efficiency difference minimum with an incremented grating thickness of 600 nm (from 300 nm) over the grid consisting of periodicity from 300 nm to 800 nm and width of aluminium from 250 nm to 40 nm. (b) Illustrates the two-dimensional pseudo color plot with the same materials and parameters as in (a), where it evaluates phase difference minimum as a function of periodicity and grating thickness. (c) Illustrates the overlapping of the (a) and (b).

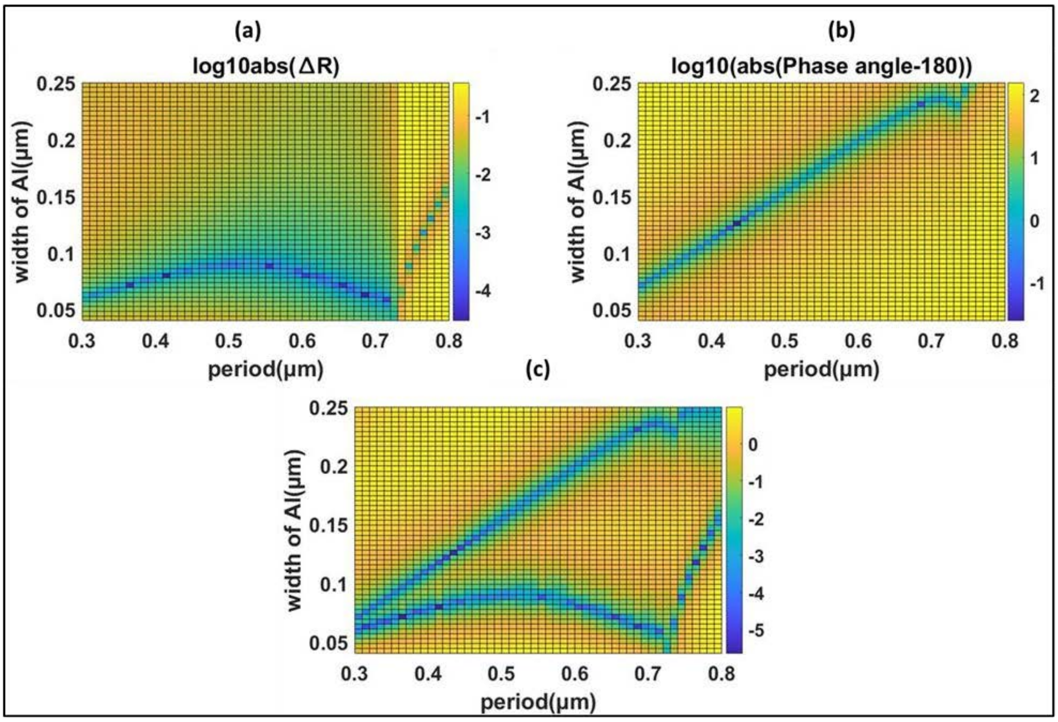

Figure 7.13 (a, b, c). Pseudo-colour optimisation of grating parameters. (a) Showing the pseudo color 2d-grid plot of reflection efficiency difference minimum with a decremented grating thickness of 200 nm (from 300 nm) over the grid consisting of periodicity from 300 nm to 800 nm and width of aluminium from 250 nm to 40 nm. (b) Illustrates the two-dimensional pseudo color plot with the same materials and parameters as in (a), where it evaluates phase difference minimum as a function of periodicity and grating thickness. (c) Illustrates the overlapping of the (a) and (b).

Then, I decreased the grating thickness from 300 nm to 200 nm and simulated the pseudo color plots for ΔR and phase difference. As Figure 7.13(c) illustrates, the non-linear curves do not intersect at this particular range of variables. In that case, I have changed the thickness again from 300 nm to 150 nm. The non-linear curves separate significantly and give no hope of intersecting each other, as shown in Figure 7.14(c).

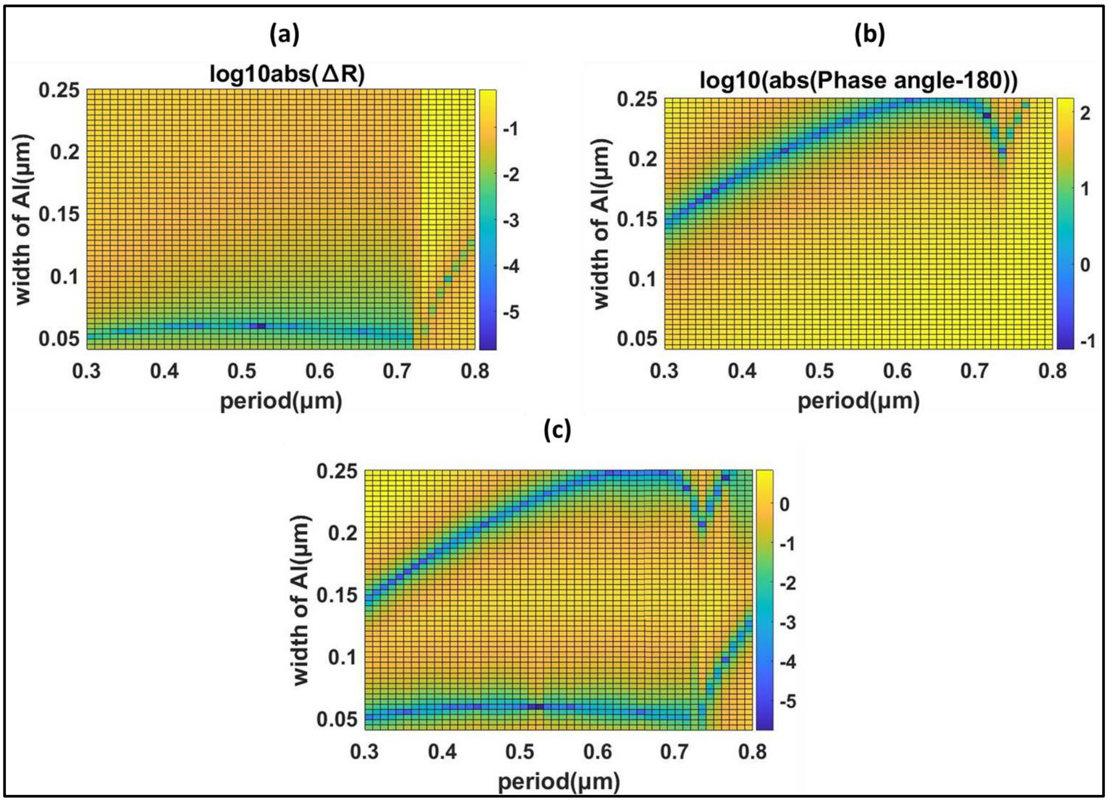

Figure 7.14 (a, b, c). Pseudo colour optimisation of phase and reflectivity difference associated with linear polarisation components of the input light. (a) Showing the pseudo color 2d-grid plot of reflection efficiency difference minimum with a decremented grating thickness of 150 nm (from 300 nm) over the grid consisting of periodicity from 300 nm to 800 nm and width of aluminium from 250 nm to 40 nm. (b) Illustrates the two-dimensional pseudo color plot with the same materials and parameters as in (a), where it evaluates phase difference minimum as a function of periodicity and grating thickness. (c) Illustrates the overlapping of the (a) and (b).

As I decrease the grating thickness from 300 nm to lower values, the pseudo phase colour plots and ΔR plots don’t seem to intersect, as shown in Figures 7.13(c) and 7.14(c).

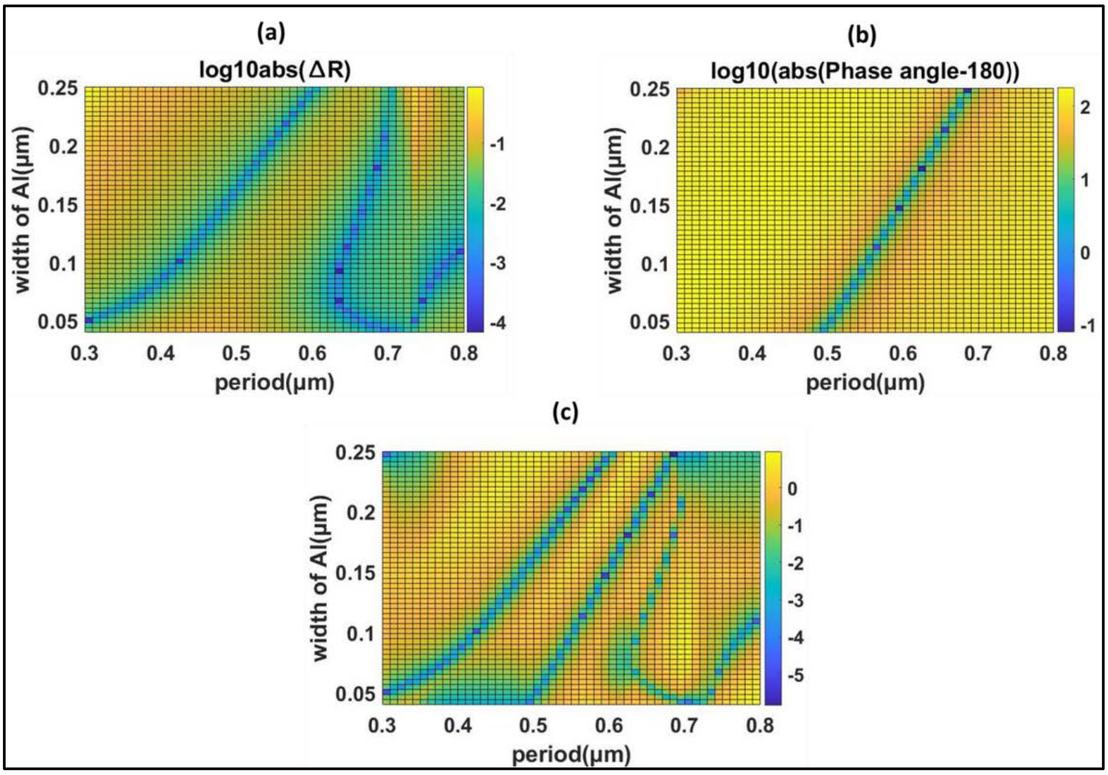

Figure 7.15 (a, b, c). Pseudo colour optimisation of phase and reflectivity difference associated with linear polarisation components of the input light. (a) Showing the pseudo color 2d-grid plot of reflection efficiency difference minimum with an incremented grating thickness of 400 nm (from 300 nm) over the grid consisting of periodicity from 300 nm to 800 nm and width of aluminium from 250 nm to 40 nm. (b) Illustrates the two-dimensional pseudo color plot with the same materials and parameters as in (a), where it evaluates phase difference minimum as a function of periodicity and grating thickness. (c) Illustrates the overlapping of the (a) and (b).

Here I have incremented the grating thickness from 300 nm to 400 nm. Figure 7.15(c) shows no intersection between the nonlinear curves. In that case, I have incremented the grating thickness from 300 nm to 700 nm by keeping all the parameters the same. This time, the nonlinear curves intersect and satisfy near polarisation independent reflectivity and 180-degree phase difference, as shown in Figure 7.16(c).

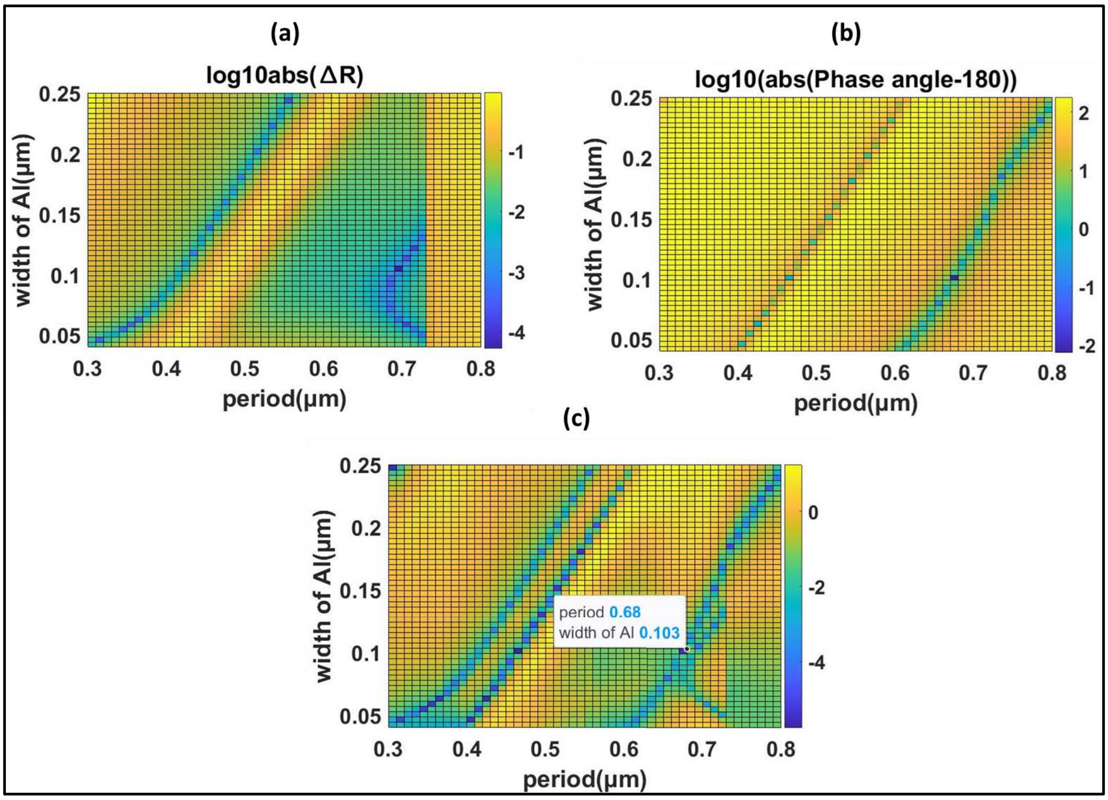

Figure 7.16 (a, b, c). Pseudo colour optimisation of phase and reflectivity difference associated with linear polarisation components of the input light with optimal parameters. (a) Showing the pseudo color 2d-grid plot of reflection efficiency difference minimum with a decremented grating thickness of 700 nm (from 300 nm) over the grid consisting of periodicity from 300 nm to 800 nm and width of aluminium from 250 nm to 40 nm. (b) Illustrates the two-dimensional pseudo color plot with the same materials and parameters as in (a), where it evaluates phase difference minimum as a function of periodicity and grating thickness. (c) Illustrates the overlapping of the (a) and (b).

The optimal grating parameters are; a grating thickness of 700 nm, a width of aluminium=103 nm, periodicity of the grating=680 nm, duty cycle of the grating of 15%, the thickness of low index layer is 120 nm, and the bottom reflecting Al-layer thickness is 75 nm.

Figure 7.17(a) illustrates the simulated reflectivity from 1014 nm to 1114 nm centred at 1064 nm. The difference in reflectivity associated with the linear polarisation components at 1064 nm is 0.004, a near-zero polarisation-independent reflectivity. Figure 7.17 (b) shows the simulated phase difference associated with the linear polarisation components of the input light. The phase difference is 180 degrees at 1064 nm.

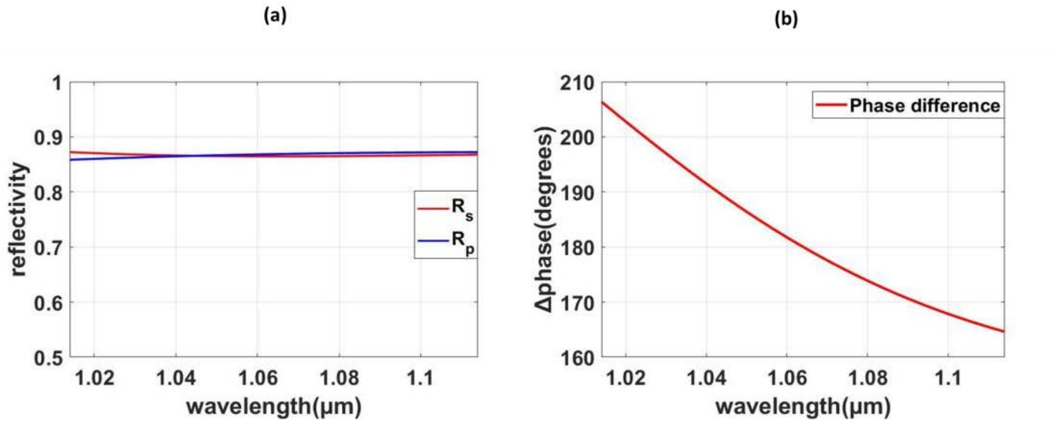

Figure 7.17 (a, b). Broad reflectivity and phase difference correspond to the optimal parameters. (a) Broad reflection efficiency from the optimised parameters showing zero reflectivity difference at 1064 nm. (b) phase difference simulated from 1014 nm to 1114 nm with the optimised parameters.

The limitation of the design is that, for ideal polarisation independent reflectivity, the optimal parameters were not within the industrial fabrication standards of duty cycle within the range of 30%-50%.

7.3 CONCLUSION

I have studied the phase response of uni-periodic subwavelength gratings. I have proven that the uni-periodic grating can rotate the s and p polarisation components of reflected light, resulting in a reflection phase retardance of 180 degrees. The grating is optimised for performing both π-phase rotation and ideal polarisation-independent reflectivity at 1550 nm. Interestingly, I have found that the optimal grating periodicity corresponds to deep subwavelength dimensions. The optimal grating period was 392 nm with a width of Al-grating of 65 nm. The periodicity of 392 nm is exciting since it is in the deep-subwavelength regime. I have also optimised the near-zero difference in reflectivity and pi-phase retardation of structure at 1064 nm. The optimised grating periodicity is 680 nm, and the width of Al is 103 nm. I need to further optimise the design by incorporating materials including Aluminium oxide, Titanium oxide, and Zirconium oxide instead of silica, as mentioned in the patent[49].

8 CHAPTER 8

8.1 CONCLUSIONS AND OUTLOOK

In this thesis, I have modelled the LCoS backplanes devoid of LC medium that combines high reflectivity and polarisation-independent operation. I have discussed various optimisation algorithms to model high-reflectivity LCoSDs.

As mentioned at the beginning of chapter 2, the typical thickness of multi-dielectric coating layers implemented to enhance the LCoS performance is 3.16 microns. My thesis's optimised models have a 0.5-1.5-micron range grating thickness. Compared to a dielectric layer thickness of 3-6 microns, the grating is compact, robust, and easy to fabricate and provides broad high reflectivity and polarisation-independent reflectivity. In chapter 3, I optimised the silicon high contrast grating (HCG) structure to have more than 99% reflectivity over a 40 nm bandwidth centred at around 1064. The total thickness of the LCoS backplane, except for the pixelated structure, is about 647 nm, including the cap layer of silica.

In chapter 4, the research aimed to optimise LCoS performance at around 1064 nm. This wavelength is utilised by a range of LASERs that work with the new series of Finisar Wave Shapers. The designs for enhanced reflectivity[40] have been developed by Frisken et al. for telecom C-band around 1550 nm. Here I confirm that these approaches remain viable at 1064 nm and perform a range of numerical parameter scans to optimise the LCoS performance at the new wavelength range. The reflectivity of conventional LCoS corresponding to s-polarised input light was enhanced after adding silicon HCG on top of the pixels. I have seen an improvement from 92% to 99% at 1064 after adding HCG. The optimised pixel periodicity is 6.5 microns. Lower the pixel size, dense packaging of pixels can be achieved, leading to higher resolutions in a feasible die area. I have qualitatively measured the standing wave generation at around 1060-1070 nm of the incidence wavelength. The pronounced standing waves generated at the diffraction regime of the pixels contribute diffractive optical losses, including light leakage at the inter-pixel gap.

As the silicon no longer performs well at the visible wavelength of operation, silicon-rich silicon nitride subwavelength gratings are employed in visible wavelength ranges. I have implemented genetic algorithm optimisation to find the optimal grating parameters in chapter 5. Also, I have implemented two-dimensional grid optimisation to validate the results obtained by the genetic algorithm. The fabrication tolerance was performed around the optimal parameters at 800 nm and 532 nm wavelengths. Both designs show an enhanced reflectivity of the s-polarised input light. The designs for enhanced reflectivity[40] have been developed by Frisken et al. for telecom C-band around 1550 nm using silicon HCGs. Here we confirm that these approaches remain viable at 800 nm and 532 nm for silicon nitride high contrast gratings and perform a range of numerical parameter scans to optimise the LCOS performance at the new wavelength range.

In chapter 6, I numerically optimised the reflectivity of silicon cross-linked gratings in order to increase the efficiency of LCoSDs. Based on two different designs, I have observed a significant increase in reflectivity that is independent of polarisation in the telecommunication C-band and 40nm wavelength ranges around 1.064 microns.

Finally, in chapter 7, I studied the physics behind the polarisation-independent LCoS developed by Finisar[49]. I have optimised the metal-dielectric uni-periodic structure for polarisation-independent reflectivity and 180-degree phase difference at 1550 nm and 1064 nm wavelengths of operation. The design for optimised polarisation independent reflectivity and 180 degrees phase difference fails to achieve the industrial fabrication standards of duty cycle (30%-50%). However, at a duty cycle of 29% and periodicity of 740 nm, the structure provides near polarisation independent reflectivity (the difference between the reflectivities associated with the linear orthogonal components of input light) and a 180-degree phase difference.

Despite these proposed structures and good performance, many critical challenges remain in the simulation of LCoS devices. It is highly desirable to have the exact data of the materials and parameters (wavelength and temperature-dependent property) involved in the design to optimise in different wavelengths. In the future, I would like to implement full vectorial field calculation using the finite element method (FEM) or with the finite difference method (FDM)[95-99], with the inclusion of the liquid crystal element in the model.

Since I'm using RCWA, the persistent issue with the simulation platform is that it's impossible to model structures with complex geometries, such as curved surfaces. Another ongoing issue is the sensitivity of FDTD with the simulation mesh size. The multiple reflections between the pixels and silica layers are not negligible and need to be considered for phase modulation applications of LCoS.

The RCWA method, FDTD method, or FEM method, predominantly in 3D, are however insufficient to simulate the entire LCoS structure, since this is a structure that involves a multi-scale-complex optical modelling problem, varying from millimetre scale of the LC layer and a glass layer to the nanometer scale for the dead space or interpixel gap. Thus hybrid approaches incorporating distinct optical modelling methods need to be implement[100] for advanced LCoS design.

APPENDIX A:GRATING DIFFRACTION CALCULATOR(GD-CALC)

A.1 IMPLEMENTATION OF GD-CALC

Grating diffraction calculator or GD-Calc is commercial software which calculates the diffraction efficiencies of uni-periodic(1D) and bi-periodic(2D) optical grating structures using Rigorous Coupled Wave Analysis (RCWA). It is a MATLAB-based electromagnetic simulation program performed within the MATLAB development framework.

GD-Calc also allows a flexible grating modelling facility where the function gdc.m is the workhorse of the software package. The function gdc.m accepts three inputs: a Grating-struct with the critical grating parameters and its geometric structure, an inc_field struct with the information about the incoming plane wave, and an order matric, indicating the diffraction order to be employed in the calculations. Further, since it can be applied within the MATLAB environment, it allows functional links of GD-Calc into user-defined optical models. In return, this can be blended into generic optimisation routines like two-dimensional grid optimisation, genetic optimisation etc., to further optimise the design performance without relying on data conversion and export/import processes. GD-Calc allows structure parameterisation and unrestricted control over the diffraction order selection.

Essential utility functions apart from gdc.m are gdc_plot.m: for plotting grating structures and gdc_eff.m: this function converts the output of gdc.m, i.e., the amplitude of transmission and reflection matrices, into diffraction efficiency data.

A.1.1 GD-Calc software interface overview

In order to use GD-Calc, one must first create a "grating" data structure that defines the grating geometry and optical materials. A data validation check can be performed as follows:

gdc(grating); (A1)

Also, one can plot a 3-D view of the grating,

gdc_plot(grating,param_index,pmt_display,x_limit); (A2)

“param_index” is a multi-dimensional parameter index associated with the parameterisation capabilities of GD-Calc. “pmt_display” identifies the display colours and legend strings of the grating’s dielectric materials employed. “x_limit” defines the 3D-plotting limits. "gdc_plot” internally call “gdc(grating)” to check the data validity.

The next step is constructing two additional data structures: “inc_field”, which defines the incident plane wave’s direction and wavelength, and “order,” which describes the specific diffraction orders retained in the simulations.

The GD-Calc simulation engine is then called as follows,

[param_size,scat_field,inc_field,inc_field] = …

gdc(grating,inc_field,order); (A3)

The “param_size” output is associated with the parameterisation, and the “inc_field” and “scat_field” output define “scattered field” and “incident field” are assigned to the function gdc_eff, which transforms the results to diffraction efficiencies for reflected and transmitted diffracted orders.

```
[ R, T ] = gdc_eff(scat_field,inc_field);                    (A4)
```

A.1.2 Constructing grating in GD-Calc

The structure “grating” consists of the following elements: (a) “grating.pmt”, a cell array of complex permittivities of the grating materials; (b) “grating.pmt_sub_index” and “grating.pmt_sup_index, the grating substrate and superstrate permittivities(assigned as indices into “grating.pmt”); (c) “grating.d$_{21}$”, “grating.d$_{31}$”, “grating.d$_{22}$”, and “grating.d$_{32}$”, relates to the fundamental grating period vectors; and (d) “grating.stratum” relates to the cell array of “strata” of grating, which define the internal design of the grating. For instance, consider the LCoS backplane with the grating structure depicted in Figure 2.9. It consists of a homogeneous stratum of silica layer on top, a uni-periodic subwavelength high contrast grating extending longitudinally along x-dimension, a homogeneous stratum of silica and a homogeneous stratum of the aluminium layer.

The following code illustrates the slew of stratum types incorporated to construct the LCoS backplane with grating and without pixels, as mentioned in Figure 2.9.

```
% Define parameters for LCoS backplane with grating and without pixels.

clear all;

Air_pmt = 1;

Si_pmt = 12.1104; %Si permittivity

SiO2_pmt = 1.9044; % superstrate permittivity
```

```
Al_pmt =-242.68+49.435i; % substrate permittivity (Aluminum)
wavelength=1.55; % micron
t1 = 0.08;  % micron Al - bottom (reflecting) grating thickness
tl = 0.21;  % thickness of silica layer below grating
tg = 0.18;  % thickness of grating
t4 = 0.1;   % thickness of silica above grating
d  = 0.850; % grating period
c1_2=0.5*(w_Si)/d
m_max=20; % maximum diffraction order index
% Construct uni-periodic subwavelength high-contrast grating
clear grating
grating.pmt=...
    {Si_pmt, Al_pmt, SiO2_pmt, Air_pmt}; % material permittivities
grating.pmt_sub_index=4; % substrate permittivity index
grating.pmt_sup_index=3; % superstrate permittivity index
grating.d21=d; % first grating period: y projection
grating.d31=0; % first grating period: x projection
grating.d22=0; % second grating period: y projection
```

```
grating.d32=d; % second grating period: x projection

% Construct the homogeneous stratum for the Aluminium layer

clear stratum

stratum.type=0; % homogeneous stratum

stratum.pmt_index= 2; % stratum's permittivity index

stratum.thick=t1; % stratum thickness

grating.stratum(1)=stratum;

% Construct the homogeneous stratum for the silica below the grating

clear stratum

stratum.type=0; % homogeneous stratum

stratum.pmt_index= 3; % stratum's permittivity index

stratum.thick=tl; % stratum thickness

grating.stratum(2)=stratum;
```

% Construct the stratum for uniperiodic silicon HCG. The following h_{11}, h_{12} indicates that the stratum's period vector matches the first grating period (Refer to equations 2.21 and 2.22).

```
clear stratum

stratum.type=1; % uniperiodic stratum

stratum.thick=tg; % grating stratum thickness
```

```
stratum.h11=1;
stratum.h12=0;
clear stripe
stripe.c1=-c1_2; % first stripe's boundary on positive side
stripe.pmt_index=3; % first stripe's permittivity index
stratum.stripe(1) =stripe;
stripe.c1=c1_2; % second stripe's boundary on positive side
stripe.pmt_index=1; % second stripe's permittivity index
stratum.stripe(2)=stripe;
grating.stratum(3)=stratum;
% Construct the homogeneous stratum for the silica above the grating
clear stratum
stratum.type=0; % homogeneous stratum
stratum.pmt_index= 3; % stratum's permittivity index
stratum.thick=t4; % stratum thickness
grating.stratum(4)=stratum;
```

As illustrated in Figure 2.9, a uni-periodic HCG stratum is defined by the following data fields: the type index (1 for uni-periodic and 0 for homogeneous stratum), two “harmonic indices” h_{11} and h_{12} and a stripe data field. The physical structure of uni-periodic HCG consists of a periodic array of parallel, vertical wall stripes whose periodicity and projections are defined by harmonic indices. The stratum comprises two stripes per periodicity, which are defined by “stratum.stripe(1)” and “stratum.stripe(2)”. One of the stripe's wall positions is defined by c1.

Next, I consider 2D-crosslinked silicon HCG having periodicity along the x and y-dimension on top of conventional LCoS. The following code illustrates the generation of the stand-alone 2D grating on top of LCoS, as shown in Figure 6.1(b).

%Construct the bi-periodic HCG structure on top of the homogeneous silica layer.

```
clear stratum

stratum.type=2; % biperiodic

stratum.thick=tg; % thickness of grating

stratum.h11= 10; Number of grating periods on top of aluminium pixels

stratum.h12=0;

stratum.h21=0;

stratum.h22=10; Number of grating periods on top of aluminium pixels

clear stripe

clear block

stripe.type=1; % inhomogeneous

stripe.c1=-c1_2;

block.c2=-c1_2; %Block 1 Silica
```

```
block.pmt_index=3;
stripe.block(1)=block;
block.c2=c1_2; %block 2 Silicon
block.pmt_index=1;
stripe.block(2)=block;
stratum.stripe(1)=stripe;
stripe.type=1; % inhomogeneous
stripe.c1=c1_2;
clear block
block.c2=-c1_2; %Block 1 Silicon
block.pmt_index=1;
stripe.block(1)=block;
block.c2=c1_2; %Block 2 Silicon
block.pmt_index=1;
stripe.block(2)=block;
stratum.stripe(2)=stripe;
grating.stratum(3)=stratum;
clear stratum stripe block
```

The fundamental difference between a uni-periodic stratum and a 2D-biperiodic stratum is that the latter has two additional harmonic indices, h_{21} and h_{22}, and its stripes can be either homogeneous or inhomogeneous. For a homogeneous stripe, stripe.type field equal to 0 and for an inhomogeneous stripe, stripe.type equal to 1. An inhomogeneous stripe (made of silicon block and silica block) in Figure 6.1(b) (e.g. stratum.stripe(1)) consists of the type identifier (stripe.type=1), c1 data field defining the positions of the boundary walls between the stripes and a "block" data field representing the structural blocks within the stripe. As illustrated in the unit cell in Figure 6.1(b), the first stripe consists of two blocks per period consisting of silica and silicon, which are represented by stripe.block(1) and stripe.block(2). Each block is defined by the position of the walls between adjoining blocks. The field pmt_index determines whether the material is either silica or silicon

APPENDIX B:GENETIC ALGORITHM OPTIMISATION

B.1 GENETIC ALGORITHM OPTIMISATION AND IMPLEMENTATION

Survival of the fittest is the basic idea behind natural biological evolution. Genetic algorithms are stochastic search methods based on evolutionary computational methods. GAs operates on a population of potential solutions, employing the principle of survival of the fittest to obtain a refined and more refined approximation to a solution. At each generation, a new set of better approximations to a solution is created by selecting individuals considering their fitness value in the problem. This procedure leads to the evolution of populations of individuals that are better matched to their environment than the individuals from which they were formed.

Figure B.1 shows the algorithm of a basic genetic optimisation. It starts with a number of individuals randomly initialised. The objective function or fitness function is then evaluated for these individuals. If the best objective function satisfies the optimisation criteria, the process terminates by assuming that the variables associated with the best fitness value are the solution to the problem.

If the variables associated with the best fitness function don't satisfy the optimisation criteria, the new generation of variables starts, pairs or is subjected to cross-over and mutation operations. The resulting individuals are selected according to their fitness function value for producing new offspring. Details of the processes are outlined in[101]. Such a GA is robust and performs well with various optimisation problems. The salient features of GAs are as follows,

- They blend with the coding of solutions set, for instance, numerical simulations using GD-Calc.
- They investigate from a set of the population rather than a single solution.
- They use fitness function value to determine better solutions than derivatives, making the process simple and robust.
- They use a probabilistic transition approach for generating the next set of solutions if the optimisation criteria are never met.

Meanwhile, compared to other optimisation techniques, GAs minimises the probability of getting stuck in local minima or maxima, increasing the solution's reliability. Although it's a time taking process, the simplicity of the process makes it more captivating compared to the other optimisation techniques.

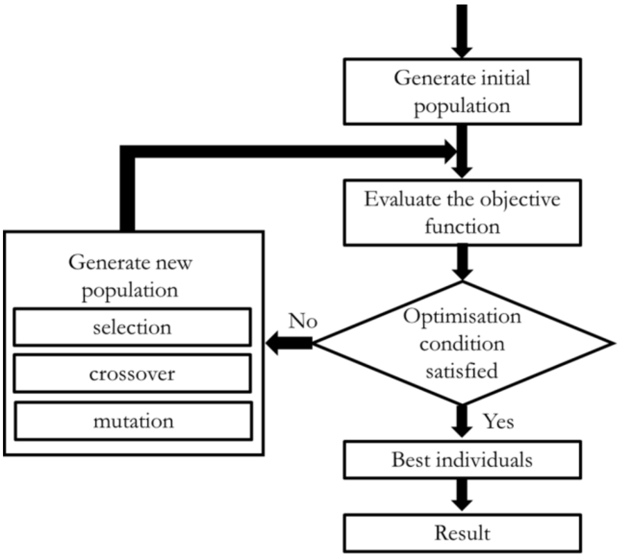

Figure B.1. Basic algorithm of a genetic optimisation.

Figure B.2 shows the flowchart of the genetic optimisation algorithm implemented to obtain the optimal grating parameters of the LCoSDs. The optimisation starts with a population of grating parameters defined within the upper-bound and lower-bound values defined in the simulation. The total population for each iteration will be 50 since the number of variables (local) associated with the optimisation (four) is less than five. GA evaluates the reflectivity of the s-polarised input light for each population generation and searches for a better score value. The score value is 1-R_s which has to be minimised to maximise the reflectivity for s-polarised input light. The convergence of the GA is achieved when the optimisation condition is satisfied. The optimisation condition is when the average change in the best fitness function value is less than or equal to the function tolerance. Also, the optimisation stops when it reaches the maximum number of generations. A four-variable optimisation's maximum number of generations is (number of variables*100) 400.

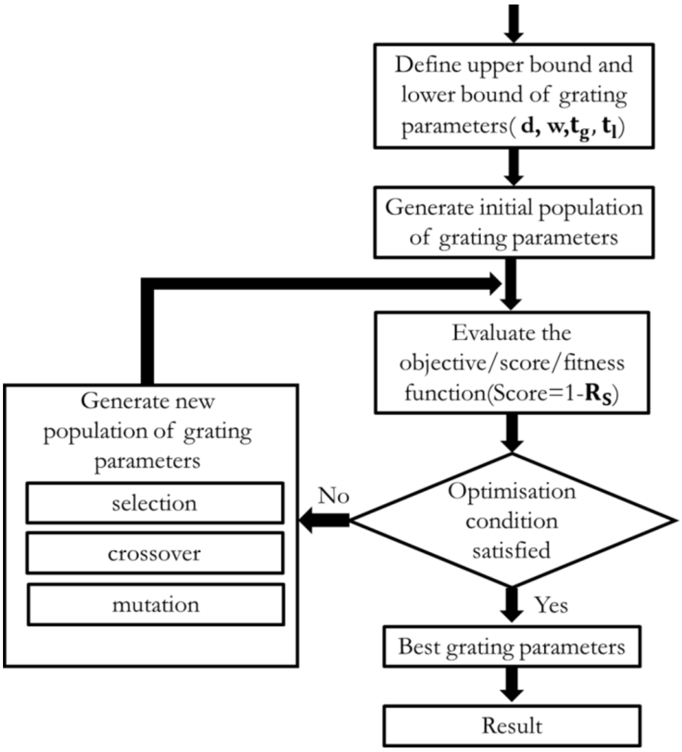

Figure B.2. Algorithm of the genetic optimisation implemented in section 5.3.1.

BIBLIOGRAPHY

1.Vettese, D., Liquid crystal on silicon. *Nature Photonics* **2010,** *4* (11), 752-754.

2.Choubey, A.; Andros, F.; Sammakia, B. G., Study of assembly processes for liquid crystal on silicon (LCoS) microdisplays. *IEEE Transactions on Components and Packaging Technologies* **2005,** *28* (2), 303-310.

3.Kazlas, P. T.; Johnson, K. M.; McKnight, D. J., Miniature liquid-crystal-on-silicon display assembly. *Optics Letters* **1998,** *23* (12), 972-974.

4.Zhang, Z.; Jeziorska-Chapman, A. M.; Collings, N.; Pivnenko, M.; Moore, J.; Crossland, B.; Chu, D. P.; Milne, B., High Quality Assembly of Phase-Only Liquid Crystal on Silicon (LCOS) Devices. *Journal of Display Technology* **2011,** *7* (3), 120-126.

5.Zhang, Z.; You, Z.; Chu, D., Fundamentals of phase-only liquid crystal on silicon (LCOS) devices. *Light: Science and Applications* **2014,** *3*.

6.Collings, N.; Davey, T.; Christmas, J.; Chu, D.; Crossland, B., The applications and technology of phase-only liquid crystal on silicon devices. *Journal of Display Technology* **2010,** *7* (3), 112-119.

7.Wilkinson, T.; Henderson, C.; Leyva, D. G.; Crossland, W., Phase modulation with the next generation of liquid crystal over silicon technology. *Journal of Materials Chemistry* **2006,** *16* (33), 3359-3365.

8. Cibula, M. A.; McIntyre, D. H., General algorithm to optimize the diffraction efficiency of a phase-type spatial light modulator. *Optics Letters* **2013,** *38* (15), 2767-2769.

9. Dai, H.; Liu, K. X. Y.; Wang, X.; Liu, J., Characteristics of LCoS phase-only spatial light modulator and its applications. *Optics Communications* **2004,** *238* (4-6), 269-276.

10. Engström, D.; Persson, M.; Bengtsson, J.; Goksör, M., Calibration of spatial light modulators suffering from spatially varying phase response. *Opt. Express* **2013,** *21* (13), 16086-16103.

11. Reichelt, S., Spatially resolved phase-response calibration of liquid-crystal-based spatial light modulators. *Applied optics* **2013,** *52* (12), 2610-2618.

12. Yang, H.; Robertson, B.; Yu, D.; Zhang, Z.; Chu, D., Origin of transient crosstalk and its reduction in phase-only LCOS wavelength selective switches. *Journal of lightwave technology* **2013,** *31* (23), 3822-3829.

13. Zhang, Z.; Yang, H.; Robertson, B.; Redmond, M.; Pivnenko, M.; Collings, N.; Crossland, W. A.; Chu, D., Diffraction based phase compensation method for phase-only liquid crystal on silicon devices in operation. *Applied optics* **2012,** *51* (17), 3837-3846.

14. Christmas, J.; Collings, N., Displays based on dynamic phase-only holography. *Applied Sciences* **2018,** *8* (5), 685.

15. Yin, K.; Hsiang, E.-L.; Zou, J.; Li, Y.; Yang, Z.; Yang, Q.; Lai, P.-C.; Lin, C.-L.; Wu, S.-T., Advanced liquid crystal devices for augmented reality and virtual reality displays: principles and applications. *Light: Science & Applications* **2022,** *11* (1), 1-22.

16. Frisken, S. In *Advances in Liquid Crystal on Silicon Wavelength Selective Switching*, Optical Fiber Communication Conference and Exposition and The National Fiber

Optic Engineers Conference, Anaheim, California, 2007/03/25; Optica Publishing Group: Anaheim, California, 2007; p OWV4.

17. Frisken, S.; Baxter, G.; Abakoumov, D.; Hao, Z.; Clarke, I.; Poole, S. In *Flexible and grid-less wavelength selective switch using LCOS technology*, 2011 Optical Fiber Communication Conference and Exposition and the National Fiber Optic Engineers Conference, 6-10 March 2011; 2011; pp 1-3.

18. Keyworth, B. P. In *ROADM subsystems and technologies*, OFC/NFOEC Technical Digest. Optical Fiber Communication Conference, 2005., 6-11 March 2005; 2005; p 4 pp. Vol. 3.

19. Frisken, S.; Zhou, H.; Abakoumov, D.; Baxter, G.; Poole, S.; Ereifej, H.; Hallemeier, P. In *High performance 'Drop and Continue' functionality in a Wavelength Selective Switch*, Optical Fiber Communication Conference and Exposition and The National Fiber Optic Engineers Conference, Anaheim, California, 2006/03/05; Optica Publishing Group: Anaheim, California, 2006; p PDP14.

20. Li, S.; Wan, Z.; Xu, J.; Zhong, S.; Wu, Y., Wavelength-selective switch based on a high f ill-factor micromirror array. *Chinese Optics Letters* **2011,** *9*, 090601.

21. Baxter, G.; Frisken, S.; Abakoumov, D.; Hao, Z.; Clarke, I.; Bartos, A.; Poole, S. In *Highly programmable wavelength selective switch based on liquid crystal on silicon switching elements*, 2006 Optical Fiber Communication Conference and the National Fiber Optic Engineers Conference, 5-10 March 2006; 2006; p 3 pp.

22. Dasgupta, P.; Das, M. K.; Das, B., Physical properties of three liquid crystals with negative dielectric anisotropy from X-ray diffraction and optical birefringence measurements. *Molecular Crystals and Liquid Crystals* **2011,** *540* (1), 154-161.

23. Kohns, P.; Schirmer, J.; Muravski, A. A.; Yakovenko, S. Y.; Bezborodov, V.; Dãbrowski, R., Birefringence measurements of liquid crystals and an application: An achromatic waveplate. *Liquid crystals* **1996,** *21* (6), 841-846.

24. Wu, S.-T.; Efron, U.; Hess, L. D., Birefringence measurements of liquid crystals. *Applied optics* **1984,** *23* (21), 3911-3915.

25. Armitage, D.; Kinell, D. K. In *Miniature spatial light modulators*, Advances in Optical Information Processing IV, SPIE: 1990; pp 158-165.

26. Armitage, D.; Kinell, D. K., Liquid-crystal integrated silicon spatial light modulator. *Applied optics* **1992,** *31* (20), 3945-3949.

27. Cotter, L.; Drabik, T. J.; Dillon, R. J.; Handschy, M. A., Ferroelectric-liquid-crystal/silicon-integrated-circuit spatial light modulator. *Optics letters* **1990,** *15* (5), 291-293.

28. McKnight, D. J.; Johnson, K. M.; Serati, R. A., 256× 256 liquid-crystal-on-silicon spatial light modulator. *Applied optics* **1994,** *33* (14), 2775-2784.

29. Bordakevich, S.; Rebón, L.; Ledesma, S., Optimization for maximum modulation of a double-pass twisted nematic liquid crystal display. *Applied optics* **2022,** *61* (4), 969-977.

30. Pezzaniti, J.; Chipman, R., Phase-only modulation of a twisted nematic liquid-crystal TV by use of the eigenpolarization states. *Optics letters* **1993,** *18* (18), 1567-1569.

31. Lu, S.-Y.; Chien, L.-C., Carbon nanotube doped liquid crystal OCB cells: physical and electro-optical properties. *Opt. Express* **2008,** *16* (17), 12777-12785.

32. Labrunie, G.; Robert, J., Transient behavior of the electrically controlled birefringence in a nematic liquid crystal. *Journal of Applied Physics* **1973,** *44* (11), 4869-4874.

33. Li, R.; Cao, L., Progress in phase calibration for liquid crystal spatial light modulators. *Applied Sciences* **2019,** *9* (10), 2012.

34. Soref, R.; Rafuse, M., Electrically controlled birefringence of thin nematic films. *Journal of Applied Physics* **1972,** *43* (5), 2029-2037.

35. Raynes, E., Optically active additives in twisted nematic devices. *Revue de Physique Appliquée* **1975,** *10* (3), 117-120.

36. Chigrinov, V. G., *Liquid crystal devices: physics and applications*. 1999.

37. Crossland, W.; Wilkinson, T.; Manolis, I.; Redmond, M.; Davey, A., Telecommunications applications of LCOS devices. *Molecular Crystals and Liquid Crystals* **2002,** *375* (1), 1-13.

38. Kelly, J. In *Application of liquid crystal technology to telecommunication devices*, National Fiber Optic Engineers Conference, Optica Publishing Group: 2007; p NThE1.

39. Chen, H.-M. P.; Yang, J.-P.; Yen, H.-T.; Hsu, Z.-N.; Huang, Y.; Wu, S.-T., Pursuing high quality phase-only liquid crystal on silicon (LCoS) devices. *Applied Sciences* **2018,** *8* (11), 2323.

40. Frisken, S. J.; Wu, Q., High reflectivity LCOS device. Google Patents: 2015.

41. Magnusson, R.; Shokooh-Saremi, M., Physical basis for wideband resonant reflectors. *Opt. Express* **2008,** *16* (5), 3456-3462.

42. Mateus, C. F.; Huang, M. C.; Chen, L.; Chang-Hasnain, C. J.; Suzuki, Y., Broad-band mirror (1.12-1.62 μm) using a subwavelength grating. *IEEE Photonics Technology Letters* **2004,** *16* (7), 1676-1678.

43. Mateus, C. F.; Huang, M. C.; Deng, Y.; Neureuther, A. R.; Chang-Hasnain, C. J., Ultrabroadband mirror using low-index cladded subwavelength grating. *IEEE Photonics Technology Letters* **2004,** *16* (2), 518-520.

44. Guan, M.; Chang-Hasnain, C., Resonant-cavity-enhanced pin photodetector using a high-contrast-grating for 940nm. *Opt. Express* **2022,** *30* (6), 9298-9306.

45. Iadanza, S.; Mendoza-Castro, J. H.; Oliveira, T.; Butler, S. M.; Tedesco, A.; Giannino, G.; Lendl, B.; Grande, M.; O'Faolain, L., High-Q asymmetrically cladded silicon nitride 1D photonic crystals cavities and hybrid external cavity lasers for sensing in air and liquids. *Nanophotonics* **2022,** *11* (18), 4183-4196.

46. Yao, H.-Y.; Wang, Y.-C.; Chang, T.-H.; Her, T.-H., Bandwidth tunable optical filter based on a tri-mode high-contrast grating. *arXiv preprint arXiv:2206.13771* **2022**.

47. Zhang, J.; Hao, C.; Zheng, W.; Liu, A. In *Vertical cavity using a heterostructure dual-period high-contrast grating*, CLEO: Science and Innovations, Optica Publishing Group: 2022; p JW3B. 74.

48. Frisken, S. J.; Wu, Q., High reflectivity LCOS device. Google Patents: 2019.

49. Frisken, S. J.; Baxter, G. W.; Wu, Q., Polarization-independent LCOS device. Google Patents: 2015.

50. Taflove, A.; Hagness, S. C.; Piket-May, M., Computational electromagnetics: the finite-difference time-domain method. *The Electrical Engineering Handbook* **2005,** *3*.

51. Moharam, M.; Grann, E. B.; Pommet, D. A.; Gaylord, T., Formulation for stable and efficient implementation of the rigorous coupled-wave analysis of binary gratings. *JOSA a* **1995,** *12* (5), 1068-1076.

52. Schröder, J.; Roelens, M. A. F.; Du, L. B.; Lowery, A. J.; Frisken, S.; Eggleton, B. J., An optical FPGA: Reconfigurable simultaneous multi-output spectral pulse-shaping for linear optical processing. *Opt. Express* **2013,** *21* (1), 690-697.

53. Chung, I.-S.; Iakovlev, V.; Sirbu, A.; Mereuta, A.; Caliman, A.; Kapon, E.; Mørk, J., Broadband MEMS-tunable high-index-contrast subwavelength grating long-wavelength VCSEL. *IEEE Journal of Quantum Electronics* **2010,** *46* (9), 1245-1253.

54. Rao, Y.; Yang, W.; Chase, C.; Huang, M. C.; Worland, D. P.; Khaleghi, S.; Chitgarha, M. R.; Ziyadi, M.; Willner, A. E.; Chang-Hasnain, C. J., Long-wavelength VCSEL using high-contrast grating. *IEEE Journal of Selected Topics in Quantum Electronics* **2013,** *19* (4), 1701311-1701311.

55. Huang, M. C.; Zhou, Y.; Chang-Hasnain, C. J., A surface-emitting laser incorporating a high-index-contrast subwavelength grating. *Nature photonics* **2007,** *1* (2), 119-122.

56. Carletti, L., High-index contrast grating reflectors for wavefront engineering. **2011**.

57. Knoernschild, C.; Kim, C.; Gregory, C. W.; Lu, F. P.; Kim, J., Investigation of optical power tolerance for MEMS mirrors. *Journal of microelectromechanical systems* **2010,** *19* (3), 640-646.

58. Mansha, S.; Moitra, P.; Xu, X.; Mass, T. W.; Veetil, R. M.; Liang, X.; Li, S.-Q.; Paniagua-Domínguez, R.; Kuznetsov, A. I., High resolution multispectral spatial light modulators based on tunable Fabry-Perot nanocavities. *Light: Science & Applications* **2022,** *11* (1), 1-11.

59. Yang, H.; Chu, D., Digital phase-only liquid crystal on silicon device with enhanced optical efficiency. *OSA Continuum* **2019,** *2* (8), 2445-2459.

60. Carletti, L., High-index contrast grating reflectors for wavefront engineering (Published master's thesis) **2011**.

61. Ashby, A. G. B. a. C. I. H., Fabrication of GaAs devices. *The Institution of Engineering and Technology* **2009,** *ISBN 978-1-84919-067-1*.

62. Wang, S.; Magnusson, R., Theory and applications of guided-mode resonance filters. *Applied optics* **1993,** *32* (14), 2606-2613.

63. Karagodsky, V.; Sedgwick, F. G.; Chang-Hasnain, C. J., Theoretical analysis of subwavelength high contrast grating reflectors. *Opt. Express* **2010,** *18* (16), 16973-16988.

64. Moharam, M.; Gaylord, T., Rigorous coupled-wave analysis of planar-grating diffraction. *JOSA* **1981,** *71* (7), 811-818.

65. (2019), K. C. J., Grating Diffraction Calculator (GD-Calc ®) [Source Code]. .

66. Yee, K., Numerical solution of initial boundary value problems involving Maxwell's equations in isotropic media. *IEEE Transactions on antennas and propagation* **1966,** *14* (3), 302-307.

67. Bérenger, J.-P., Perfectly matched layer (PML) for computational electromagnetics. *Synthesis Lectures on Computational Electromagnetics* **2007,** *2* (1), 1-117.

68. Gedney, S. D.; Zhao, B., An auxiliary differential equation formulation for the complex-frequency shifted PML. *IEEE Transactions on Antennas and Propagation* **2009,** *58* (3), 838-847.

69. Born, M.; Wolf, E., Principles of Optics, 7th (expanded) edition. *United Kingdom: Press Syndicate of the University of Cambridge* **1999,** *461*, 401-424.

70. Loewen, E. G., & Popov, E., Diffraction Gratings and Applications (1st ed.). CRC Press. . **1997**.

71. Kress, B. C.; Meyrueis, P., *Applied digital optics: from micro-optics to nanophotonics*. John Wiley & Sons: 2009.

72. Chang-Hasnain, C. J.; Koyama, F.; Willner, A. E.; Zhou, W. In *High Contrast Metastructures II*, Proc. of SPIE Vol, pp 863313-1.

73. Chang-Hasnain, C. J.; Mateus, C. F. R.; Huang, M. C.-Y., Ultra broadband mirror using subwavelength grating. Google Patents: 2007.

74. He, X.; Jie, J.; Yang, J.; Chen, Y.; Han, Y.; Zhang, S., Suppressing the unwanted resonance mode in a metal-insulator-metal structure using fine-structured gratings. *Opt. Express* **2019,** *27* (11), 15298-15308.

75. Zhang, C.; Zhou, Y.; Mi, L.; Ma, J.; Wu, X.; Fei, Y., High Performance of a Metal Layer-Assisted Guided-Mode Resonance Biosensor Modulated by Double-Grating. *Biosensors* **2021,** *11* (7), 221.

76. Yariv, A.; Yeh, P., Handbook of Optical Constants of Solids, Edward D. Palik. Academic Press, Boston: 1985.

77. Rakić, A. D., Algorithm for the determination of intrinsic optical constants of metal films: application to aluminum. *Applied optics* **1995,** *34* (22), 4755-4767.

78. Pierce, D. T.; Spicer, W. E., Electronic structure of amorphous Si from photoemission and optical studies. *Physical Review B* **1972,** *5* (8), 3017.

79. Chen, P.-J.; Engel, P.; Urbach, H. P. In *Investigation on backplane reflectivity and dielectric mirror coating designs for improved LCoS SLM performance in telecommunication beam steering*, Emerging Liquid Crystal Technologies XVI, International Society for Optics and Photonics: 2021; p 1170706.

80. Wang, Y.; Stellinga, D.; Klemm, A. B.; Reardon, C. P.; Krauss, T. F., Tunable optical filters based on silicon nitride high contrast gratings. *IEEE Journal of Selected Topics in Quantum Electronics* **2014,** *21* (4), 108-113.

81. Chang-Hasnain, C. J.; Yang, W., High-contrast gratings for integrated optoelectronics. *Advances in Optics and Photonics* **2012,** *4* (3), 379-440.

82. Conn, A.; Gould, N.; Toint, P., A globally convergent Lagrangian barrier algorithm for optimization with general inequality constraints and simple bounds. *Mathematics of Computation* **1997,** *66* (217), 261-288.

83. Conn, A. R.; Gould, N. I.; Toint, P., A globally convergent augmented Lagrangian algorithm for optimization with general constraints and simple bounds. *SIAM Journal on Numerical Analysis* **1991,** *28* (2), 545-572.

84. Goldberg, D. E., Optimization, and Machine Learning. *Genetic algorithms in Search* **1989**.

85. Luke, K.; Okawachi, Y.; Lamont, M. R.; Gaeta, A. L.; Lipson, M., Broadband mid-infrared frequency comb generation in a Si_3N_4 microresonator. *Optics letters* **2015,** *40* (21), 4823-4826.

86. Yang, H.; Chu, D. P., Digital phase-only liquid crystal on silicon device with enhanced optical efficiency. *OSA Continuum* **2019,** *2* (8), 2445-2459.

87. Chung, I.; Iakovlev, V.; Sirbu, A.; Mereuta, A.; Caliman, A.; Kapon, E.; Mørk, J., Broadband MEMS-Tunable High-Index-Contrast Subwavelength Grating Long-Wavelength VCSEL. *IEEE Journal of Quantum Electronics* **2010,** *46* (9), 1245-1253.

88. Frisken, S. J., Q . Wu,, High reflectivity LCOS device,US10302995B2. **2015**.

89. Ikeda, K.; Takeuchi, K.; Takayose, K.; Chung, I.-S.; Mørk, J.; Kawaguchi, H., Polarization-independent high-index contrast grating and its fabrication tolerances. *Applied optics* **2013,** *52* (5), 1049-1053.

90. Mateus, C. F. R.; Huang, M. C. Y.; Deng, Y.; Neureuther, A.; Chang-Hasnain, C., Ultrabroadband mirror using low-index cladded subwavelength grating. *IEEE Photonics Technology Letters* **2004,** *16*, 518-520.

91. Chong, T. K.; Wilson, J.; Mokkapati, S.; Catchpole, K. R., Optimal wavelength scale diffraction gratings for light trapping in solar cells. *Journal of Optics* **2012,** *14* (2), 024012.

92. Settle, M.; Salib, M.; Michaeli, A.; Krauss, T. F., Low loss silicon on insulator photonic crystal waveguides made by 193nm optical lithography. *Opt. Express* **2006,** *14* (6), 2440-2445.

93. Love, G. D., Liquid-crystal phase modulator for unpolarized light. *Applied optics* **1993,** *32* (13), 2222-2223.

94. Patel, J.; Lee, S. D., Electrically tunable and polarization insensitive Fabry–Perot étalon with a liquid-crystal film. *Applied physics letters* **1991,** *58* (22), 2491-2493.

95. Chiang, K.-H.; Chen, S.-H.; Wu, S.-T., Diffraction Effect on High-Resolution Liquid-Crystal-on-Silicon Devices. *Japanese Journal of Applied Physics* **2005,** *44*, 3068.

96. Davidson, A.; Elston, S., Three-dimensional beam propagation model for the optical path of light through a nematic liquid crystal. *Journal of Modern Optics* **2006,** *53*, 979-989.

97. Fan-Chiang, K.-H.; Wu, S.-T.; Chen, S.-H., Fringing-Field Effects on High-Resolution Liquid Crystal Microdisplays. *Display Technology, Journal of* **2006,** *1*, 304-313.

98. Kriezis, E. E.; Elston, S., A wide angle beam propagation method for the analysis of tilted nematic liquid crystal structures. *Journal of Modern Optics* **1999,** *46*, 1201-1212.

99. Kriezis, E. E.; Elston, S. J., Wide-angle beam propagation method for liquid-crystal device calculations. *Applied optics* **2000,** *39* (31), 5707-14.

100. Martínez, J. L.; Moreno, I.; del Mar Sánchez-López, M.; Vargas, A.; García-Martínez, P., Analysis of multiple internal reflections in a parallel aligned liquid crystal on silicon SLM. *Opt Express* **2014,** *22* (21), 25866-79.

101. Gen, M.; Cheng, R., *Genetic algorithms and engineering optimization*. John Wiley & Sons: 1999; Vol. 7